UNIVERSITÉ CÔTE D'AZUR

Inria informatiques mathématiques

École doctorale Sciences et Technologies de l'Information et de la Communication

Centre de Recherche Inria Sophia Antipolis - Méditerranée

Thèse

Présentée en vue de l'obtention du grade de docteur

de l'Université Côte d'Azur

Spécialité : Automatique, Traitement du Signal et des Images

par

Christos PAPAGEORGAKIS

Modèles de conductivité patient-spécifiques : caractérisation de l'os du crâne

---

Soutenue le 15 décembre 2017 devant le jury composé de :

Directrice de thèse	Juliette Leblond	Inria Sophia Antipolis, France
Co-directrice de thèse	Maureen Clerc	Inria Sophia Antipolis, France
Rapporteurs	Ioannis Stratis	National and Kapodistrian University of Athens, Grèce
	Carsten Wolters	University of Münster, Allemagne
Examinateurs	Jean-Michel Badier	Aix Marseille University, France
	Laure Blanc-Féraud	I3S Laboratory, France
Invité	Mateusz Rusiniak	BESA GmbH, Allemagne

UNIVERSITÉ CÔTE D'AZUR

Inria informatiques mathématiques

Doctoral School Sciences et Technologies de l'Information et de la Communication

Research Center Inria Sophia Antipolis - Méditerranée

PhD Thesis

Submitted in partial fulfillment of the requirements for the degree of doctor of the Université Côte d'Azur

Specialized in: Automation, Signal and Image Processing

by

Christos Papageorgakis

Patient specific conductivity models: characterization of the skull bones

---

Defended on December 15^{th} 2017 in front of the jury composed by:

Supervisor	Juliette Leblond	Inria Sophia Antipolis, France
Co-supervisor	Maureen Clerc	Inria Sophia Antipolis, France
Reviewers	Ioannis Stratis	National and Kapodistrian University of Athens, Greece
	Carsten Wolters	University of Münster, Germany
Examiners	Jean-Michel Badier	Aix Marseille University, France
	Laure Blanc-Féraud	I3S Laboratory, France
Invited	Mateusz Rusiniak	BESA GmbH, Germany

Acknowledgements

I honestly believe that a thesis is the product of a collective work, as there are more people involved than the Ph.D student who writes the thesis. Therefore in this section, I would like to thank all those how were there to guide me, supported me, help me, accompany me and create the right conditions in order to achieve this task in the most pleasant way.

First of all, I would like to sincerely thank my supervisor Juliette Leblond for her continuous support, patience and guidance over all these years. She was always there, in all times, giving me confidence and strength to continue, not only by transferring her knowledge to me with the most effective ways but also helping me to overcome various difficulties. I am grateful meeting her and creating such a strong bond, both in a scientific and in a friendly form. Equally I would like to thank my co-supervisor Maureen Clerc for her guidance and continuous support of my Ph.D study and related research. Her challenging questions and critical thinking helped me to understand in depth my research topic and push me to become the researcher I am today. I could not have imagined having better supervisors, they were complementary in their role and both responsible for what I have succeeded!

Besides my supervisors, I would like to thank the two reviewers of my manuscript Ioannis Stratis and Carsten Wolters not only for their time and extreme patience but also for their comments and recommendations which improved my thesis and my understanding in so many ways. I really enjoyed discussing with them my work and hearing about their experience in their fields, they made the process of reviewing my thesis so enjoyable!

At this point, I would like to thank the rest of my thesis committee: Jean-Michel Badier, Laure Blanc-Féraud and Mateusz Rusiniak, for their insightful comments and encouragement, but also for the hard question which push further to widen my research from various perspectives.

I would also like to express my gratitude to those who collaborated with me in this project: Benjamin Lanfer (and Mateusz Rusiniak) from the BESA company for their guidance in practical aspects of my research, their advice and comments when needed. Christian G. Benar (and Jean-Michel Badier) from the Aix Marseille University for providing me the patient data but also their expertise and knowledge in research and clinical practices. Jean-Paul Marmorat from Ecole des Mines ParisTech for providing me countless

times support for using the FS3D software and among other things, showed me the mathematical aspect of programming. Theodore Papadopoulo who was the first that provided me an opportunity to work in the exiting field of neuroscience as an intern in Athena team and since then he is always present providing me with feedback, advices and guidance. My gratitude also goes to Sylvain Chevillard who showed me the mathematical way of thinking and proving theorems, while also imparted me his enthusiasm in math and computer science.

My sincere thanks to all the people from APICS team, Athena team and the BESA company, that welcomed me when working with them and treated me as one of their own. I am happy to have met them and apart from being my colleges for all these years, they become also my friends. A special thanks to Brahim, Nathanaël, Kai, Kostia, and Sebastien who managed to endure my company over the years, sharing the same office for a period of time! A huge thanks also to Stephanie for the numerous times helping me with Inria and not only matters, even if she didn't have to.

A huge thanks to the Porco Rosso team of close friends formed during the years of our Ph.D lives: Dmitry P. from Russia, the best office mate that became a true friend having endless deep conversations, Matthias C. from Belgium, the guy how was visiting us but always felt like living with us, Stefano C. the Italian friend who made us the best risotto nights and make us feel what "una faccia una razza" means, Konstantinos M. from Greece, the best friend that followed me to France and supported me without even asking! A huge thanks also to my best friend from Greece: Μωυσής, Χάρης, Μάρα και Ζωή for their company and support all these year. A huge thanks also to Dora, that although meeting in the competitive environment of our master program, became from the beginning my good friend and accompany me also in the following years at Inria. Thanks also to the great people I have met: Adam (the Viking), Marco, Dimitra, Rutger, Nathalie, Antonia, Guillermo, Mouloud, Federica, Isa, Abib, Patryk, Samuel, Sébastian, David, and Gibin.

A huge thanks also to my family: Ένα τεράστιο ευχαριστώ στην οικογένειά μου που καθημερινά και για όλα τα χρόνια της ζωής μου ήταν δίπλα μου, δείχνοντάς μου έμπρακτα την αγάπη τους, στηρίζοντάς με σε κάθε μου απόφαση, προσπαθώντας με τον καλύτερο δυνατό τρόπο να μου παρέχουν τα απαραίτητα ηθικά και υλικά εφόδια για να εξασφαλίσω ένα καλύτερο μέλλον. Ένα ξεχωριστό ευχαριστώ στην αδερφή μου Ινώ, που μεταξύ χιλιάδων πραγμάτων που με έμαθε, ήταν η πρώτη που με έκανε να καταλάβω ότι έχω τις απαραίτητες γνώσεις για να γίνω ερευνητής.

Last but not least, I would like to thank my dear Elena for her patience, support and encouragement the last and long months of writing my thesis. She was the most affected during that period, but despite the difficulties, she was there for me to support me. Her presence (and not only) made my task easier and the whole period a pleasant memory!

Table of Contents

Abstract

One of the major issues related to electroencephalography (EEG) is to localize where in the brain signals are generated, this is so called inverse problem of source localization. The quality of the source localization depends on the accuracy of the geometry and the electrical conductivity model used to solve the problem. Among the head tissues, the skull conductivity is the one that influences most the accuracy of the source localization, due to its low conductivity value. Moreover, the human skull is a bony tissue consisting of compact and spongy bone layers, whose thickness vary across the skull. As the skull tissue composition has strong inter-individual variability both in terms of geometry and of individual conductivity, conductivity estimation techniques are required in order to determine the unknown skull conductivity. The aim of this thesis is to reduce the uncertainty on the skull conductivity both in spherical and realistic head geometries in order to increase the quality of the inverse source localization problem. Therefore, conductivity estimation is first performed on a 3-layered spherical head model. Existence, uniqueness and stability of the conductivity in the intermediate skull layer are discussed, together with a constructive recovery scheme. Then a simulation study is performed comparing two realistic head models, a bulk model where the skull is modelled as a single compartment and a detailed one accounting for the compact and spongy bone layers, in order to determine the importance of the internal skull structure for conductivity estimation in EEG.

General introduction

To better understand the human brain, neuroscientists have worked on various models, experiments, techniques, recording and imaging modalities to reveal its structure and functionalities [72]. A fundamental problem in neurosciences is to localize where is the electrical activity generated inside the brain, what is the so called inverse problem of source estimation. The inverse problem of source estimation aims at locating and estimating the source of the electric activity of the functioning human brain, preferably using non-invasive measurements, such as electroencephalography (EEG), see [17, 23, 36, 48, 49, 57].

EEG measures the effect of the electric activity of active brain regions through values of the electric potential obtained by a set of electrodes placed at the surface of the scalp [23] and serves for clinical (location of epilepsy foci) and cognitive studies of the living human brain.

Before solving the inverse source problem, and for numerical simulation purposes, one first solve the forward EEG problem, that is, given a source distribution and a head model, what is the generated electrical potentials at a set of electrodes located at the surface of the skull. The quality of the forward solution, and the inverse solution, depends on the accuracy of the volume conductor model used, i.e. the head model, reflecting the geometry and the electrical conductivity values of the different head tissues [47].

Indeed, the human head consists of several tissues with some of the most common tissues found in head models being: the scalp, the skull, the cerebrospinal fluid (CSF), and the brain which is often divided into gray and white matter.

A plethora of head models has been proposed to model the human head and the various tissues within it. In general, the head models are divided in two categories in terms of geometry. First, the spherical head models, where the geometry of the human head is simplified to a sphere, while the different head tissues are modelled as spherical layers [10, 23, 31, 36, 39, 57, 90]. The second category consists in the realistic head models, where the tissues of the head are described in greater detail [2, 15, 26, 65, 103], often extracted from imaging modalities such as magnetic resonance imaging (MRI), while less often using computed tomography (CT) scans [43] and combination of the two [88].

One of the biggest advantages of the spherical models, due to the simplicity of the spherical geometry, is that an analytical solution can be computed for the problem (mainly the forward), whereas a numerical solution can be obtained based on the analytical solution with low computational cost. In the realistic head models, different numerical approaches have to be considered to solve the problem in the complex geometry, such as the boundary element method (BEM) [22,46,77] and the finite element method (FEM) [109]. Those solutions are in general more costly, compared to the solutions obtained in the spherical domain. However, the solutions obtained on spherical models might be less accurate compared to the ones on realistic models, as it has been shown in [25,27], where the accuracy of the source localization is reduced with errors up to few centimetres (cm). Yet, a solution to the first might be used as an initial solution for the later. For example, estimating the quantity of sources from given EEG measurements, is not a trivial task and one may solve the problem in a simplified spherical geometry [23] and then use the estimated quantities in a realistic head model to accurately localize the sources. In addition, theoretical results such as existence, uniqueness and stability of a solution in the spherical case may be obtained and used as proofs of concept for solutions obtained in the realistic models. Thus, even though the two modelling types are quite different in terms of geometry, both appear to be important in solving the different aspects of the problem in EEG.

The inverse source localization problem in EEG is influenced by the electric conductivities of the several head tissues and especially by the conductivity of the skull due to its low value [100]. In addition, the human skull is a bony tissue consisting of compact and spongy bone compartments, whose distribution and density vary across individuals, and according to age, since humidity of tissues, and therefore their conductivity tends to decrease [78].

Therefore conductivity estimation techniques are required to minimize the uncertainty in source reconstruction due to the skull conductivity. Typically, an inverse conductivity estimation problem aims at determining an unknown conductivity value inside a domain Ω from measurements acquired on the boundary $\partial\Omega$. In the EEG case, the measurements can be modelled as pointwise values obtained on a portion of the boundary $\partial\Omega$, the measured potentials at a number of EEG electrodes (between 2 and 512 in modern EEG protocols) at the upper part of the scalp.

However, nowadays there are still many applications where the conductivity of the skull is described by a given fixed value for the whole tissue.

Measurements of conductivity performed on extracted skull flaps from patients under intra-cranial surgery, showed that depending the local skull structure and the proportion of compact and spongy bone in the sample, a significant variation in the measured conductivity values is observed [95]. This indicates the necessity for more accurate head models both in the skull tissue geometry and electrical conductivity.

The aim of this thesis is to minimize the uncertainty of the skull conductivity and investigate the importance of skull inhomogeneity for conductivity estimation, in order to improve the accuracy of the inverse source localization problem. The inverse conductivity estimation problem is first studied deriving analytical formulas for a spherical head geometry where the skull was modelled as a single and homogeneous layer. Existence, uniqueness and stability of the solution are discussed, together with a reconstruction algorithm for the skull conductivity (Part I). Derivation of analytical formulas while considering an inhomogeneous skull, for instance assuming that the skull itself is made of concentric layers, seems too simplistic. Therefore, we then investigate the importance of skull inhomogeneity for conductivity estimation considering realistic head models. We perform a simulation study that compares two realistic head models: the first modelling the skull as a single and homogeneous layer, the second modelling its inhomogeneity by accounting for compacta and spongiosa. Other aspects under consideration are the selection of the proper skull tissue and the influence of different skull templates on conductivity estimation (Part II).

Due to its rather general formulation, this work could be extended to other geometries and unknown tissue conductivities. The inverse conductivity estimation problem could also be considered from other modalities (magnetoencephalography, MEG, or Electrical Impedance Tomography, EIT).

Contributions and structure of the thesis

The work of this thesis was performed within APICS and Athena project teams at Research Center Inria Sophia Antipolis - Méditerranée, France, in collaboration with BESA GmbH, Gräfelfing, Germany, and with Institut de Neurosciences des Systèmes (INSERM), Aix Marseille University, France. It was supported by the Région Provence-Alpes-Côte d'Azur, France, and BESA GmbH.

Contributions

This thesis deals with two different approaches of the inverse skull conductivity estimation problem in EEG.

- In the first we consider the estimation problem in a spherical 3-layered head geometry where the skull is modelled as a single homogeneous layer. Existence, uniqueness and stability of the solution are established, together with a reconstruction algorithm for the skull conductivity. The behaviour and the robustness of our algorithm is investigated over various configurations, with respect to errors either to the EEG measurements or on the source term (Part I).
- In the second, we investigate the importance of the skull inhomogeneity for conductivity estimation considering realistic head models. We perform a simulation study that compares two realistic head models: the first modelling the skull as a single and homogeneous layer, the second modelling its inhomogeneity by accounting for compacta and spongiosa compartments. Other aspects under consideration are the selection of the proper skull tissue and the influence of different skull templates on the conductivity estimation (Part II).

Outline

The content of this thesis is structured in an introductory part (chapter 1), the first main part (Part I, chapters 2 and 3 followed by a conclusion), the second main part (Part II, chapter 4) and the final part (chapter 5).

Chapter 1 gives an introduction to head modelling. First, some fundamental concepts in EEG are explained. The structure of the human head is discussed along with several head models encountered in the literature. A physical model derived from the Maxwell equations under the quasi-static approximation is introduced to model the electromagnetic fields generated by currents within the human brain. In addition, various forward and inverse problems in EEG are presented. Finally, the influence of the various head tissues, their segmentation and their conductivities is discussed for the numerous head models encountered in the literature.

In Part I, Chapter 2, the inverse conductivity estimation problem is considered in a spherical head geometry. Existence, uniqueness and stability of the solution are discussed, together with a constructive scheme for the inverse skull conductivity estimation problem.

Then, in Chapter 3, a reconstruction algorithm for the inverse skull conductivity estimation problem in EEG is provided. A numerical analysis is then performed using simulated EEG data. The behaviour and the robustness of our algorithm with respect to errors on the measurements or the source term is investigated. Agreement of the conductivity estimation results with the theoretical stability properties of the problem is discussed.

In Part II, Chapter 4, the importance of skull inhomogeneity for conductivity estimation is considered in realistic head models. A simulation study is performed that compares two realistic head models: the first modelling the skull as a single and homogeneous layer, the second modelling its inhomogeneity by accounting for two different types of skull tissues (compacta and spongiosa). Other aspects under consideration are the selection of the proper skull tissue and the influence of different skull templates on conductivity estimation.

Finally, in Chapter 5, a general discussion and a conclusion are given. The practical aspects of conductivity estimation are discussed, while we suggest ways to improve the inverse conductivity estimation results both for spherical and realistic head models.

Notations

$\mathbf{E}$	electric field
$\mathbf{B}$	magnetic field
u	electric potential
σ	conductivity
$\mathbf{J}$	current density
$\mathbf{J}^P$	cerebral current density (sources)
$\mathcal{S}$	general source term
$\mathbf{p}_q$	source moment
$\mathbf{C}_q$	source location
Q	number of sources
Ω	domain
$\partial\Omega$	interface
S	sphere
n	outwards unit normal vector
$T, \mathcal{T}$	transfer and transmission matrices and operators
r	radius of sphere
θ	inclination
ϕ	azimuth
$\mathbf{x}$	location $\in \mathbb{R}^3$
$\mathbf{r}$	location $\in \Omega \subset \mathbb{R}^3$
g	continuous potential at the boundary $\partial\Omega$
g_i	pointwise values of the potential g
g_{km}	spherical harmonics coefficients of the potential values g
$\tilde{g}_k$	normalized spherical harmonics coefficients from g_{km}
β_{0km}	spherical harmonics coefficients of the source term
$\tilde{\beta}_{0k}$	normalized spherical harmonics coefficients from β_{0km}

where symbols in **bold** represent vector valued quantities, unless otherwise indicated.

CHAPTER 1

Head modelling

This chapter gives an introduction to head modelling. First, some fundamental concepts in EEG are explained. The structure of the human head is discussed along with several head models encountered in the literature. A physical model derived from the Maxwell equations under the quasi-static approximation is introduced to model the electromagnetic fields generated by currents within the human brain. In addition, various forward and inverse problems in EEG are presented. Finally, the influence of the various head tissues, their segmentation and their conductivities is discussed for the numerous head models encountered in the literature.

Electroencephalography (EEG) measures passively and non-invasively the electrical activity of the functioning brain by recording electric potentials at the surface of the scalp [78]. The electrical activity of the brain is generated by displacement of charges of billions of synchronously active cells, called neurons, that exist within it and produce current that spreads in the whole head volume conductor. The generated potentials are captured by a set of electrodes/sensors (between 2 and 512) that are placed on the scalp using a EEG cap, leading to the obtained scalp EEG measurements, see Figure 1.1.

The sets of synchronously active neurons generating the electric potentials, recorded by EEG measures, are called generators or sources. It is believed that most of the signals detected by EEG are generated by pyramidal neurons in the cortex, due to their local parallel distribution and orientation which is pointing perpendicular to the local cortical surface [16].

Similarly to EEG, magnetoencephalography (MEG) [30, Ch. 4] measures the normal component of the magnetic field produced by electrical currents within the brain (the same sources generating the EEG measurements), using sensitive magnetometers placed above the surface of the scalp.

The electrical activity generated within an active area of the brain can

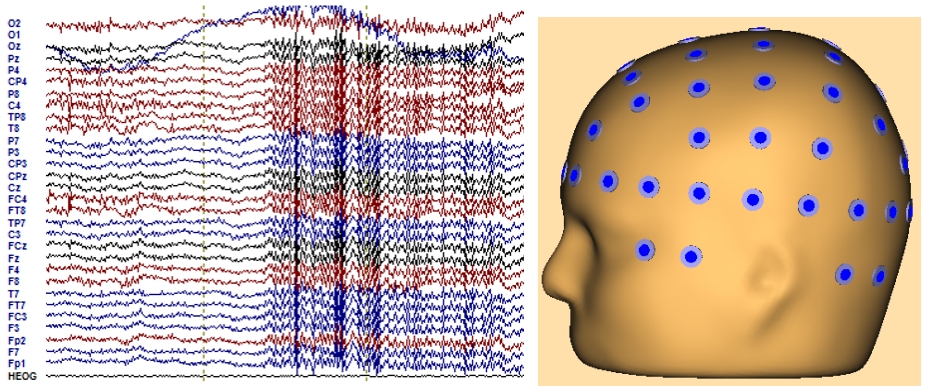

Figure 1.1: Recorded electrical potentials by a set of electrodes at the surface of the scalp. [Left] The measured EEG potentials at electrodes along the time. [Right] Electrodes locations on the scalp.

be "approximated" by an equivalent pointwise current dipole, located at the center of the active area [16, 34], as illustrated in Figure 1.2. As multiple brain areas can be active at the same time, one can also use multiple dipoles to approximate the measured potentials [76]. More sophisticated multipolar (see for example [56]) or distributed sources (see the discussion in [72, Sec. 3.2]) models are also proposed to model the brain's electrical activity. We refer to [78] for more details on how the electric fields and potentials recorded by EEG are generated in the brain.

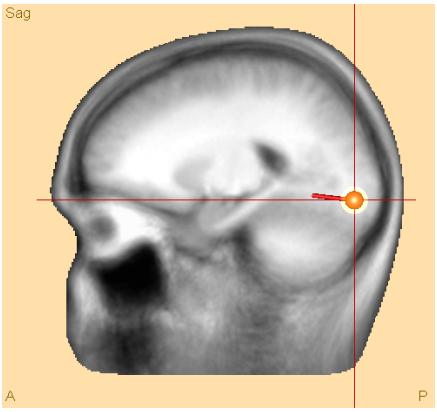

Figure 1.2: A pointwise current dipole is placed within the brain to model the electrical activity of a small active brain patch.

One of the major issues related to EEG (or MEG) is to localize where in the brain signals are generated. The solution to this so called inverse source localization problem in EEG, depends on the mathematical algorithm chosen [47], as well as on the choice of the head volume conductor model

(in short, the head model), which reflects the geometry and the electrical conductivity values of the different head tissues.

Tissues within the human head

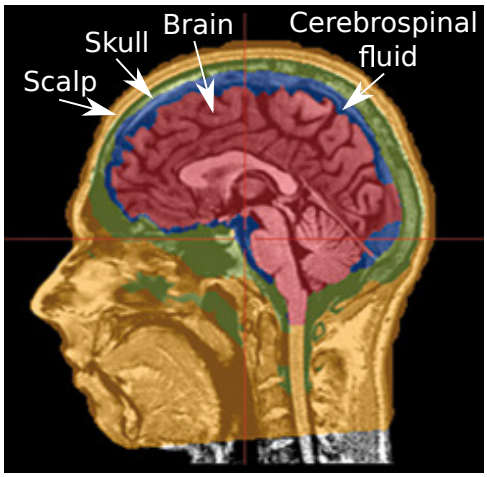

Figure 1.3: Head tissues commonly found in head models.

The human head is an inhomogeneous medium that consists of several types of tissue, including muscle, fat, bones, fluids, and air cavities. Although the human skull is anatomically quite complicated, an approximation of the human head is usually considered in head modelling, distinguishing only a few tissue types. Some of the most commonly considered tissues in head models are: the scalp, the skull, the cerebrospinal fluid (CSF), and the brain (see Figure 1.3) which is often separated into gray and white matter.

As the electrical activity generated in the brain spreads within the head volume conductor, it has to pass through the different head tissues to reach the EEG sensors. Based on the tissue composition (bone, fluid, muscle or fat), each is characterized by a different electrical conductivity. The measurements recorded by EEG, are affected by the electrical conductivities of the different tissues existing within the head. Various studies have been performed to determine the dielectric properties of the various head tissues by measuring samples (in vivo and in vitro) over a range of injected current frequencies (see for example [41, 42]).

Among the head tissues, the skull is the one that influences most the EEG source localization because of its low conductivity [100] compared to the other head tissues which are far more conductive. A brain to skull conductivity ratio as high as 80 has been considered in the past in head modelling, while more recently there are suggestions that this ratio is closer to 15 [79]. Measurements of skull samples extracted from different skull

areas show that the skull is inhomogeneous with the local skull conductivity depending on the structure and bone composition variations [3].

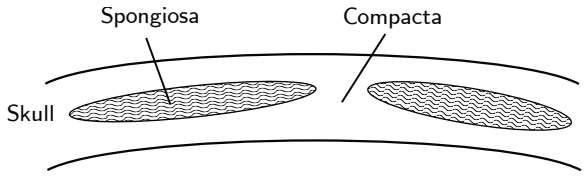

Figure 1.4: The layered structure of the skull consisting of compact (compacta) and spongy (spongiosa) bone layers.

Indeed, the skull is a bony tissue consisting of two layers of compact bone (compacta) separated by a layer of spongy bone (spongiosa), whose thickness vary across the skull. While compacta is present everywhere across the skull (apart from the suture lines, i.e. a type of joint between the bones of the skull, see [37, Sec. 59 and 60]), spongiosa may not be always present, as illustrated in Figure 1.4. As skull conductivity is mostly due to fluids existing within the bones, the spongy bone, which contains more space for fluids, is expected to be more conductive comparing to the compact bone. As shown in [3, 28] the conductivity value of the spongiosa compared to compacta may differ substantially, by a factor of 4.5 within an individual. Further investigations in [95] show that the amount of spongiosa present within a sample plays an important role on the measured skull conductivity value, while the presence of suture lines (a type of joint by fibrous tissue) can significantly increase the skull conductivity.

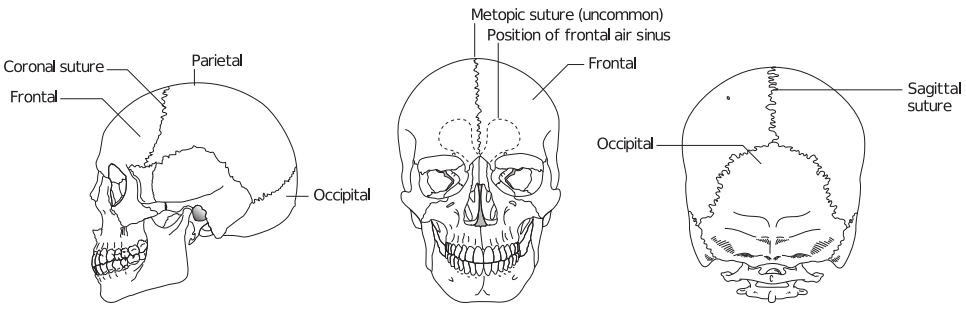

Figure 1.5: Cranial suture: A type of joint between the bones of the skull where the bones are held tightly together by fibrous tissue.

As the skull tissue composition has strong inter-individual variability both in terms of tissue geometry and of individual tissue conductivity, a fixed conductivity value for the skull can not be set in advance and describe any individual. Although the skull conductivity shows important variability in terms of measured conductivities, this is not necessarily the case for the other head tissues. In [18] the conductivity of a number of CSF samples

was measured and concluded to be $1.79\,S/m$ as there was minor variability across the measured samples.

When measuring the conductivity of extracted samples, important is the dependence of the measured values on the frequency of the injected current and the condition of the sample (storage conditions or temperature during the measurement) [42, 95].

Physical modelling

Maxwell's equations

The electromagnetic fields and currents generated within the human brain, obey the Maxwell partial differential equations:

$$\nabla \cdot \mathbf{E} = \frac{\rho}{\epsilon}\,, \tag{1.1}$$

$$\nabla \times \mathbf{E} = -\frac{\partial \mathbf{B}}{\partial t}\,,$$

$$\nabla \cdot \mathbf{B} = 0\,, \text{ and}$$

$$\nabla \times \mathbf{B} = \mu_0(\mathbf{J} + \epsilon\frac{\partial \mathbf{E}}{\partial t}) \tag{1.2}$$

which basically relate the electric field $\mathbf{E}$ ($\mu V/mm$), with the magnetic field $\mathbf{B}$ (fT) and the current density $\mathbf{J}$ ($\mu A/mm^2$). We denote with ρ the charge density, ϵ the electrical permittivity of the medium and μ the magnetic permeability. We refer to [83] for more information on the Maxwell equations and the units used.

An equation that is implied by the Maxwell's equations (1.1) and (1.2) is the conservation of charges formula, that relates the current density with the charge density:

$$\nabla \cdot \mathbf{J} = \frac{\partial \rho}{\partial t}\,.$$

Quasi-static approximation

For EEG and MEG modelling, the spatial scale (size of the human head), the recording frequencies, and the medium properties make it possible to neglect the inductive, capacitive and displacement effects, and to effectively omit the time-derivatives [38, App. A] in the above time-varying general setting, leading to the following simplified equations:

$$\nabla \times \mathbf{E} = 0 \quad \text{and} \quad \nabla \cdot \mathbf{J} = 0\,.$$

From the first one, we deduce that:

$$\mathbf{E} = -\nabla u \tag{1.3}$$

where u (V) is the electric potential, a scalar quantity. Separating the current density $\mathbf{J}$ into the ohmic current $\sigma\mathbf{E}$ and the source current (also called primary current) $\mathbf{J}^P$ leads to:

$$\mathbf{J} = \sigma\mathbf{E} + \mathbf{J}^P \tag{1.4}$$

where σ $(1/(\Omega mm)$ or $S/mm)$ is the electrical conductivity of the medium. The addition of the primary current $\mathbf{J}^P$ term is physiologically meaningful, as the brain is not a passive medium, but is subject to an electrical activity reflected by the electrically active brain regions. Estimating the primary current distribution is one of the main goals in EEG and MEG.

Conductivity equation

Using equations (1.4) and (1.3), under the quasi-static approximation:

$$\begin{aligned}
&\mathbf{J} = \sigma\mathbf{E} + \mathbf{J}^P \\
&\mathbf{J} = -\sigma\nabla u + \mathbf{J}^P \\
&\nabla\cdot\mathbf{J} = -\nabla\cdot(\sigma\nabla u) + \nabla\cdot\mathbf{J}^P \\
&as\ \nabla\cdot\mathbf{J} = 0 \\
&\boxed{\nabla\cdot(\sigma\nabla u) = \nabla\cdot\mathbf{J}^P}
\end{aligned}$$

leads to our general model for the electric potential u in terms of conductivity equation with source term in divergence form:

$$\nabla\cdot\big(\sigma(\mathbf{r})\nabla u(\mathbf{r})\big) = \nabla\cdot\mathbf{J}^P(\mathbf{r}) \quad \text{in} \quad \Omega\subset\mathbb{R}^3 \tag{1.5}$$

where $\sigma(\mathbf{r})\in\mathbb{R}$ is the real valued conductivity of the medium at location $\mathbf{r}$.

As discussed earlier, the human head is an inhomogeneous medium, due to the various tissue existing within it. The value of the medium conductivity $\sigma(\mathbf{r})$ when considering the domain $\Omega\subset\mathbb{R}^3$ of the head changes depending on the tissue at location $\mathbf{r}$.

Piecewise constant conductivity models

To model the inhomogeneity of the human head, a domain $\Omega\subset\mathbb{R}^3$ composed of a number of tissues $i = 0,\ldots,N$ represented as a set of nested regions $\Omega_i\subset\Omega$ can be considered. There the conductivity of each region Ω_i can be considered constant (homogeneous within regions) and be described by a real value (isotropic assumption). Assuming also that the innermost region Ω_0 represents the brain and that sources can only exist within the brain, equation (1.5) becomes:

$$\nabla \cdot (\sigma_i \nabla u) = \nabla \cdot \mathbf{J}^P$$
$$\nabla \sigma_i \cdot \nabla u + \sigma_i \Delta u = \nabla \cdot \mathbf{J}^P$$
$$as \;\; \nabla \sigma_i = 0$$
$$\boxed{\sigma_i \Delta u = \nabla \cdot \mathbf{J}^P} \quad in \;\; \Omega_0$$

while the right hand side of the equation is zero for the other regions Ω_i, $i > 0$.

The conductivity of a region can also be modelled as anisotropic (different conductivity value for different directions). In this case conductivity is a tensor (or matrix).

In practice, the value of the conductivity at each location is given by the head model, which approximates the various tissues geometry.

Geometry of head models

A plethora of head models has been proposed to model the human head and approximate the various tissues within it. In general, the head models are divided in two categories in terms of geometry.

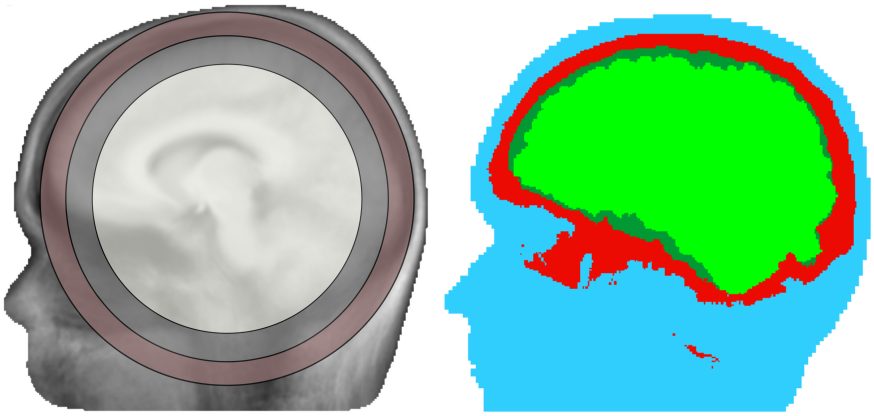

Figure 1.6: Head models. [Left] 3-layered concentric spheres model. [Right] 4-layered realistic model.

First, spherical head models were proposed, where the geometry of the human head is simplified to a ball, while the different head tissues are modelled as homogeneous spherical layers [10,23,36,57,90]. When approximating the head with spheres, a 3-layer concentric model is most often used, where the brain is modelled as a homogeneous ball surrounded by two spherical shells, representing the skull and the scalp tissues, respectively. The size of the outer most sphere can either be fixed (unit sphere) [23] or chosen such that it matches the measured diameter of the human head [90]. Alternatively, when a set of points that describe the surface of an individual's

scalp are given, the size of the outer most sphere can be fitted to those points, solving a least square problem. This is the case in [92], where the surface of the scalp is extracted from magnetic resonance images (MRI), and used to fit the size of the outer most sphere, while the points that are not on the fitted sphere, are projected on it using a scaling factor. Similarly, in the tool called CARTOOL [19] different sets of 3-layer spherical models are considered, to take into account the non-spherical head geometry at the electrode locations, in an attempt to improve the source localization accuracy of the 3-layer spherical model. Multiple sphere models are also considered in MEG [64]. Considering other geometries, in [67] an elliptic head approximation is investigated to solve the source localization problem whereas in [30, Ch. 4] both the EEG and MEG case is considered in an ellipsoidal geometry.

The second category consists in realistic head models [2, 15, 26, 65, 103], where the tissues of the head are described in greater detail, often extracted from imaging modalities such as MRI, while less often using computed tomography (CT) scans [43] or by other means like in [111] where images of slices of the human head were used. Combinations of different imaging modalities has also been investigated to capture as accurately as possible the geometry of the head. For example in [88] the authors used MRI and CT data to improve the accuracy of the head model in the skull geometry. The choice of the imaging modality to extract the various head tissues will be discussed later on in Section 1.5.

Usually when appropriate data are available, for the subject of interest, an individual head model can be constructed segmenting the different tissues from the available data. Conversely, when individual data are not available, a realistic approximation can be used, usually constructed by registering data of different individuals into the same space and then averaging them to produce an average realistic head model [99] also known as template or atlas [29]. Such models can also be used to perform group statistics, where the head geometry of several individuals should be in a common space to be comparable [89]. Age appropriate atlases have also been proposed to account for morphological changes of the head over time and especially during the early stages of growth in children [40, 91]. Due to the imperfect anatomical correspondence among the individuals, the created head model might cause errors in the source localization as discussed in [99]. Averaging of several MRI aquisitions of the same individual is also proposed in [52], producing a template know as "Colin 27 Average Brain[1]". Spherical and realistic head models (including individual and age appropriate heads for childes and adults) can be found in the BESA software[2] (BESA GmbH, Gräfelfing, Germany).

[1] http://www.bic.mni.mcgill.ca/ServicesAtlases/Colin27

[2] https://www.besa.de/products/besa-research/features/head-model-selection/

Forward and inverse problems in EEG

As discussed at the beginning of this chapter, one of the most important problems in EEG, is to localize where is the electrical activity generated inside the brain. Before solving the source localization problem, and for numerical simulation purposes, one first must solve the forward problem in EEG.

- The forward problem in EEG is: given a source distribution and a head model, what is the generated electrical potentials at a set of electrodes located at the surface of the scalp, as illustrated in Figure 1.7. In other words, given the primary current $\mathbf{J}^P(\mathbf{r})$ located within the brain at location $\mathbf{r}$, the domain of the head Ω (the geometry of the various tissues) and the medium conductivity $\sigma(\mathbf{r})$ at each location, compute the generated potential $u(\mathbf{r})$ at the boundary $\mathbf{r} \in \partial\Omega$.

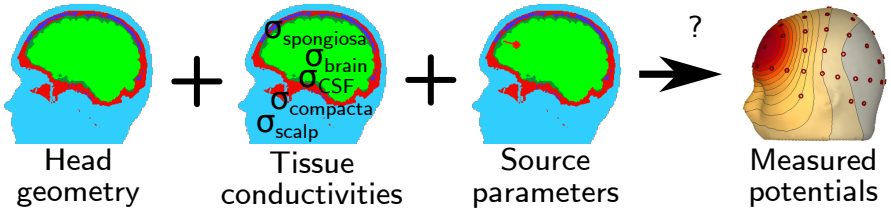

Figure 1.7: The forward problem in EEG: given the geometry of the head (and the various tissues within it), the conductivity of the tissues and the parameters of the sources, compute the electric potential at a set of electrodes located at the surface of the scalp.

On the other hand, several inverse problems can be considered in EEG depending on the information to be recovered.

- The inverse source estimation problem, where given measurements of the potential u at some points on the boundary $\partial\Omega$ and the medium conductivity σ, the aim is to estimate the primary current $\mathbf{J}^P$ that explains the measured potentials. Variations of this problem may consider given measurements on a part of the boundary $\Gamma \in \partial\Omega$ or measurements at the whole boundary $\partial\Omega$ and the recovery of unknown information about the sources (number of sources, location, orientation and moment strength).

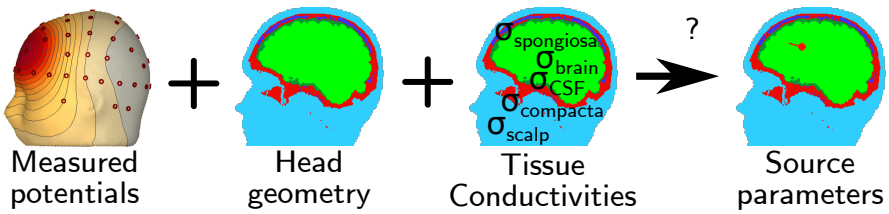

Figure 1.8: The inverse problem of source estimation in EEG: given the electric potential at the surface of the scalp, the geometry of the head and the conductivity of the tissues, estimate some parameters of the sources.

- The inverse conductivity estimation problem, which aims at determining an unknown conductivity value inside a domain Ω from measurements acquired on the boundary $\partial\Omega$ while the geometry of the head and the source parameters are given. Solving the conductivity estimation problem one may consider some tissue conductivities to be known while estimating the unknown one or ones (for example estimating a ratio of two conductivities).

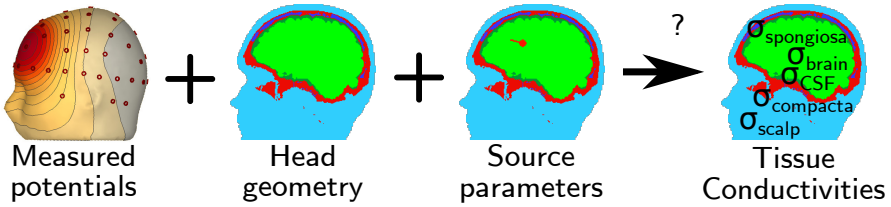

Figure 1.9: The inverse conductivity estimation problem in EEG: given the electric potential at the surface of the scalp, the geometry of the head and the parameters of the sources, recover information about the tissues conductivities.

Simultaneous source and conductivity estimation has also been studied in [1, 68], combining the two inverse problems.

Forward problem solutions

When the geometry of the head is simple enough to be expressed in an analytical form, such as the layered spherical head geometries, an analytical solution can be constructed for the forward problem. A numerical solution can be obtained from the analytical solution with low computational cost. In more complex head geometries, such as the realistic head models which capture the head geometry in greater detail, numerical approaches have to be considered to solve the forward problem. Those solutions are in general computational costly, compared to the solutions obtained in the spherical domain.

Both in the spherical and the realistic head geometries, the obtained solutions (analytic or numerical), practically solve equation (1.5).

The methods used to solve the forward problem in the realistic geometries are the boundary element method (BEM) [22, 46, 77] and the finite element method (FEM) [20, 109]. A prerequisite for both methods is a mesh of the head, i.e. a discretization of the head volume and its tissues into

elements. The head geometry and the various tissues within it can be extracted by segmenting MRI or other imaging data (as already discussed in Section 1.3), while the segmented images distinguishing the various tissues can be used to create the required mesh.

Solving the EEG forward problem for the discretized head volume with known conductivities for its tissue, a lead field matrix can be computed, that represents the linear relation between the amplitudes of dipolar sources within the brain and electrode measurements on the scalp [109]. The dimension of a lead field matrix is $(n_{electrodes} \times 3 * n_{nodes})$ where $n_{electrodes}$ is the number of electrodes and $3 * n_{nodes}$ corresponds to the 3 canonical orientations at n_{nodes} fixed dipole locations, i.e. the nodes of the mesh assigned to the brain tissue. An implementation of BEM can be found in OpenMEEG [46] whereas an implementation of FEM in BESA MRI[3] (BESA GmbH, Gräfelfing, Germany).

Inverse problem solutions

In contrast to the forward problem, the inverse problems in EEG are far more difficult and in general not well posed[4]. This is especially true for the inverse source estimation problem. The solution of the source estimation problem is not unique, as more that one source distributions may explain the same measured potentials, while measurement errors due to high levels of noise (compared to the power of the obtained signals) can make the solution unstable. To solve the ill-posed problem (as a problem is called when it is not well posed), apart from the head model, a source model is required along with constrains over the source distribution. A detailed review of some recent source localization techniques and the constrains each uses can be found in [72] and the references therein, while a few more different approaches can be found in [23, 35, 72].

Finally, to solve the inverse source localization problem in EEG, one usually has to compute a number of forward solutions, which can be obtained fast, having already computed once a lead field matrix.

Influence of head tissues and models

As discussed earlier in this chapter, the head is anatomically complicated and inhomogeneous both in terms of tissue geometry and tissue conductivity. While several head models have been proposed to approximate the human head (spherical or realistic) with various numbers of included tissues, the

[3] http://www.besa.de/products/besa-mri/besa-mri-overview

[4] A mathematical problem is called well posed, when a solution exist, the solution is unique and the solution is stable i.e. the solution changes continuously with variations of the initial conditions.

influence of each tissue geometry and conductivity to the problem's solution (forward or inverse) has to be investigated separately.

For several years, 3-layer spherical models have been used to construct analytical solutions both for the forward and the inverse problems in EEG. Numerical solutions obtained on the spherical models were often compared to numerical solutions obtained on realistic head models for validation purposes, see for example [46, 70]. Due to the unrealistic geometry of the spherical models and the modelling of the tissues as spherical layers (which is too simplistic to capture the internal inhomogeneity of some head tissues and especial of the skull), realistic head models are used which are proven to be more accurate, especially in source localization.

In [105] the authors investigated the influence of different tissue compartments on the signal topography and signal magnitude, by incrementally introducing tissue layers to a 3-layer realistic head model. They concluded that including the highly conductive CSF layer significantly reduced the measured errors while distinguishing between gray and white matter is also important. Their findings also suggest that white matter anisotropy and distinguishing between the skull compacta and spongiosa did not significantly improve the results with spongiosa having the smallest influence among the included tissue layers. But, their models were not used to solve the inverse source localization problem and assess on the influence of the different tissues simplifications.

In contrast, in [86] the authors investigated the influence of different head models on scalp potentials and on the inverse source localization problem, performing a simulation study based on dipolar sources in the motor cortex. They considered a highly heterogeneous head model accounting for eleven head tissues (scalp, skull compacta and spongiosa, CSF, gray and white matter and other soft tissues) and compared it to simplified versions of it. Their study suggests that the CSF tissue should be included in head models, as it plays an important role, which is in agreement with [105]. In contrast to [105], their findings suggest that distinction between gray and white matter is not that important, as the obtained localization errors in the simplified model were quite low. The influence of the skull inhomogeneity (distinction between compacta and spongiosa) was investigated at the same time with other tissues (fat and muscle) and thus was not clear from their results.

From the above and as the electrical conductivity of the CSF has already been determined and showed minor variability across the measured samples [18] it is concluded that it should be considered in head modelling. However, segmentation of the CSF layer from MRI data, is difficult, as in the most common MRI sequences (T1 and T2 weighted sequences) a clear boundary between the skull and the CSF is not visible as illustrated in Figures 1.11 and 1.12.

In CT scans (see Figure 1.10) the skull tissue is more visible than in

MRI, but due to the exposure of the patient to radiation, the use of CT is limited. In contrast, MRI only exposes the patient to a static magnetic field and is widely used with numerous sequences targeting different tissues. The MRI sequences that are often used in head modelling are the T1- and T2-weighted sequences (see Figures 1.11 and 1.12 respectively), but extracting the skull tissue from those sequences is in general difficult. A recent MRI sequence has been proposed in [106] that aims in better imaging the skull bone compared to the usual sequences.

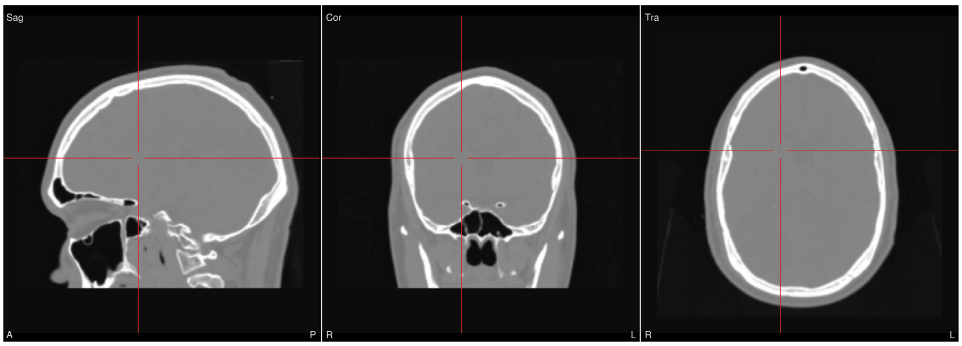

Figure 1.10: Sagittal, coronal and transverse slices of CT data.

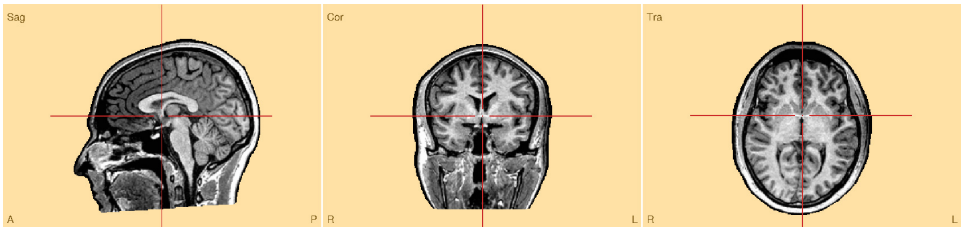

Figure 1.11: Sagittal, coronal and transverse slices of T1-weighted MRI data.

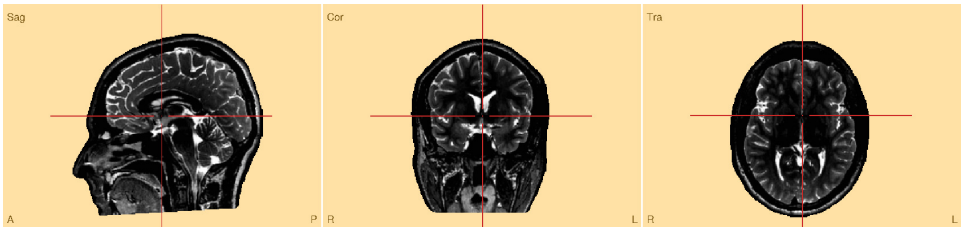

Figure 1.12: Sagittal, coronal and transverse slices of T2-weighted MRI data.

In [73] the influence of skull segmentation and modelling was investigated comparing a realistic head model that accounts for the internal skull structure (compacta and spongiosa) with various other head models. The reference model was constructed by improving the skull segmentation ob-

tained from MRI data with the skull geometry extracted from CT data. The generated head model was used to localize dipoles and its performance was compared to the model using the segmentation only from the MRI data, various skull simplifications, and models where anisotropy was considered. Their results showed that their isotropic heterogeneous skull model led to the lower localization errors. Their results also indicate that segmentation only based on MRI, introduced geometry errors that led to an increase in the average localization errors.

The influence of skull segmentation inaccuracies was also investigated in [65] compared to a reference model constructed from T1- and T2-weighted MRI data. Their results show that a simplification of the skull tissue to a single layer of constant thickness leads to significant (forward and inverse problem) errors, while limiting the head model directly below the skull (discarding any volume below) also leads to significant errors.

In the above studies [65,73,86,105], the conductivities of the tissues were fixed and the influence of the tissue geometry was investigated. Their results indicate the importance of the various tissues with respect to the selected conductivity values, however different results might be obtained selecting different conductivity values, see for example [2] where modelling the skull as a single compartment and assuming a different brain to skull conductivity ratio (80 instead of 25 in their reference model) the observed localization errors were up to $31\,mm$.

To better understand the influence of the various head tissues on the forward solution the authors in [101] considered a 3-layer realistic model, accounting for the scalp, skull (single layer) and brain tissues, and varied the conductivity values of all the tissues together. In their investigation, they also considered the skull to be anisotropic. Their global sensitivity analysis concluded that the ratio between the scalp and skull conductivities was the most influential, especially for shallow dipoles. Their anisotropy investigation showed that the effect of the skull conductivity comes from its radial component, while the tangential one had almost no effect.

In [84] the influence of skull conductivity misspecification is investigated, modelling the skull as a single layer and varying its conductivity in a wide range of values. They concluded that for an error of 20% in the skull conductivity the localization errors were acceptable (on average $3\,mm$). However, that investigation did not consider the internal skull structure (compacta and spongiosa). A second investigation (included in the same study) points out that the internal structure of the skull should be considered when modelling the human head.

In [28] individual head models that account for the layered skull structure were constructed by segmenting T1- and T2-weighted MRI data. Errors in the forward computations and the inverse dipole localization were measured while assuming the skull to be heterogeneous (layered structure with compacta and spongiosa), homogeneous (single layer) and anisotropic, while a

range of conductivity values and various proportions of spongiosa within the skull was also considered. The obtained results suggest that accounting for the layered structure of the skull is important, whereas assuming isotropic or anisotropic skull conductivity had little influence.

The influence of the tissue conductivities is also investigated using MEG measurements [50, 103, 108, 109].

Other sources of modelling errors may also affect the accuracy of the inverse solution. For example the location of the sensors on the scalp [2], the number of sensors [62] or even the position of the patient during the MRI acquisition and the EEG recording [87].

To conclude, both accurate tissue segmentation and conductivity values should be considered while modelling the human head. Among the various head tissues the skull has the strongest influence on the source localization results, due to its low conductivity and inhomogeneity. Therefore, conductivity estimation techniques are required to minimize the uncertainty of the unknown tissue conductivities. Apart from the mainly considered head tissues (scalp, skull and brain), CSF and the internal structure of the skull should also be considered in head models.

While realistic head models are able to capture better the complicated head geometry, in spherical models, analytical solutions can be obtained that can be used to validate the methods developed for the realistic head models.

PART I

Conductivity estimation in a spherical geometry

CHAPTER 2

Spherical models

In the previous chapter we discussed about the conductivity Poisson equation, that relates the electric potential to the source term through the conductivity of the medium.

In this chapter we will use the conductivity Poisson equation to solve the inverse conductivity problem in a bounded spherical domain that approximates the human head geometry.

Our goal here is to establish uniqueness and a constructive scheme for the inverse skull conductivity estimation problem using partial boundary EEG data, in the preliminary case of a homogeneous skull conductivity. The stability of the inverse problem is also considered.

The results of this chapter are published in [24].

Introduction to spherical models

We study an inverse conductivity recovery problem in the particular case of a spherical 3D domain Ω (a ball in $\mathbb{R}^3$) and for piecewise constant conductivity functions, of which one value is unknown. More precisely, we assume Ω to be made of 3 nested spherical layers, whose conductivity values are known in the innermost and outermost layers. We assume that the elliptic partial differential conductivity equation (conductivity PDE) holds with a given source term in divergence form supported in the innermost layer.

Provided a single measurement as a pair of Cauchy data on the boundary (open subset of the sphere $\partial\Omega$), we establish uniqueness and stability properties together with a reconstruction algorithm for the intermediate conductivity [24].

We will also perform some analysis in order to investigate robustness of the reconstruction with respect to available measurements and sources information.

We face a very specific version of the many inverse conductivity issues for second order elliptic PDE under study nowadays. This one is related to piecewise constant conductivities in a spherical geometry in $\mathbb{R}^3$, and set from a single (Cauchy pair of partial) boundary measurement. Similar inverse conductivity recovery problems may be formulated in more general (Lipschitz smooth) domains of arbitrary dimension, with more general conductivities. They are often considered from (several or) infinitely many boundary measurements (pairs of Cauchy data, related Dirichlet-to-Neumann operator), and are called after Calderón [60], or after medical imaging processes EIT (Electrical Impedance Tomography). Uniqueness and stability issues for conductivity recovery are deeply discussed in [4–6, 8, 32, 39, 53, 60, 97].

More general inverse problems for elliptic PDEs, in particular transmission issues, are discussed in [54, 61, 85]. Stability properties of Cauchy boundary value problems are described in [7] (see also references therein).

Typically, inverse conductivity recovery problems aim at determining an unknown conductivity value inside a domain Ω from measurements acquired on the boundary $\partial\Omega$. To solve the inverse conductivity recovery problems, we will assume that the potential u is given on an open subset Γ of $\partial\Omega$: $u\big|_{\Gamma} = g$, where g represents the given boundary data.

In practice (for example using EEG measurements) one usually has at his disposal pointwise values to solve the inverse problem (the measurements at a number of sensors). Estimating the continuous potential from the pointwise values, is not a trivial task and we will discuss this problem and its solutions in Chapter 3.

In general, the electrical potential u is solution to:

$$\nabla \cdot \big(\sigma \nabla u\big) = \mathcal{S} \text{ in } \mathbb{R}^3\,, \tag{2.1}$$

where σ is the unknown conductivity and $\mathcal{S}$ is a source term. The necessary assumptions for the above formula to make sense and its derivation from the Maxwell equations is already discussed in Chapter 1, Section 1.2.

In addition, the current flux $\sigma\partial_n u = 0$ is assumed to vanish on $\partial\Omega$ assuming that no current flux is present outside the domain Ω, as the conductivity of the air at $\mathbb{R}^3 \setminus \Omega$ surrounding the domain Ω is considered to be zero:

$$\sigma\big|_{\mathbb{R}^3\setminus\Omega} = 0\,.$$

In this setting we face the overdetermined boundary value problem being given u on Γ, recover the unknown value of σ in some part of Ω:

$$\begin{cases} \nabla \cdot (\sigma \nabla u) = \mathcal{S} \text{ in } \Omega \\ \sigma \nabla u \cdot n = 0 \text{ in } \partial\Omega\,. \end{cases} \tag{2.2}$$

Here and in the next chapter we will also investigate questions as: the existence of the skull conductivity for known sources inside the brain (the

solution may not exist); the uniqueness of the recovered value (there could be more than one conductivity value that explain the measured data); the stability of this reconstruction (the recovered conductivity value may change dramatically with slight changes in the measured data), and how to create constructive procedures that are robust (the proposed algorithm might introduce numerical errors to the solution for example due to the accuracy of the computations).

Quite frequently, for piecewise constant conductivities, the sub-domain (supporting the unknown conductivity value) is also to be determined, in some cases this is even more important than the constant conductivity value itself (for example for tumor detection, see [9, Ch. 3] and references therein, [58, 59]). But in the case of EEG, the sub-domains containing the various tissues can be considered known, because they can be extracted from Magnetic Resonance Images (MRI). And for simplicity, we only consider the inverse skull conductivity estimation problem in a three-layer spherical head geometry, using partial boundary EEG data. The dipolar sources positions and moments will be considered to be known. This may appear to be an unrealistic assumption because source reconstruction is itself a difficult inverse problem. But in fact, in some situations there are prior assumptions as to the positions of the sources (in primary evoked electrical potentials), and the position of a source also constrains its orientation, because to the laminar organization of pyramidal neurons in the grey matter. The source locations, for example, can be fixed in somatosensory evoked potentials (SEP) and fields (SEF) measurements by the SEF localisations, which might be considered mm-accurate and mainly independent of skull conductivity, see [15, 110].

Layered geometry and conductivity model

We consider the inverse conductivity estimation problem in a spherical domain $\Omega \subset \mathbb{R}^3$ made of 3 concentric spherical layers (centered at 0), a ball Ω_0, and 2 consecutive surrounding spherical shells Ω_1, Ω_2. Their respective boundaries are the spheres denoted as S_0, S_1, and S_2, with S_i of radius r_i such that $0 < r_0 < r_1 < r_2$. We also put $\Omega_3 = \mathbb{R}^3 \setminus \overline{\Omega} = \mathbb{R}^3 \setminus (\Omega \cup S_2)$.

For $i = 0, 1, 2$, we assume that σ is a real valued piecewise constant conductivity coefficient with values $\sigma_i > 0$ in Ω_i. Let also $\sigma_3 = 0$.

Note that in the present work, the values σ_i of the conductivity in Ω_i for $i \neq 1$ outermost layers Ω_0, Ω_2 are assumed to be known.

In the EEG framework and for spherical three-layer head models, the domains Ω_i respectively represent the brain, the skull and the scalp tissues for $i = 0, 1, 2$, as shown in Figure 2.1, see [48, 49]. There, under isotropic assumption, it holds that $0 < \sigma_1 < \sigma_0 \simeq \sigma_2$.

Throughout the present work, the geometry Ω and the conductivity σ will be assumed to satisfy the above assumptions. More general situations

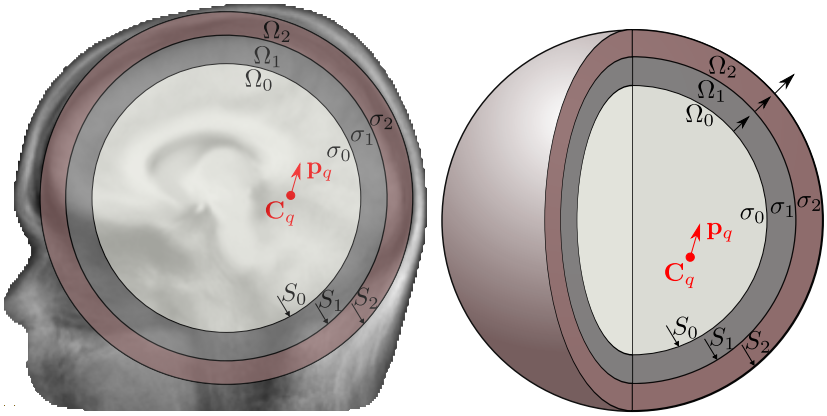

Figure 2.1: Spherical head model, with one source $\mathbf{C}_q$, $\mathbf{p}_q$.

are discussed in Section 3.3.3.

Conductivity estimation

We consider the following inverse conductivity estimation problem in the 3-layered spherical framework of Section 2.2. From (a single pair of) Cauchy boundary data $u = g$ in a (non-empty) open subset Γ of $\partial\Omega = S_2$ and $\partial_n u = 0$ on S_2 of a solution to (2.5), and from a (known) source term $\mathcal{S}$ given by (2.4), we want to recover the constant value σ_1 of the conductivity σ in the intermediate layer Ω_1.

Before, we still need to describe the PDE and associated boundary value problems in each of the consecutive layers Ω_i.

Model, assumptions

We consider the conductivity Laplace-Poisson partial differential equation (PDE) (2.1):

$$\nabla \cdot \big(\sigma \nabla u\big) = \mathcal{S} \text{ or } \operatorname{div}\big(\sigma \operatorname{grad} u\big) = \mathcal{S} \text{ in } \mathbb{R}^3\,, \tag{2.3}$$

(in the distributional sense), with a source term $\mathcal{S}$ taken to be a distribution on $\mathbb{R}^3$ compactly supported in Ω_0.

We investigate situations where source terms $\mathcal{S}$ are of divergence form:

$$\mathcal{S} = \nabla \cdot \mathbf{J}^P = \operatorname{div} \mathbf{J}^P\,,$$

for distributions $\mathbf{J}^P$ made of Q pointwise dipolar sources located at $\mathbf{C}_q \in \Omega_0$ with (non zero) moments $\mathbf{p}_q \in \mathbb{R}^3$:

$$\mathbf{J}^P = \sum_{q=1}^{Q} \mathbf{p}_q\, \delta_{\mathbf{C}_q}\,, \text{ whence } \mathcal{S} = \sum_{q=1}^{Q} \mathbf{p}_q \cdot \nabla \delta_{\mathbf{C}_q}\,, \tag{2.4}$$

where $\delta_{\mathbf{C}_q}$ is the Dirac distribution supported at $\mathbf{C}_q \in \Omega_0$. Therefore, in $\mathbb{R}^3$,

$$\nabla \cdot \big(\sigma \nabla u\big) = \sum_{q=1}^{Q} \mathbf{p}_q \cdot \nabla \delta_{\mathbf{C}_q} \,. \tag{2.5}$$

For the EEG case, under the quasi-static approximation and modeling the primary cerebral current $\mathbf{J}^P$ as in (2.4), Maxwell's equations imply that the conductivity PDE (2.5) drives the behaviour of the electric potential u [48].

Solution to Laplace-Poisson PDE

For each of the spherical layers $i = 0, 1, 2, 3$, write $u_{|\Omega_i} = u_i$ for the restriction to Ω_i of the solution u to (2.5). We put $\partial_n u_i$ for the normal derivative of u_i on spheres in $\overline{\Omega}_i$, the unit normal vector being taken towards the exterior direction (pointing to Ω_{i+1}). In the present spherical setting, we actually have $\partial_n = \partial_r$, as the direction of the unit normal vector coincides with the radial direction coming from the center of the circle.

For $i = 1, 2, 3$, the following Dirichlet and Neumann transmission conditions hold on S_{i-1}, in particular in $L^2(S_{i-1})$, see [17, 23, 36]:

$$u_{i-1} = u_i \,, \quad \sigma_{i-1}\, \partial_n u_{i-1} = \sigma_i\, \partial_n u_i \,.$$

Linked by those boundary conditions and under the piece-wise constant conductivity assumption, the solutions u_i to (2.5) in Ω_i satisfy the following Laplace and Laplace-Poisson equations:

$$\begin{cases} \Delta\, u_i = 0 \text{ in } \Omega_i \,, \;\; i > 0 \,, \\ \Delta\, u_0 = \dfrac{1}{\sigma_0} \displaystyle\sum_{q=1}^{Q} \mathbf{p}_q \cdot \nabla \delta_{\mathbf{C}_q} \text{ in } \Omega_0 \,. \end{cases} \tag{2.6}$$

The above derivation is shown in Section 1.2.4.

We will see (in Section 2.5) that the transmission from $\begin{bmatrix} u_i \\ \partial_n u_i \end{bmatrix}$ on S_i to $\begin{bmatrix} u_{i-1} \\ \partial_n u_{i-1} \end{bmatrix}$ on S_{i-1}, for $i = 1, 2$, may be written

$$\begin{bmatrix} u_{i-1} \\ \partial_n u_{i-1} \end{bmatrix}_{|S_{i-1}} = \begin{bmatrix} 1 & 0 \\ 0 & \frac{\sigma_i}{\sigma_{i-1}} \end{bmatrix} \mathcal{T}(S_{i-1}, S_i) \begin{bmatrix} u_i \\ \partial_n u_i \end{bmatrix}_{|S_i} .$$

for some operator $\mathcal{T}(S_{i-1}, S_i)$ that accounts for the harmonicity of u_i in Ω_i and that we will express using spherical harmonics, see Section 2.5.2.

Concerning the source term $\mathcal{S}$, note that it's knowledge only determines u_0 on S_0 up to the addition of a harmonic function in Ω_0. Indeed, by

convolution with a fundamental solution of Laplace equation in $\mathbb{R}^3$, we see that

$$u_s(\mathbf{x}) = \frac{1}{4\pi} \sum_{q=1}^{Q} \frac{< \mathbf{p}_q, \mathbf{x} - \mathbf{C}_q >}{|\mathbf{x} - \mathbf{C}_q|^3} \,, \mathbf{x} \notin \{\mathbf{C}_q\} \,, \tag{2.7}$$

satisfies $u_s(\mathbf{x}) \to 0$ at $|\mathbf{x}| \to \infty$,

$$\Delta\, u_s = \sum_{q=1}^{Q} \mathbf{p}_q \cdot \nabla \delta_{\mathbf{C}_q} \,,$$

in $\mathbb{R}^3$, whence in Ω and Ω_0, and $\Delta\, u_s = 0$ outside Ω_0. Solutions u_0 to (2.6) in Ω_0 are then provided by u_s/σ_0 up to the addition of a harmonic function in Ω_0.

Spherical harmonics expansions

In order to express harmonic functions in the spherical shells and balls Ω_i and their boundary values on S_i, we use the spherical harmonics basis $r^k\, Y_{km}(\theta, \varphi)$, $r^{-(k+1)}\, Y_{km}(\theta, \varphi)$, $k \geq 0$, $|m| \leq k$, in the spherical coordinates (r, θ, φ). These are homogeneous harmonic and anti-harmonic polynomials for which we refer to [13, Ch. 9, 10], [33, Ch. II, Sec. 7.3] as for their properties. The basis functions $Y_{km}(\theta, \varphi)$ are products between associated Legendre functions of indices $k \geq 0$, $|m| \leq k$, applied to $\cos\theta$ and elements of the Fourier basis of index m on circles in φ (real or complex valued, $\cos m\varphi$, $\sin m\varphi$ or $e^{\pm im\varphi}$).

Note that for $g \in L^2(S_2)$, we have the relations:

$$\|g\|^2_{L^2(S_2)} = \sum_{k,m} |g_{km}|^2 \,,$$

and:

$$\|\nabla g\|^2_{L^2(S_2, \mathbb{R}^2)} = \sum_{k,m} k(k+1) |g_{km}|^2 \,. \tag{2.8}$$

Here, g_{km} are the spherical harmonic coefficients of the expanded potential (g on S_2) on the spherical harmonic basis. This issue is discussed further in this section. Their definition is given in Appendix by equation (A.3).

Source term

The decomposition theorem [13, Thm 9.6], [33, Ch. II, Sec. 7.3, Prop. 6], is to the effect that the restriction u_i of u to Ω_i for $i = 1, 2$ may be expanded on the spherical harmonics basis as follows, at $(r, \theta, \varphi) \in \Omega_i$:

$$u_i(r,\theta,\varphi) = \sum_{k=0}^{\infty} \sum_{m=-k}^{k} \left[\alpha_{ikm} r^k + \beta_{ikm} r^{-(k+1)}\right] Y_{km}(\theta,\varphi) \in \Omega_i\,, \qquad (2.9)$$

where α_{ikm} and β_{ikm} are the spherical harmonic coefficients of the harmonic and anti-harmonic parts of u_i, respectively (harmonic inside or outside $\cup_{j\le i}\Omega_i$). Similarly, because it is harmonic in a spherical layer surrounding S_0, the restriction u_0 of u to Ω_0 is given at points (r,θ,φ) with $r > \max_q |\mathbf{C}_q| > 0$ by

$$u_0(r,\theta,\varphi) = \sum_{k=0}^{\infty} \sum_{m=-k}^{k} \alpha_{0km} r^k\, Y_{km}(\theta,\varphi) + u_s(r,\theta,\varphi)\,,$$

where u_s given by (2.7) is expanded there as: $r^{-(k+1)}\, Y_{km}(\theta,\varphi)$:

$$u_s(r,\theta,\varphi) = \sum_{k,m} \beta_{0km} r^{-(k+1)} Y_{km}(\theta,\varphi)\,. \qquad (2.10)$$

Here, β_{0km} are the spherical harmonic coefficients of the anti-harmonic (harmonic outside Ω_0) function u_S. Their definition is given in Appendix by equation (A.4).

Boundary data on spheres

The normal derivative of u_i, $i = 0,1,2$, is then given in Ω_i (with $r > \max_q |\mathbf{C}_q|$ for $i = 0$) by:

$$\partial_n u_i(r,\theta,\varphi) = \sum_{k,m} \left[\alpha_{ikm} k r^{k-1} - \beta_{ikm}(k+1) r^{-(k+2)}\right] Y_{km}(\theta,\varphi) \qquad (2.11)$$

On S_i, we put (because $u_i \in L^2(S_i)$ where the spherical harmonics form an orthogonal basis [13, Thm 5.12]):

$$u_i(r_i,\theta,\varphi) = \sum_{k=0}^{\infty} \sum_{m=-k}^{k} \gamma_{ikm} Y_{km}(\theta,\varphi)\,,\ \partial_n u_i(r_i,\theta,\varphi) = \sum_{k=0}^{\infty} \sum_{m=-k}^{k} \delta_{ikm} Y_{km}(\theta,\varphi)\,,$$

with l^2 summable coefficients γ_{ikm}, δ_{ikm} (that may be real or complex valued depending on the choice for Y_{km}).

Assuming that u is given at the full $\partial\Omega = S_2$ or already extended from Γ to S_2 (see [11,23] and the discussion in Section 3.1.1), we have that $u_2 = g$:

$$u_2(r_2,\theta,\varphi) = \sum_{k,m} \gamma_{2km} Y_{km}(\theta,\varphi) = \sum_{k,m} g_{km} Y_{km}(\theta,\varphi) = g(\theta,\varphi)\,,$$

for $g \in L^2(S_2)$. Then $g_{km} = \gamma_{2km}$, whereas the corresponding $\delta_{2km} = 0$ since $\partial_n u_2 = 0$ on S_2 (because $\sigma_3 = 0$).

Transmission conditions

Matrix form

Below, we write for sake of simplicity, for $i = 0, 1, 2$: $\alpha_{ik} = \alpha_{ikm}$, $\beta_{ik} = \beta_{ikm}$, $\gamma_{ik} = \gamma_{ikm}$, $\delta_{ik} = \delta_{ikm}$, $g_k = g_{km}$, for all $k \geq 0$, and every $|m| \leq k$ (we could also take the sums over $|m| \leq k$).

Recall from Section 2.3.2 that the following transmission conditions hold on S_{i-1} for $i = 1, 2, 3$:

$$\Sigma_{i-1} \begin{bmatrix} u_{i-1} \\ \partial_n u_{i-1} \end{bmatrix}_{|S_{i-1}} = \Sigma_i \begin{bmatrix} u_i \\ \partial_n u_i \end{bmatrix}_{|S_{i-1}}, \tag{2.12}$$

with

$$\Sigma_i = \begin{bmatrix} 1 & 0 \\ 0 & \sigma_i \end{bmatrix} \text{ hence } \Sigma_i^{-1} = \begin{bmatrix} 1 & 0 \\ 0 & \frac{1}{\sigma_i} \end{bmatrix} \text{ and } \sigma_i \Sigma_i^{-1} = \begin{bmatrix} \sigma_i & 0 \\ 0 & 1 \end{bmatrix}.$$

By projection of (2.9), (2.11), onto (the orthogonal $L^2(S_i)$ basis of) spherical harmonics, and with

$$T_k(r_i) = \begin{bmatrix} r_i^k & r_i^{-(k+1)} \\ k r_i^{k-1} & -(k+1) r_i^{-(k+2)} \end{bmatrix},$$

we obtain for all $k \geq 0$ the following relations on S_i:

$$\begin{bmatrix} \gamma_{ik} \\ \delta_{ik} \end{bmatrix} = T_k(r_i) \begin{bmatrix} \alpha_{ik} \\ \beta_{ik} \end{bmatrix}.$$

In particular:

$$\beta_{ik} = \frac{r_i^{k+1}}{2k+1} (k \gamma_{ik} - \delta_{ik}). \tag{2.13}$$

The transmission conditions (2.12) through S_{i-1} express as:

$$\Sigma_{i-1} \begin{bmatrix} \gamma_{i-1k} \\ \delta_{i-1k} \end{bmatrix} = \Sigma_i T_k(r_{i-1}) \begin{bmatrix} \alpha_{ik} \\ \beta_{ik} \end{bmatrix}.$$

Because $T_k(r_i)$ is invertible ($r_i > 0$), this implies that:

$$\begin{bmatrix} \gamma_{i-1k} \\ \delta_{i-1k} \end{bmatrix} = \Sigma_{i-1}^{-1} \Sigma_i T_k(r_{i-1}) T_k(r_i)^{-1} \begin{bmatrix} \gamma_{ik} \\ \delta_{ik} \end{bmatrix}.$$

Therefore, in the spherical geometry, $\mathcal{T}(S_{i-1}, S_i) = T_k(r_{i-1}) T_k(r_i)^{-1}$ for the operator $\mathcal{T}(S_{i-1}, S_i)$ introduced at the end of Section 2.3.2.

Hence, because $\gamma_{2k} = g_k$ and $\delta_{2k} = 0$ (see Section 2.4.2):

$$\begin{bmatrix} \gamma_{0k} \\ \delta_{0k} \end{bmatrix} = \Sigma_0^{-1}\,\Sigma_1\,T_k(r_0)\,T_k(r_1)^{-1}\,\Sigma_1^{-1}\,\Sigma_2\,T_k(r_1)\,T_k(r_2)^{-1} \begin{bmatrix} g_k \\ 0 \end{bmatrix}, \qquad (2.14)$$

while

$$\beta_{0k} = [0\ 1]\,T_k(r_0)^{-1} \begin{bmatrix} \gamma_{0k} \\ \delta_{0k} \end{bmatrix}. \qquad (2.15)$$

These formula express a linear relation between the source term coefficients β_{0k} and the boundary Dirichlet data with coefficients g_k, which is studied in Appendix and gives rise to (2.16) below. A graphical demonstration of the above relation showing the data transmission over the spherical interfaces is presented in Figure 2.2. We already see the particular role of σ_1 that appears through Σ_1^{-1} and Σ_1. This explains why, after multiplication by σ_1 and algebraic manipulations, we obtain in (2.16) a polynomial of degree 2 in σ_1.

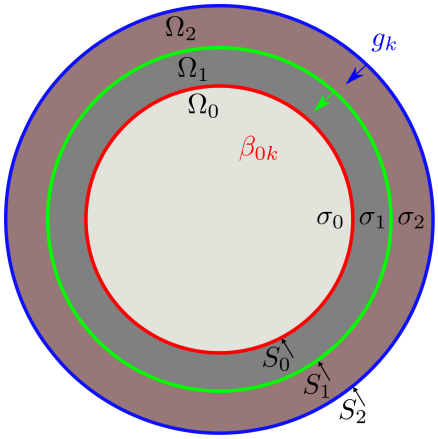

Figure 2.2: Data transmission from S_2 to S_0 between the source term coefficients β_{0k} and the boundary Dirichlet data with coefficients g_k.

Algebraic equations

Let us now derive the polynomial of degree 2 in σ_1. From (2.14), (2.15), we get for all $k \geq 0$,

$$\beta_{0k} = g_k \times$$
$$[0\ 1]\,T_k(r_0)^{-1}\,\Sigma_0^{-1}\,\Sigma_1\,T_k(r_0)\,T_k(r_1)^{-1}\,\Sigma_1^{-1}\,\Sigma_2\,T_k(r_1)\,T_k(r_2)^{-1} \begin{bmatrix} 1 \\ 0 \end{bmatrix}.$$

The matrices $T_k(r_i)$ and $T_k(r_j)^{-1}$ can be written:

$$T_k(r_i) = \begin{bmatrix} 1 & 0 \\ 0 & \frac{1}{r_i} \end{bmatrix} \begin{bmatrix} 1 & 1 \\ k & -(k+1) \end{bmatrix} \begin{bmatrix} r_i^k & 0 \\ 0 & r_i^{-(k+1)} \end{bmatrix},$$

$$T_k(r_j)^{-1} = \frac{1}{2k+1} \begin{bmatrix} r_j^{-k} & 0 \\ 0 & r_j^{(k+1)} \end{bmatrix} \begin{bmatrix} k+1 & 1 \\ k & -1 \end{bmatrix} \begin{bmatrix} 1 & 0 \\ 0 & r_j \end{bmatrix} .$$

Their products that give an expression of $\mathcal{T}(S_{i-1}, S_i)$ in the spherical geometry are then such that:

$$T_k(r_{i-1})\, T_k(r_i)^{-1} = \frac{1}{2k+1} \times$$

$$\begin{bmatrix} 1 & 0 \\ 0 & r_{i-1}^{-1} \end{bmatrix} \begin{bmatrix} 1 & 1 \\ k & -(k+1) \end{bmatrix} \begin{bmatrix} \left(\frac{r_{i-1}}{r_i}\right)^k & 0 \\ 0 & \left(\frac{r_i}{r_{i-1}}\right)^{k+1} \end{bmatrix} \begin{bmatrix} k+1 & 1 \\ k & -1 \end{bmatrix} \begin{bmatrix} 1 & 0 \\ 0 & r_i \end{bmatrix}$$

$$= \frac{1}{2k+1} \left(\frac{r_i}{r_{i-1}}\right)^{k+1} \times$$

$$\begin{bmatrix} 1 & 0 \\ 0 & r_{i-1}^{-1} \end{bmatrix} \begin{bmatrix} 1 & 1 \\ k & -(k+1) \end{bmatrix} \begin{bmatrix} \left(\frac{r_{i-1}}{r_i}\right)^{2k+1} & 0 \\ 0 & 1 \end{bmatrix} \begin{bmatrix} k+1 & 1 \\ k & -1 \end{bmatrix} \begin{bmatrix} 1 & 0 \\ 0 & r_i \end{bmatrix} .$$

We can write

$$T_k(r_{i-1})\, T_k(r_i)^{-1} = \rho_k^{(i)} \begin{bmatrix} a_k^{(i)} & b_k^{(i)} \\ c_k^{(i)} & d_k^{(i)} \end{bmatrix} ,$$

with

$$\rho_k^{(i)} = \frac{1}{2k+1} \left(\frac{r_i}{r_{i-1}}\right)^{k+1} , \; i = 1, 2 , \; \rho_k^{(0)} = \frac{r_0^{k+1}}{2k+1} ,$$

and the real valued quantities, with their equivalent asymptotic behaviours as $k \to \infty$:

$$\begin{cases} a_k^{(i)} = (k+1) \left(\frac{r_{i-1}}{r_i}\right)^{2k+1} + k & \sim k , \\ b_k^{(i)} = r_i \left[\left(\frac{r_{i-1}}{r_i}\right)^{2k+1} - 1\right] & \sim -r_i , \\ c_k^{(i)} = \frac{k\,(k+1)}{r_{i-1}\, r_i}\, b_k^{(i)} & \sim -\frac{k^2}{r_{i-1}} , \\ d_k^{(i)} = \frac{r_i}{r_{i-1}} \left[k \left(\frac{r_{i-1}}{r_i}\right)^{2k+1} + k + 1\right] & \sim \frac{k r_i}{r_{i-1}} . \end{cases}$$

Define also the real valued quantities $e_k^{(0)}$, $f_k^{(0)}$:

$$e_k^{(0)} = k , \; f_k^{(0)} = f^{(0)} = -r_0 .$$

We have

$$[0 \; 1]\, T_k(r_0)^{-1} = \rho_k^{(0)} \begin{bmatrix} e_k^{(0)} & f_k^{(0)} \end{bmatrix} .$$

Then, for all $k \geq 0$, equations (2.14), (2.15) can be rewritten as:

$$B_1(k)\,\sigma_1\,\beta_{0k} = \left(A_2(k)\,\sigma_1^2 + A_1(k)\,\sigma_1 + A_0(k)\right)\,g_k\,, \tag{2.16}$$

and holds true with:

$$B_1(k) = \frac{\sigma_0}{\rho_k^{(0)}\,\rho_k^{(1)}\,\rho_k^{(2)}} \text{ whence } r_0^{k+1}\,B_1(k) = \sigma_0\,(2k+1)^3\,\left(\frac{r_0}{r_2}\right)^{k+1} \sim 8k^3\left(\frac{r_0}{r_2}\right)^{k+1},$$

and

$$\begin{cases} A_1(k) = \sigma_0\,e_k^{(0)}\,a_k^{(1)}\,a_k^{(2)} + \sigma_2\,f_k^{(0)}\,d_k^{(1)}\,c_k^{(2)} & \sim k^3(\sigma_0+\sigma_2)\,, \\ A_2(k) = f_k^{(0)}\,c_k^{(1)}\,a_k^{(2)} & \sim k^3\,, \\ A_0(k) = \sigma_0\,\sigma_2\,e_k^{(0)}\,b_k^{(1)}\,c_k^{(2)} & \sim k^3\sigma_0\sigma_2\,. \end{cases}$$

Observe that $r_0^{k+1}\,B_1(k)$ acts on $r_0^{-(k+1)}\,\beta_{0k}$ that are members of an l^2 sequence (see Section 2.4.1 and equation (2.13) with $i = 0$).

One can show with the above expressions that the behaviours of the ratios $A_i(k)/A_2(k)$, $B_1(k)/A_2(k)$ ensure that they all are uniformly bounded from below or from above by positive constants, for $k > 0$.

Note also that

$$\begin{cases} B_1(k) = \sigma_0\,\tilde{B}_1(k)\,, \\ A_1(k) = \sigma_0\,\tilde{A}_{10}(k) + \sigma_2\,\tilde{A}_{12}(k)\,, \\ A_2(k) = \tilde{A}_2(k)\,, \\ A_0(k) = \sigma_0\,\sigma_2\,\tilde{A}_0(k)\,, \end{cases}$$

where $\tilde{A}_i$, $\tilde{A}_{ij}$, $\tilde{B}_1$ only depend on the spherical geometry.

Therefore, equation (2.16) is composed of non negative quantities $A_i(k)$, $i = 0, 1, 2$, $B_1(k)$ that depend only on the geometry, on the given conductivity values σ_0, σ_2, and on k. Actually, $A_1(k), B_1(k) > 0$ for all $k \geq 0$ while $A_0(k), A_2(k) > 0$ for $k > 0$ but $A_0(0) = A_2(0) = 0$. In particular, for all $k \geq 0$ and for $\sigma_1 > 0$, we have $A_2(k)\,\sigma_1^2 + A_1(k)\,\sigma_1 + A_0(k) > 0$.

This implies that $\beta_{0k} = 0 \Leftrightarrow g_k = 0$ and that for all k such that $g_k \neq 0$, β_{0k}/g_k is real valued positive: the spherical harmonics basis diagonalizes the transmission relations.

Note that Equation (2.16) is the one on which relies our conductivity estimation result, but also the data transmission step (see Section 3.1.2).

Uniqueness result

Recall that the geometry Ω and the conductivity coefficients satisfy the hypotheses of Section 2.2. Let $\Gamma \subset S_2$ be a (non empty) open set.

Assume the source term $\mathcal{S}$ given by (2.4) to be known, and not to be reduced to a single dipolar pointwise source located at the origin ($\mathcal{S} \neq \mathbf{p} \cdot \nabla \delta_{\mathbf{0}}$).

Theorem 1 *Let σ, σ' be piecewise constant conductivities in Ω associated to two values σ_1, σ_1' in Ω_1 and equal values σ_0, σ_2 in Ω_0, Ω_2. If two solutions u, u' to (2.5) associated with σ, σ' and such that $\partial_n u = \partial_n u' = 0$ on S_2 coincide on Γ: $u_{|\Gamma} = u'_{|\Gamma}$, then $\sigma_1 = \sigma_1'$.*

This implies that a single pair of partial boundary Dirichlet data $u_{|\Gamma}$ on Γ and Neumann data $\partial_n u = 0$ (vanishing) on S_2 of a solution u to (2.5) uniquely determines $\sigma_1 > 0$.

As the proof in [24, Sec. 3.3] shows, source terms $\mathcal{S}$ that guarantee uniqueness are such that associated Dirichlet data $u_{|\Gamma}$ on Γ do not identically vanish. Notice also that if no source is present, uniqueness fails (boundary data identically vanish on S_2). However, Theorem 1 would also hold true for non identically vanishing Neumann data on S_2.

Stability properties

We now present a stability result for the inverse conductivity estimation problem with respect to the source term whenever $\Gamma = S_2$. The proof of the stability result can be found in [24, Sec. 3.4].

Proposition 1 *Assume the source terms $\mathcal{S}$, $\mathcal{S}'$ and the conductivities σ, σ' to satisfy the assumptions of Theorem 1. Let u_s, u_s' be the associated potentials through (2.7). Let u, u' be the associated solutions to (2.5) such that $\partial_n u = \partial_n u' = 0$ on S_2. Let g, g' be their boundary values on S_2. Then, there exist c, $c_s > 0$ such that*

$$\left|\sigma_1 - \sigma_1'\right| \leq c \left\| g - g' \right\|_{L^2(S_2)} + c_s \left\| u_s - u_s' \right\|_{L^2(S_0)} .$$

Whenever $0 < s_m \leq \sigma_1$, $\sigma_1' \leq s_M$ for constants s_m, s_M, then c, c_s do not depend on σ_1 , σ_1' but on s_m, s_M.

Remark 1 *For ordered lists of sources $(\mathbf{p}_q, \mathbf{C}_q)$, $(\mathbf{p}_q', \mathbf{C}_q')$ with length Q, we can define the geometric distance*

$$d(\mathcal{S}, \mathcal{S}') = \sum_{q=1}^{Q} \left(|\mathbf{p}_q - \mathbf{p}_q'| + |\mathbf{C}_q - \mathbf{C}_q'| \right) .$$

If the sources are located far enough from S_0 in the sense that $\max(|\mathbf{C}_q|, |\mathbf{C}'_q|) \leq \rho < r_0$, *and because u_s is on S_0 a continuous function of $\mathbf{p}_q, \mathbf{C}_q$, we can rewrite the inequality in Proposition 1 as:*

$$\left|\sigma_1 - \sigma'_1\right| \leq c \, \|g - g'\|_{L^2(S_2)} + c'_s \; d(\mathcal{S}, \mathcal{S}') \, ,$$

with $c'_s = K(\rho)\, c_s$ for some constant $K(\rho)$ which depends on ρ. Hence, the conductivity σ_1 depends continuously on the (complete) Dirichlet boundary data g (in $L^2(S_2)$) and on the source term $\mathcal{S}$, with appropriate topology.

Notice also the relation:

$$\beta_{0km} = \frac{1}{2k+1} \sum_{q=1}^{Q} \langle \mathbf{p}_q \, , \, \nabla \left(r^k \, Y_{km}(\theta, \varphi) \right) (\mathbf{C}_q) \rangle_{L^2(S_0)} \, .$$

Finally, observe that the constants c, c_s, c'_s in the above inequalities also depend on the data g' whence on $\mathcal{S}'$. The dependence between Dirichlet data g' on S_2 and the source term $\mathcal{S}'$ can be precised by using, for instance, the last equality together with relation (2.16) *between their coefficients (g'_k) and (β_{0k}), and then recalling the assumption $s_m \leq \sigma'_1 \leq s_M$.*

CHAPTER 3

Application to EEG

Previously, we solved the inverse skull conductivity estimation problem from the available EEG partial boundary data, expanded on the spherical harmonics basis, and transmitted over the spherical interfaces by transfer functions, while we considered that the source term is known. The stability of the inverse problem was also considered.

In this chapter we construct a reconstruction algorithm for the above inverse conductivity problem in EEG. A numerical analysis is then performed using simulated EEG data and source activity of various source configurations, expanded on spherical harmonic basis. The behaviour and the robustness of our algorithm is investigated over various source configurations and by introducing errors either to the EEG measurements or on the source term. Agreement of the conductivity estimation results with the theoretical stability properties of the problem is discussed.

FindSources3D

FindSources3D[1] (FS3D) is a Matlab software solving the inverse source localization problem in EEG in the layered spherical geometry of Section 2.2, see also [23]. It estimates pointwise dipolar current sources from pointwise measurement acquired by electrode on the surface of the scalp. It incorporates in particular the following functionalities.

Expansion of pointwise EEG data

EEG measurements can be used to solve the inverse conductivity problem. These can be modelled as pointwise values of the potential u obtained on

[1] See http://www-sop.inria.fr/apics/FindSources3D/.

the upper part of the scalp $\Gamma \subset \partial\Omega$, at a number N_e of electrode locations $\mathbf{r}_i$ (the location of the electrodes of the EEG cap):

$$u(\mathbf{r}_i) \simeq g_i \,,\ \mathbf{r}_i \in \Gamma \,. \tag{3.1}$$

Solving the inverse estimation problems from the given pointwise values g_i is not trivial and usually involves estimating the continuous potential values g on the whole $\partial\Omega$ from the values g_i [23, Sec. 3 and App. A].

The potential u is estimated from its values at the electrode locations in (3.1). The EEG case is then summarised by (2.2) together with (3.1).

The computation of the function g on S_2 from the pointwise values g_i of g at electrode locations $\mathbf{r}_i$ is actually an ill posed problem which needs to be regularized in order to be solved. First, it does not admit a unique solution. Next, we must take care about the fact that the values g_i may be corrupted by measurement (and modelling) errors.

A solution is to set this interpolation/extrapolation issue as a best constrained approximation problem in a suitable class of function. This is usually called Tykhonov regularization process. Such a procedure for the overall cortical mapping transmission step is described in [23, App. A], see also reference therein. We will discuss it shortly in Section 3.1.2. It uses boundary element methods and can be applied in realistic layered geometries, using for example tools such as OpenMEEG [46].

In the present spherical setting, we make use of the spherical harmonic basis (see Section 2.4) in order to formulate the problem as in [11], where it is shown to be well-posed (best constrained approximation).

The function g on S_2 is expressed as a truncated sum over the spherical harmonic basis:

$$g(r_2, \theta, \varphi) = \sum_{k,m} g_{km} Y_{km}(\theta, \varphi) \,, \tag{3.2}$$

where $k = 1, \ldots, K$ ($|m| \leq k$).

Usually in EEG the potentials are recorded[2] at a set of N_e electrode locations, between 64 and 128. The problem is then to find the spherical harmonic coefficients g_{km} from the pointwise measurements g_i at electrode locations $\mathbf{r}_i$ at the upper part of the scalp, with $i = 1, \ldots, N_e$. It can be written in a linear form as:

$$[g_i] = M[g_{km}] \,, \tag{3.3}$$

where $[g_i] \in \mathbb{R}^{N_e}$, $[g_{km}] \in \mathbb{R}^{(K+1)^2}$ and M is a matrix of size $N_e \times (K+1)^2$ which maps the spherical harmonic coefficients of g onto its pointwise values at $\mathbf{r}_i = (r_2, \theta_i, \varphi_i)$, whose entries are given by $Y_{km}(\theta_i, \varphi_i)$.

[2]The EEG measurements are in fact acquired over a period of time and in this work, we treat them at a fixed time instant as static data. We do not precise the actual time treatment which consist in separation and combination of time independent components (of MUSIC type [75]).

For a number $K \geq 30$ the above linear system becomes undetermined, as the number N_e of measurements is smaller than the number of basis functions (which in total is $(K+1)^2$ for all indices k and m), and should be constrained.

Using the relation (2.8) we compute the coefficients $[g_{km}]$ by solving the equality (3.3) and minimizing the quadratic criterion (2.8). The above is thus summarized by:

$$\begin{cases} \min\limits_{[g_{km}]} \sum\limits_{k,m} k(k+1)|g_{km}|^2 \,, \\ M[g_{km}] = [g_i] \,. \end{cases} \tag{3.4}$$

Transmission between scalp and cortex

The "cortical mapping" step consist in data transmission from the scalp to the cortex, described in [23, Sec. 3] on the spherical harmonic coefficients (obtaining β_{0km} from g_{km}).

Within FS3D and with the purpose of source estimation, this is actually performed using formula (2.16) as a "parametrization" of:

$$[g_{km}] = T_{map}[\beta_{0km}] \,, \tag{3.5}$$

where, for $k \geq 0$,

$$T_{map} = T_{map}(k) = \frac{B_1(k)\,\sigma_1}{A_2(k)\,\sigma_1^2 + A_1(k)\,\sigma_1 + A_0(k)} \,.$$

This step could be done either after (3.4) or as a parametrization directly incorporated into (3.4). We will mainly use the latter in our study (unless stated otherwise).

Source localization

Source localization from EEG data is the primary aim of the software FindSources3D. It requires the conductivity values and the spherical head geometry to be given. The anti-harmonic part u_s of the potential in the brain (see (2.7), (2.9)) is computed on S_0 and its squared values are quadratically approximated on circles by rational functions in [23]. The poles of these rational functions are then post processed, in order to furnish the quantity Q of the sources and an approximation of $\mathbf{C}_q$, $\mathbf{p}_q$. The idea behind this process is that u_s^2 can be extended from circles to disks in a function of the complex variable whose singularities are linked to the source locations $\mathbf{C}_q$. The poles of the best rational approximants in the disk are close to those singularities that they allow to estimate. More precisely, the sphere (brain) is scanned into series of parallel planar cross sections, in various directions. On each of these cross sections, u_s^2 extends into a function of the

complex variable of which the "planar singularities" in the corresponding disk are well approximated by the poles of the best rational approximant (in quadratic norm, on the circle). Observe that the suitable degree of the rational approximant (the smallest degree of the denominator that produces a sufficiently small error) indicates the quantity of sources. These singularities, hence the corresponding poles, superimpose ones onto the others along the parallel sections, in order to form lines. Changing the direction will furnish some other lines and they will intersect all together at the sources locations. A post treatment is then applied, that consists in a clustering algorithm followed by a dipole fitting procedure for each source.

Reconstruction algorithm for σ_1

Measurements of the Dirichlet data g on the scalp S_2 (pointwise values at electrodes locations) and known sources activity are expanded on the spherical harmonics basis. We therefore have at our disposal the spherical harmonics coefficients (g_{km}, β_{0km}) for $0 \leq k \leq K$ for some $K > 0$ and $|m| \leq k$.

As the reconstruction of the conductivity σ_1 does not depend on the spherical harmonics indices m (see Section 2.5), in order to increase the robustness of our reconstruction algorithm, the following normalization is applied over the different spherical harmonics indices k:

$$\begin{cases} \tilde{g}_k = \displaystyle\sum_{|m|\leq k} g_{km}\, \bar{\beta}_{0km}\,, \\ \tilde{\beta}_{0k} = \displaystyle\sum_{|m|\leq k} \beta_{0km}\, \bar{\beta}_{0km} = \sum_{|m|\leq k} |\beta_{0km}|^2\,. \end{cases} \tag{3.6}$$

There, $\bar{\beta}_{0km}$ is the complex conjugate number to β_{0km} (indeed, β_{0km} could be complex valued if the basis elements Y_{km} are taken in their complex valued form). Using the above normalization, both the $\tilde{\beta}_{0k}$ coefficients become real valued and the number of polynomial equations to be solved is reduced to only $K+1$ equations.

Let us rewrite equation (2.16) in the following error equation:

$$\varepsilon_k(\sigma_1, \tilde{\beta}_{0k}, \tilde{g}_k) = B_1(k)\,\sigma_1\,\tilde{\beta}_{0k} - \big(A_2(k)\,\sigma_1^2 + A_1(k)\,\sigma_1 + A_0(k)\big)\;\tilde{g}_k\,. \tag{3.7}$$

The conductivity reconstruction procedure is a least square minimization of the error equation as a truncated finite sum for $K > 0$:

$$\sigma_1^{est} \;=\; \arg\min_s \sum_{k=0}^{K} \Big|\varepsilon_k(s, \tilde{\beta}_{0k}, \tilde{g}_k)\Big|^2\,. \tag{3.8}$$

Numerical illustrations

We consider the EEG framework in the spherical three-layer head model, as described in Section 2.2, where the layers represent the brain, the skull and the scalp tissues, respectively. The typical dimensions used for the three concentric spheres are 8 cm for brain radius, 5 mm for skull thickness, and 7 mm for scalp thickness [10, 90]. In our numerical analysis the above values are normalized, leading to the radii $r_0 = 0.87$, $r_1 = 0.92$, and $r_2 = 1$ as in [23]. The brain and scalp tissue conductivities are set to $\sigma_0 = \sigma_2 = 0.33\,\mathrm{S/m}$, while the skull conductivity σ_1 is to be recovered. When generating simulated EEG data through the associated forward simulation, we will set $\sigma_1 = 0.0042\,\mathrm{S/m}$.

Our study uses simulated data associated to a single or multiple dipoles and the minimization of the criterion (3.8) for the conductivity estimation. The algorithm is written as a MATLAB code and takes as input a pair of spherical harmonics coefficients $\tilde{g}_k$ (expanded EEG measurements) and $\tilde{\beta}_{0k}$ (expanded source activity), computed in the FS3D software (either following the process in Section 3.1.1 or in Section 3.1.2) for $0 \leq k \leq K = 30$. The forward simulations are run with the FS3D software (unless stated otherwise) generating potential values at a set of 64 electrode locations on the upper part of the scalp. The inverse source localization functionality of FS3D (see Section 3.1.3) is fully used in Section 3.3.1 to estimate the source location and moment from a given set of potential values.

Usually, the measurements recorded during an EEG experiment are subject to some ambient noise and measurement errors, and the a priori knowledge on the sources is not perfect. The inverse conductivity estimation problem is sensitive to such perturbations though it possesses the stability property described in Proposition 1. To investigate the robustness of our algorithm in accordance with the stability property of the inverse conductivity estimation problem a number of investigations are performed in addition to those contained in [24].

First we examine the robustness of our algorithm in recovering the unknown conductivity from estimated source locations at different brain lobes (i.e. not perfectly known source locations). Then the robustness of our algorithm is investigated with respect to measurement errors (i.e. noise at the sensors level) and the source properties, simulating scenarios for a plethora of inexact source locations and inexact source moments.

Let us consider three different source terms each made of a single dipole located in the brain at: $\mathbf{C}_1 = (0.019, 0.667, 0.1)$, $\mathbf{C}_2 = (0.012, 0.426, 0.064)$ and $\mathbf{C}_3 = (0.003, 0.112, 0.017)$ respectively. The first is mimicking an EEG source at the frontal lobe (source configuration listed in Table 3.2) whereas the other two are shifted versions of the first towards the center of Ω_0 at $O = (0, 0, 0)$. Consider the line segment $l = (O, C_{S_0})$ between O and a point C_{S_0} (on the surface S_0) passing through $\mathbf{C}_1$ (length equal to the r_0

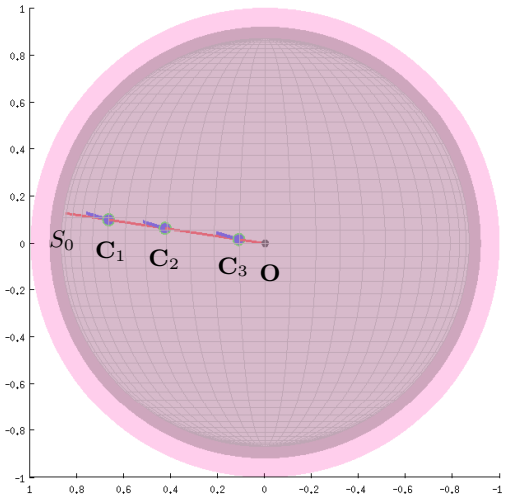

Figure 3.1: Dipolar source $\mathbf{C}_1$, $\mathbf{C}_2$, $\mathbf{C}_3$ sharing the same moment $\mathbf{p}_1$ (blue), aligned on the same radius (red) of S_0 in Ω_0.

radius). The sources are located at $\mathbf{C}_1, \mathbf{C}_2, \mathbf{C}_3 \in l$ and share the same moment $\mathbf{p}_1 = (0.027, 0.959, 0.28)$ as illustrated in Figure 3.1.

Behaviour with respect to various dipole configurations

We validate our reconstruction algorithm using simulated EEG data and source terms, of various single and double dipole configurations. The EEG data were simulated using FS3D software for solving the direct EEG problem with dipoles that were placed at locations $\mathbf{C}_i^{act}$, within different brain lobes, and at locations $\mathbf{C}_1, \mathbf{C}_2$ and $\mathbf{C}_3$. As the FS3D software is going to be used later for estimating the sources, using it to solve both for the forward and the inverse problem, it might lead to biased results. Therefore, EEG data were also simulated using the BESA simulator[3] for the same configuration (sources, geometry, conductivities and electrode locations) used in FS3D.

In the following investigations the EEG data will be expanded on spherical harmonic basis using either equation (3.4) or (3.5). As we will see, the expansion using equation (3.4), introduce a significant amount of errors to the computed spherical harmonics coefficients g_{km}, compared to the method based on equation (3.5). This is due to the fact that the minimization problem solved by (3.4) aims at finding the spherical harmonic coefficients that best fit the EEG given data, while using equation (3.5) carries additional information about the sources and the layered geometry that make the com-

[3]See http://www.besa.de/downloads/besa-simulator/.

putations much more precise.

Known source terms

First, the simulated EEG measurements where processed using the FS3D software, computing the spherical harmonics coefficients g_{km} of the measurements using equation (3.4), while also computing the spherical harmonics coefficients β_{0km} of the given source term. We perform conductivity estimation from the pair of normalized coefficients $\tilde{g}_k$ and $\tilde{\beta}_{0k}$, for each source configuration, see Section 3.2 and equation (3.6). The estimated conductivities for each source configuration is listed in Table 3.1.

Configuration	Src	Model	σ_1^{est}	Rel. Err.	Rel. EEG Err.
Frontal lobe	1	BESA	2.905e-03	3.082e-01	1.925e-01
Frontal lobe	1	FS3D	2.879e-03	3.145e-01	1.848e-01
Left occipital	1	BESA	1.871e-03	5.546e-01	2.141e-01
Left occipital	1	FS3D	2.026e-03	5.177e-01	1.990e-01
Right phg	1	BESA	2.432e-03	4.209e-01	3.173e-01
Right phg	1	FS3D	2.023e-03	5.184e-01	3.598e-01
Bilateral temporal	2	BESA	2.462e-03	4.139e-01	2.977e-01
Bilateral temporal	2	FS3D	3.512e-03	1.638e-01	8.737e-02
$\mathbf{C}_1$	1	FS3D	2.879e-03	3.145e-01	1.848e-01
$\mathbf{C}_2$	1	FS3D	3.356e-03	2.010e-01	1.428e-01
$\mathbf{C}_3$	1	FS3D	3.570e-03	1.501e-01	1.023e-01

Table 3.1: Conductivity estimation results using equation (3.4). Listed in columns are: (i) the EEG configuration name, (ii) the number of sources for each configuration, (iii) the EEG data simulator used to simulate the data, (iv) the estimated conductivity value σ_1^{est} in S/m, (v) the relative error between σ_1 and σ_1^{est} and (vi) the relative error between g_{km} and g_{km}^{map}.

In this setting, the knowledge of the source term is perfect, as the coefficients $\tilde{\beta}_{0k}$ are computed from the given source location and moment of each configuration. On the other hand, during the expansion of the EEG data using (3.4) a great amount of errors is introduced to the computed $\tilde{g}_k$ coefficients (through the g_{km} coefficients), introducing errors to the input data of the conductivity estimation algorithm. As the EEG data of each configuration were simulated using a given source term, we are able to compute the amount of introduced errors to the g_{km} coefficients. The errors are measured as the l^1 distance between the spherical harmonics coefficients g_{km} and g_{km}^{map}, where g_{km} were determined by equation (3.4) and g_{km}^{map} determined by equation (3.5) which is more precise. The relative EEG error in Table 3.1 is defined as $\frac{\sum |g_{km} - g_{km}^{map}|}{\sum |g_{km}^{map}|}$. The estimated conductivities are

certainly affected by those introduced errors, but still the estimated conductivities are of the same order of magnitude as the actual conductivity value (used in the data simulation).

Estimated source terms

The simulated EEG measurements where processed again, using the FS3D software, estimating the source location $\mathbf{C}_i^{est}$ that best explains the given measurements while also computing the spherical harmonics coefficients g_{km} of the measurements using equation (3.5) and the β_{0km} coefficients of the source term. Note that source estimation is done by using the knowledge that the skull conductivity is $\sigma_1 = 0.0042\,S/m$, whereas through equation (3.5) the same value is used to expand the EEG data.

We perform conductivity estimation from the pair of normalized spherical harmonics coefficients $\tilde{g}_k$ and $\tilde{\beta}_{0k}$, for each source configuration, see Section 3.2. The estimated conductivities for each paradigm is listed in Table 3.2.

Configuration	Src	Model	σ_1^{est}	Rel. Error	Distance
Frontal lobe	1	BESA	4.302e-03	2.431e-02	4.454e-02
Frontal lobe	1	FS3D	4.211e-03	2.677e-03	1.788e-06
Left occipital	1	BESA	4.026e-03	4.141e-02	4.986e-02
Left occipital	1	FS3D	4.052e-03	3.524e-02	2.808e-02
Right phg	1	BESA	4.053e-03	3.485e-02	3.424e-02
Bilateral temporal	2	BESA	4.104e-03	2.280e-02	6.819e-02

Table 3.2: Conductivity estimation results using equation (3.5). Listed in columns are: (i) the EEG source name, (ii) the number of sources for each configuration, (iii) the EEG data simulator used to simulate the data, (iv) the estimated conductivity value σ_1^{est} in S/m, (v) the relative error between σ_1 and σ_1^{est} and (vi) the distance $\sum_i |\mathbf{C}_i^{act} - \mathbf{C}_i^{est}|$.

In this setting, the expansion of the EEG data using (3.5) does not introduce errors to the computed $\tilde{g}_k$ coefficients. In contrast, the knowledge of the source term is not perfect as the sources where estimated (using the reference conductivity $\sigma_1 = 0.0042\,\mathrm{S/m}$), introducing some errors to the input data of the conductivity estimation algorithm. Although, the estimated conductivities seem to be quite accurate, reporting conductivity values close to the actual conductivity value σ_1 used in the data simulations. Note also that the algorithm was able to recover properly the unknown conductivity value even in the case where two sources were used for the data simulation. This suggests that our algorithm is able to handle cases with more than one source present at a time. The influence of the source mislocation will further be studied in the following investigations. Finally,

no big differences are observed between the estimations results with respect to brain locations of the actual sources.

As we have clearly seen, the expansion of the EEG data while computing the $\tilde{g}_k$ spherical harmonic coefficients using equation (3.4) introduce unacceptable errors to the conductivity estimation algorithm. Therefore, in the following investigations and in order to control the introduced uncertainty to the input data for the conductivity estimation, we will only use the method based on equation (3.5) followed by the normalization of equation (3.6). Our choice is less realistic compared to the method based on equation (3.4), but necessary for isolating the influence of each modified parameter on the conductivity estimation procedure.

Robustness with respect to measurement errors

To investigate the stability of our algorithm with respect to measurement errors and the possible influence of the depth of the source, we consider three different source terms each of them made of a single dipole located at: $\mathbf{C}_1$, $\mathbf{C}_2$ and $\mathbf{C}_3$ respectively, all with moment $\mathbf{p}_1$. For each source term, EEG measurements are simulated, whereas the spherical harmonics coefficients of the EEG data $\tilde{g}_k$ and the source term $\tilde{\beta}_{0k}$ are computed. Then, new spherical harmonics coefficients $\tilde{g}_k^i$ have been simulated by adding white Gaussian noise of various levels to the simulated EEG data g_i, with the noise levels been computed as a percent of the standard deviation of the actual EEG measurements (in the spatial scale). Conductivity estimation is performed for the generated pairs of coefficients $\tilde{g}_k^i$ and $\tilde{\beta}_{0k}$. Therefore, the only uncertainty introduced to the input pair of coefficients, namely the $\tilde{g}_k^i$, arise from the measurement errors, while the source term (used in data simulation) was perfectly known. The estimated conductivities over the introduced noise levels and the corresponding distance between the actual and the noisy measurement coefficients are presented in Figure 3.2.

The results show that our conductivity estimation algorithm is robust with respect to the added noise, as the estimated conductivities are quite close to the actual σ_1 conductivity value (used in the simulations) up to 30% of added noise, and all the estimated conductivities being in the scale of 10^{-3} far from the actual one. This comes in agreement with the inequality in Proposition 1 stating that the distance between the actual and the estimated conductivity is bounded by the distance between the measurements up to a multiplicative constant (since the distance between the potentials u_s and u'_s associated to the source terms is assumed to be zero in this case). Observe that conductivity estimation seems to be less affected by the added noise for sources deeper in Ω_0, as the values of the relative errors decrease when the source is moving from $\mathbf{C}_1$ to $\mathbf{C}_3$.

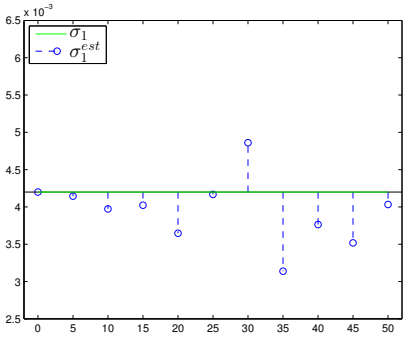

(a) Dipole located at $\mathbf{C}_1$

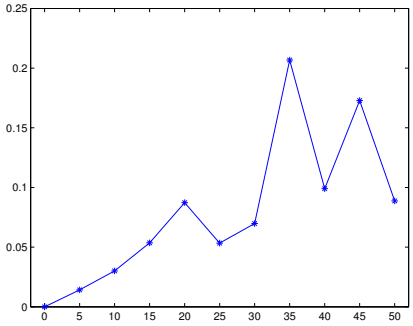

(b) Dipole located at $\mathbf{C}_1$

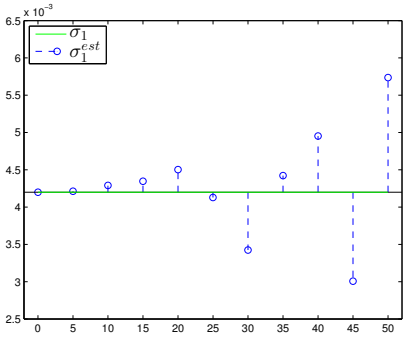

(c) Dipole located at $\mathbf{C}_2$

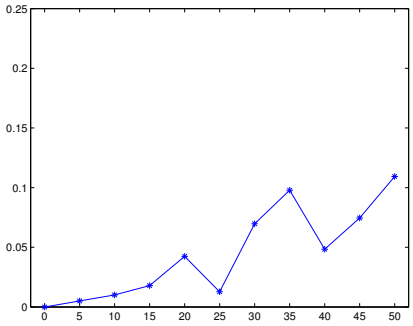

(d) Dipole located at $\mathbf{C}_2$

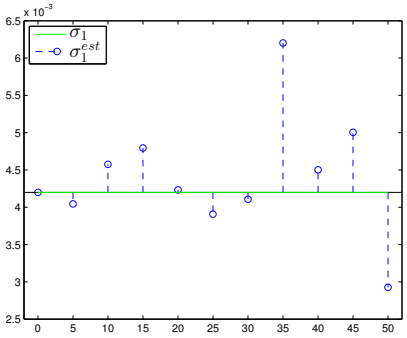

(e) Dipole located at $\mathbf{C}_3$

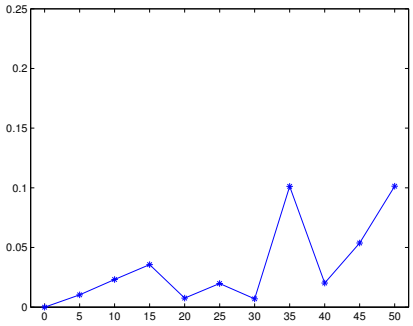

(f) Dipole located at $\mathbf{C}_3$

Figure 3.2: Conductivity estimation results with respect to the added level of noise (in percentage) on the simulated EEG measurements. [Left] Estimated conductivity values (S/m) over the increasing percent of noise. Displayed are: σ_1, the actual conductivity value used in the EEG data simulation, and σ_{est}, the estimated conductivity value for each level of added noise. [Right] The distance $\sum_k |\tilde{g}_k - \tilde{g}_k^i|$ between the spherical harmonics coefficients of the simulated and the noisy EEG data.

Behaviour with respect to errors on the source term

Influence of mislocated sources at a constant distance

The original source location $\mathbf{C}_i$ for $i = 1, \cdots, 3$ is replaced by inexact locations $\mathbf{C}_i^n$ for $n = 1, \cdots, 20$ located at a constant distance from $\mathbf{C}_i$ (a percentage of the inner sphere radius r_0), as illustrated in Figure 3.3, while the source moment $\mathbf{p}_1$ is retained. For each new dipole location $\mathbf{C}_i^n$, the associated spherical harmonics coefficients $\tilde{\beta}_{0k}^n$ are simulated. We perform conductivity estimation from the pairs $\tilde{g}_k$, $\tilde{\beta}_{0k}^n$ (recall that $\tilde{g}_k$ correspond to the actual $\tilde{\beta}_{0k}$). Therefore, the only uncertainty introduced to the input pair of coefficients, namely the $\tilde{\beta}_{0k}^n$, comes from the inexact location of the source term, while keeping the EEG measurements and the original source moment intact. The conductivity estimation results and the resulting relative errors while the distance $|\mathbf{C}_i - \mathbf{C}_i^n|$ increases are illustrated in Figure 3.4.

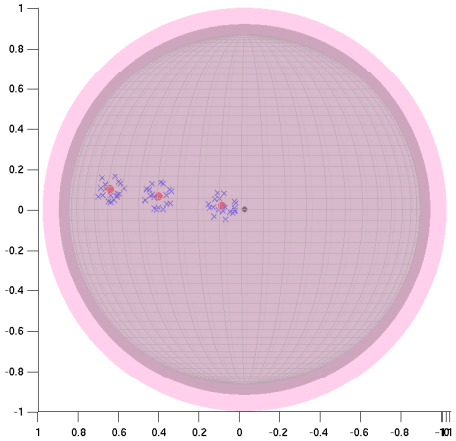

Figure 3.3: Locations (in Ω_0) of $\mathbf{C}_i$ (red bullets) and of the 20 points $\mathbf{C}_i^n$ (blue cross) surrounding each $\mathbf{C}_i$, for $|\mathbf{C}_i - \mathbf{C}_i^n|$ equal to 10% of r_0 with $i = 1, 2, 3$.

Observe that in the plots 3.4(e) and 3.4(f), the mislocation distance (on the abcissa axis) do not reach the same values as in the other plots of Figure 3.4. This happens because in our simulations the mislocation distance from a location $\mathbf{C}_i$ was not allowed to reach the center of Ω_0 (the point O at origin), as discussed in Section 2.6. Therefore, we have chosen mislocation distances up to 12% of r_0 which do not reach the origin. The obtained conductivity estimation results show that our algorithm is stable with respect to the source mislocations, while the distance between the actual source location and its mislocations increases. As stated by the inequality in Remark 1 the distance between the actual and the estimated conductivity is

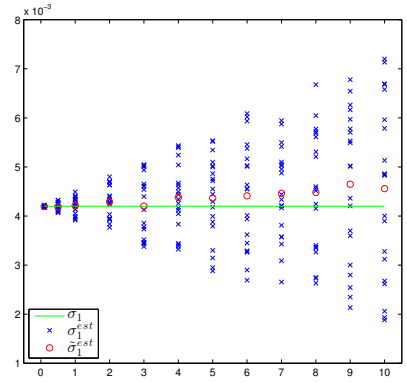

(a) Mislocations of $\mathbf{C}_1$

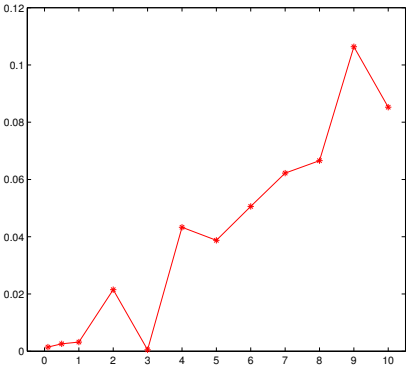

(b) Mislocations of $\mathbf{C}_1$

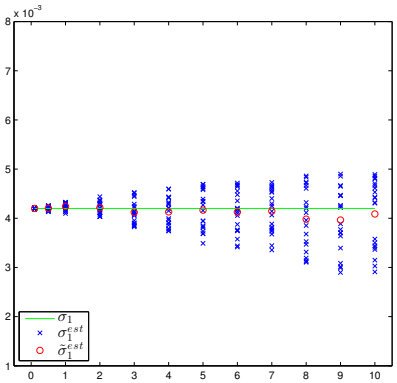

(c) Mislocations of $\mathbf{C}_2$

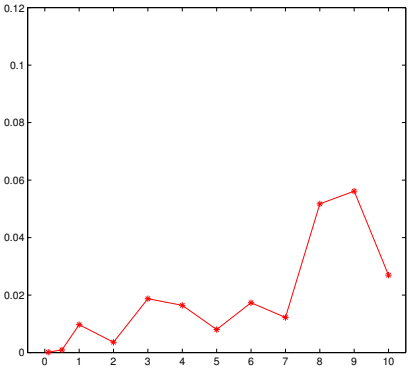

(d) Mislocations of $\mathbf{C}_2$

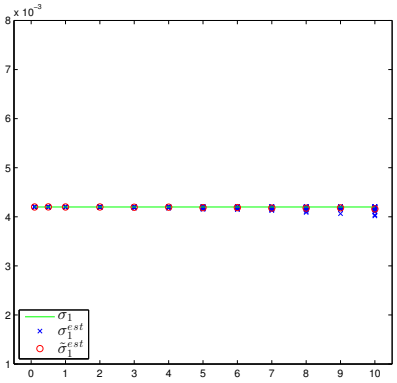

(e) Mislocations of $\mathbf{C}_3$

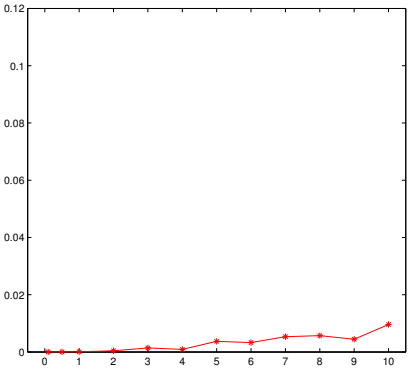

(f) Mislocations of $\mathbf{C}_3$

Figure 3.4: Conductivity estimation results, with respect to increasing mislocation distances (in percent of the brain radius) from the actual dipole. [Left] 20 estimated conductivity values (S/m) for each percentage values of increasing distance. Displayed are: σ_1, the actual conductivity value used in the EEG data simulation, σ_1^{est}, the estimated conductivity value for each dipole position $\mathbf{C}_i^n$, and $\tilde{\sigma}_1^{est}$, the mean value of σ_1^{est} among $n = 1, \cdots, 20$. [Right] The relative error between the mean values $\tilde{\sigma}_1^{est}$ and σ_1.

bounded by the distance between the source terms up to a multiplicative constant (since the distance between the functions g and g' is zero in this case). Observe that for a source mislocation up to 6% of r_0 the estimated conductivities are not that far from the actual one, and all the estimated conductivities being in the scale of 10^{-3} far from the actual one. This means that having a wrong source localization in an EEG experiment of no more than $0,8\,\text{cm}$ (using the realistic brain radius mentioned at the beginning of Section 3.3) the estimated conductivity would still not be that far.

Finally, it is visually evident that the deeper sources (as the one located at $\mathbf{C}_2$ and $\mathbf{C}_3$) are less and less affected by the source mislocation, with the estimated conductivities closer to the actual one. This is maybe due to the increasing distance between the source location $\mathbf{C}_i$ and the sensors on S_2.

Influence of radial source mislocations

The original location $\mathbf{C}_i$ for $i = 1, \cdots, 3$ is replaced by inexact locations $\mathbf{C}_i^n$ for $n = 1, \cdots, N$ located at a constant distance from $\mathbf{C}_i$ and on the radius l passing from $\mathbf{C}_1$. The mislocation distance was chosen to be 10% of r_0, leading to $N = 20$ mislocated sources. The source moment $\mathbf{p}_1$ is retained for all mislocated sources. For each new inexact dipole location $\mathbf{C}_i^n$, the associated spherical harmonics coefficients $\tilde{\beta}_{0k}^n$ are simulated. We perform conductivity estimation from the pairs $\tilde{g}_k$, $\tilde{\beta}_{0k}^n$ (recall that $\tilde{g}_k$ correspond to the actual $\tilde{\beta}_{0k}$). Therefore, the only uncertainty introduced to the input pair of coefficients, namely the $\tilde{\beta}_{0k}^n$, come from the inexact location of the source term, while keeping the EEG measurements and the original source moment intact. This is similar to the investigation of the previous paragraph but with the sources mislocated on the radial direction. For simplicity, the locations of the inexact sources $\mathbf{C}_i^n$ are presented as the distance from the origin.

The conductivity estimation results and the resulting relative errors are illustrated in Figure 3.5 as a function of the distance between the inexact source location and the origin. The conductivity estimation results show that our algorithm is again stable with respect to this type of source mislocations as the mislocation distance increases, at least up to a reasonable distance from the actual source, and in agreement with the inequality in Remark 1. Observe also that the conductivity estimation problem seems more stable when the sources are closer to the origin (located at $\mathbf{C}_2$ and $\mathbf{C}_3$), as more estimated conductivities are close to the true conductivity line compared to the one obtained when the actual source was located at $\mathbf{C}_1$.

Observe that the closer an inexact location is to the actual one, the better the accuracy of the conductivity estimation is.

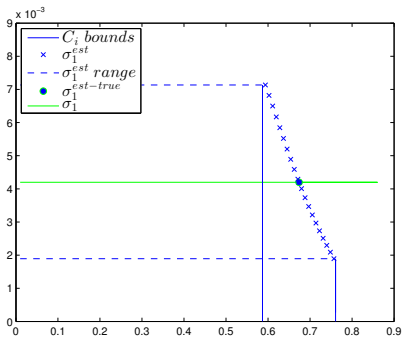

(a) Mislocations of $\mathbf{C}_1$

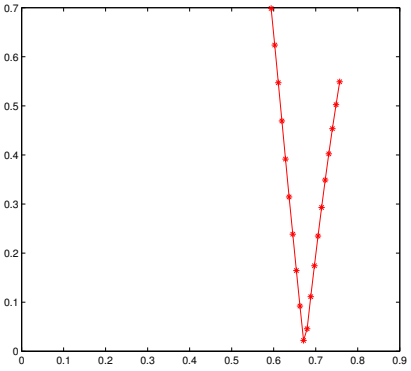

(b) Mislocations of $\mathbf{C}_1$

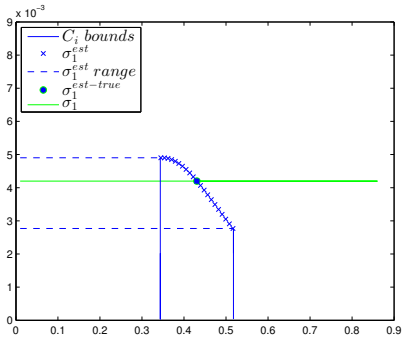

(c) Mislocations of $\mathbf{C}_2$

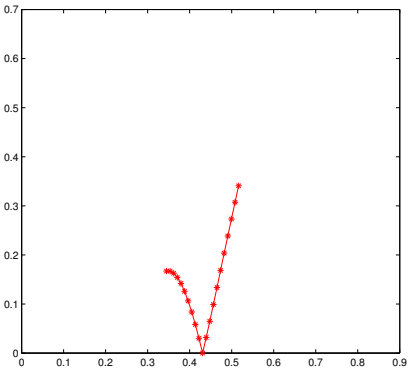

(d) Mislocations of $\mathbf{C}_2$

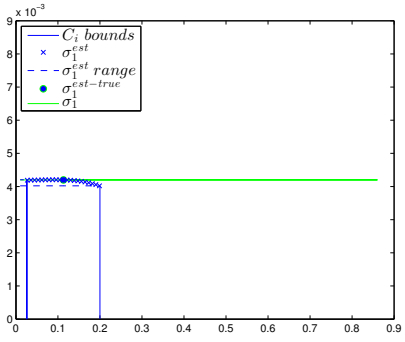

(e) Mislocations of $\mathbf{C}_3$

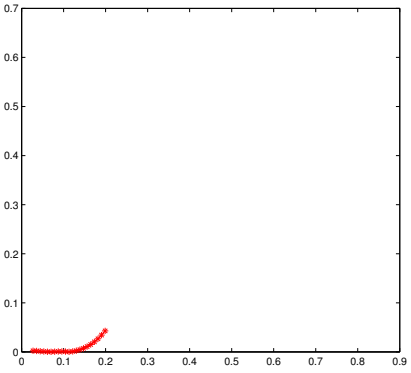

(f) Mislocations of $\mathbf{C}_3$

Figure 3.5: Conductivity estimation results for bounded mislocations of the actual dipole in the radial direction. The results are presented with respect to the distance of the mislocated source from the origin. [Left] Estimated conductivity values (S/m) for the mislocated dipoles $\mathbf{C}_i$. Displayed are: $\mathbf{C}_i$ *bounds*, the mislocation bounds set at 10% of the brain radius, σ_1^{est}, the estimated conductivity value within the mislocation bounds, σ_1^{est} *range*, the corresponding range of estimated conductivities, $\sigma_1^{est-true}$, the estimated conductivity value for the actual dipole $\mathbf{C}_i$, and σ_1, the actual conductivity value used in the EEG data simulation. [Right] Relative errors between σ_1^{est} and σ_1.

Sensitivity to the radial source position from S_0

As discussed in Section 2.7 the stability of the inverse conductivity estimation problem depends on the distance of the sources from the interface S_0. To better illustrate this stability property, we extend the previous investigation by exploring more "radial" locations (not only at the locations $\mathbf{C}_1$, $\mathbf{C}_2$ and $\mathbf{C}_3$) for the simulated sources.

Therefore, we perform an investigation where we consider 100 source locations evenly distributed on the radius l passing from $\mathbf{C}_1$, to simulate the spherical harmonics coefficients $\tilde{g}_k$ and $\tilde{\beta}_{0k}$. We take care to ensure that among them the closest dipole to the center and the surface of the Ω_0 ball has at least a minimum distance of 0.01, while the source moment $\mathbf{p}_1$ is retained.

Each simulated source, $\mathbf{D}_i$ for $i = 1, \cdots, 100$, is replaced by inexact locations $\mathbf{D}_i^n$ for $n = 1, \cdots, N < 100$, belonging to a subset of $\{\mathbf{D}_i\}$, simulating the inexact spherical harmonics coefficients $\tilde{\beta}_{0k}^n$. The number N of the inexact locations (for each simulated source), is determined by the following two quantities: the maximum distance between two estimated conductivities $\left|\sigma_1^{est} - \sigma_1^{est'}\right|$ when the inexact locations are bounded to be 10% of r_0 far from the simulated source location $\mathbf{D}_i$ (i.e. $|\mathbf{D}_i - \mathbf{D}_i^n| \leq 0.1 r_0$) as illustrated in Plot 3.6(b) and second, the maximum distance between two inexact locations $|\mathbf{D}_i^n - \mathbf{D}_i^{n'}|$ when the estimated conductivities of the inexact location are bounded to be 10% far from the estimated conductivity of the simulated source (i.e. $\left|\sigma_1^{est} - \sigma_1^{est-true}\right| \leq 0.1$) as illustrated in Plot 3.6(a). Both quantities are expressed as a function of the simulated source location, presented as the distance from the origin. An example showing the bounds and the conductivity estimation results participating to the computations of the above two quantities for a simulated source placed at $\mathbf{C}_1$ is presented in Figure 3.6. The results of the investigation for all the simulated sources and their inexact locations are presented in Figure 3.7.

The results are in agreement with the previous investigations and the stability property in Section 2.7, showing that the deeper a source is (i.e. far from the S_0 surface), the more stable the conductivity estimation problem is. This can be easily observed in Plot 3.7(a) where the distance between the estimated conductivities increases (becoming less stable) while the simulated source is moving towards the surface S_0, even though the mislocation distance (i.e. selected bound) was fixed. In Plot 3.7(b) the same phenomenon is observed up to the value of 0.3 in the abcissa axis.

At values higher than 0.75 in Plot 3.7(a) a decay of the computed distance is observed. This happens for two reasons, first the conductivity estimation problem becomes less stable and the estimated conductivities of neighbouring mislocated sources have bigger difference between them, and second because the actual source comes too close to S_0 leaving less and less space for inexact locations. For both reasons, less and less data contribute to

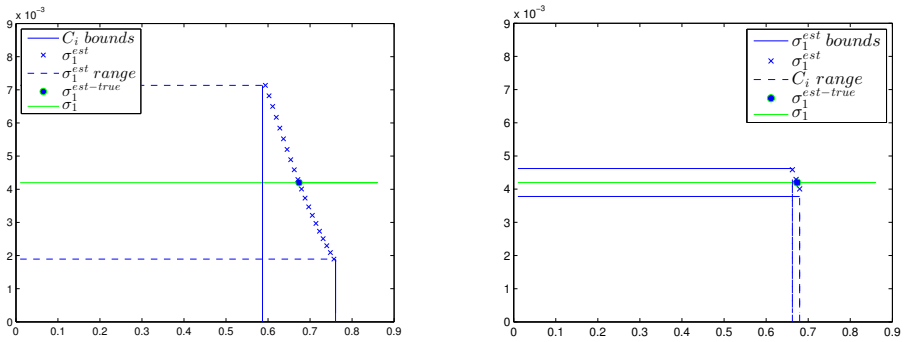

(a) Bounded mislocations of $\mathbf{C}_1$ (b) Bounded estimated conductivities of $\mathbf{C}_1$

Figure 3.6: Conductivity estimation results for bounded mislocations of a simulated dipole (placed at $\mathbf{C}_1$) in the radial direction. [Left] Conductivity estimation results (S/m) for bounded dipole mislocations within $|\mathbf{C}_1 - \mathbf{C}_1^n| \leq 0.1r_0$. Displayed are: "$\mathbf{C}_i$ *bounds*", the mislocation bounds set at 10% of the brain radius, and σ_1^{est} *range*, the corresponding range of estimated conductivities. [Right] Bounded conductivity estimation results (S/m) within $\left|\sigma_1^{est} - \sigma_1^{est-true}\right| \leq 0.1\sigma_1^{est-true}$. Displayed are: σ_1^{est} *bounds*, the conductivity estimation bounds set at 10% of the estimated conductivity for the simulated source $\mathbf{C}_1$, "$\mathbf{C}_i$ *range*", the corresponding range of mislocation. Displayed in both are: σ_1, the actual conductivity value used in the EEG data simulation, and σ_1^{est}, the estimated conductivities within the given bounds.

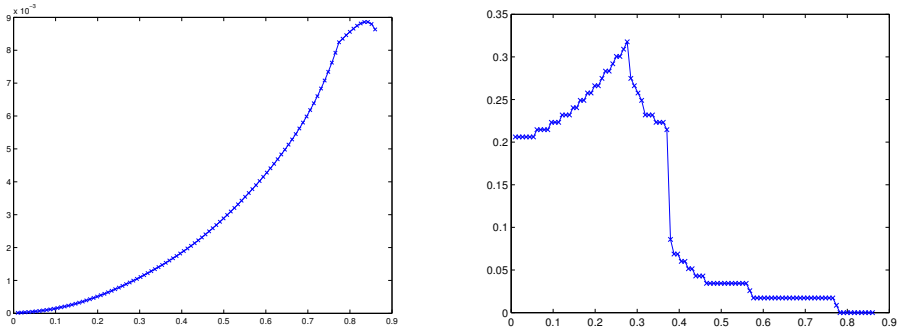

(a) Distance between estimated conductivities (b) Distance between mislocated sources

Figure 3.7: Bounded conductivity estimation results with respect to the simulated source locations. The results are presented with respect to the distance of the simulated sources from the origin (abcissa axis). [Left] The maximum distance between two estimated conductivities $\left|\sigma_1^{est} - \sigma_1^{est'}\right|$ when the inexact locations are bounded to be 10% of r_0 far from the simulated source location $\mathbf{D}_i$. [Right] The maximum distance between two inexact locations $|\mathbf{D}_i^n - \mathbf{D}_i^{n'}|$ when the estimated conductivities of the inexact locations are bounded to be 10% far from the estimated conductivity of the simulated source.

the computations. The same effects can be observed in Plot 3.7(b) starting after 0.35 for the first reason and before 0.8 for both.

Influence of the moment

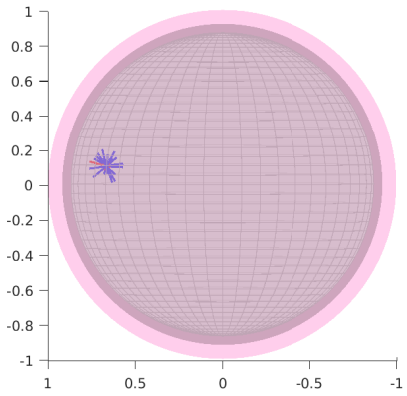

Figure 3.8: Dipolar source at $\mathbf{C}_1$ (red point) with its original moment $\mathbf{p}_1$ (red vector) and its 20 inexact orientations $\mathbf{p}_1^n$ (blue vectors) having an amplitude equal to the original: $|\mathbf{p}_1| = |\mathbf{p}_1^n| = 1$.

The influence of inexact value of the moment on the conductivity estimation is investigated at the three dipole locations $\mathbf{C}_1$, $\mathbf{C}_2$, and $\mathbf{C}_3$. The original source orientation is replaced by 20 inexact orientations $\mathbf{p}_1^n$ of a given amplitude (strength), as illustrated in Figure 3.9. We consider various strengths with values in $[0.9, 1.1]$ of the amplitude $|\mathbf{p}_1| = 1$ of the original dipole. For each new source amplitude the spherical harmonics coefficients $\tilde{\beta}_{0k}^n$ of the inexact orientation $\mathbf{p}_1^n$ are simulated. We perform conductivity estimation from the pairs $\tilde{g}_k$, $\tilde{\beta}_{0k}^n$ (recall that $\tilde{g}_k$ correspond to the actual $\tilde{\beta}_{0k}$). Therefore, the uncertainty only acts on the coefficients $\tilde{\beta}_{0k}^n$ and comes from the inexact orientation, when the amplitude is set to 1 (the original source amplitude) and both the orientation and the amplitude for the other amplitude values. The EEG measurements and the original source location are intact. The conductivity estimation results and the mean of the resulted relative errors are illustrated in Figure 3.9 as a function of the source strength.

The conductivity estimation results show that our algorithm seems to be most affected by the moment amplitude, with the estimated conductivities varying in the scale of 10^{-2}.

Finally observe, that deeper sources seems to be less affected by the moment amplitude, with the mean relative error decreasing when the source location is moving from $\mathbf{C}_1$ to $\mathbf{C}_2$ and $\mathbf{C}_3$.

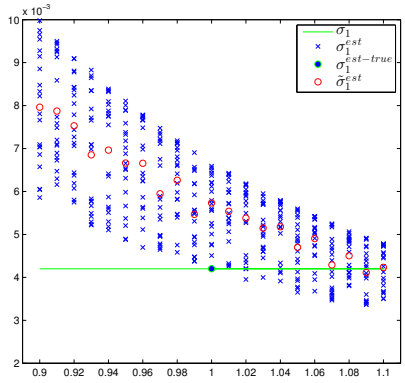

(a) Variations of $|\mathbf{p}_1|$ at $\mathbf{C}_1$

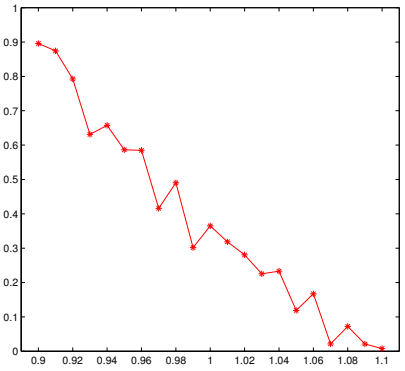

(b) Variations of $|\mathbf{p}_1|$ at $\mathbf{C}_1$

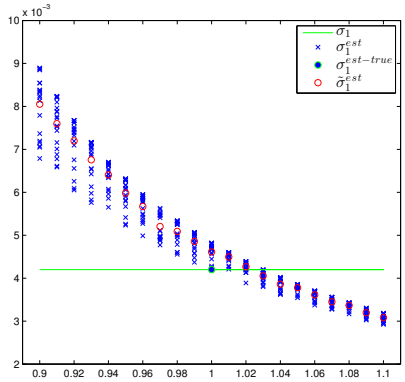

(c) Variations of $|\mathbf{p}_1|$ at $\mathbf{C}_2$

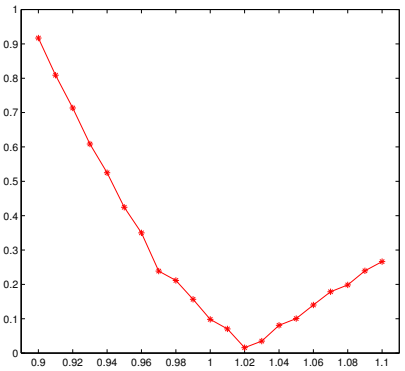

(d) Variations of $|\mathbf{p}_1|$ at $\mathbf{C}_2$

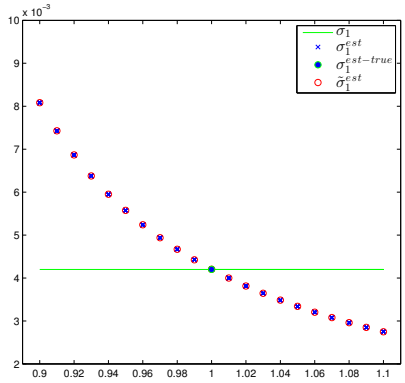

(e) Variations of $|\mathbf{p}_1|$ at $\mathbf{C}_3$

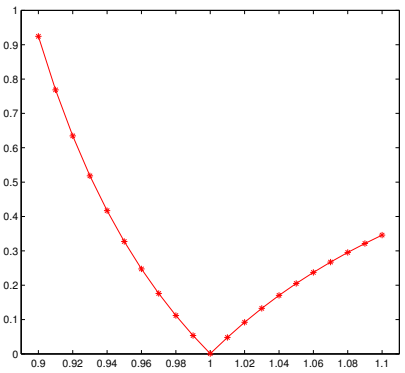

(f) Variations of $|\mathbf{p}_1|$ at $\mathbf{C}_3$

Figure 3.9: Conductivity estimation results with respect to increasing inexact moment amplitude values (relative to the actual source moment $|\mathbf{p}_1| = 1$). [Left] Conductivity estimation results (S/m) for 20 inexact orientations for each inexact moment amplitude value. Displayed are: σ_1, the actual conductivity value used in the EEG data simulation, σ_1^{est}, the estimated conductivities for each new source moment (orientation and amplitude), $\sigma_1^{est-true}$, the estimated conductivity value for the actual dipole $(\mathbf{C}_i)$, and $\tilde{\sigma}_1^{est}$, the mean value of σ_1^{est} among $n = 1, \cdots, 20$. [Right] The relative error between the mean values $\tilde{\sigma}_1^{est}$ and σ_1.

Discussion and conclusion

Following Chapter 2, observe that our uniqueness result, Theorem 1, may be expressed as an identifiability property of the conductivity value (model parameter) σ_1 in the relation (2.16) from boundary data to sources (transfer function, control to observation), [21, 66]. This could be useful in order to couple EEG with additional modalities, like EIT (where $\partial_n u \neq 0$ is known on Γ) or even MEG (magnetoencephalography, which measures the magnetic field outside the head), and to simultaneously estimate both σ_1 and the source term $\mathcal{S}$ in situations where the latter is (partially) unknown. The source locations, for example, can be fixed in somatosensory evoked potentials (SEP) and fields (SEF) measurements by the SEF localisations, which are mainly independent of skull conductivity, see [15, 110].

In EIT, the source term is zero ($\mathcal{S} = 0$), as it is assumed that the only electrical activity present is the injected current at the selected pair of EEG electrodes. Therefore, the current flux $\phi = \sigma \partial_n u$ is taken as an input (control) at the selected pair of electrodes, while the associated potential values (3.1) are measured at the other electrode locations ($\mathbf{r} \neq \mathbf{r}_{in}\,, \mathbf{r}_{out}$). This is summarized by:

$$\begin{cases} \nabla \cdot (\sigma \nabla u) = 0 \text{ in } \Omega\,, \\ \sigma \nabla u \cdot n = \delta_{\mathbf{r}_{in}} - \delta_{\mathbf{r}_{out}} \text{ in } \partial\Omega\,, \end{cases}$$

where $\mathbf{r}_{in}$ is the input electrode where the current was injected, $\mathbf{r}_{out}$ the output electrode, and δ_r the Dirac mass at location $\mathbf{r}$.

Situations with more than 3 spherical layers could be described similarly, which may help to consider more general conductivities (smooth but non constant) by piecewise constant discretization. The addition of a new spherical layer would practically require to incorporate a few more matrices describing its transmission conditions in the relation in Section 2.5.1. This would be a step towards non homogeneous layers. Anisotropic models could be considered as well, in relations with more realistic geometries.

Also, one may also recover using the above scheme possibly unknown information about the (spherical) geometry of Ω_1 (like r_1 or/and r_0).

In Chapter 3, the presented results illustrate the influence of errors on conductivity estimation, and the robust character of our algorithm, in accor-

dance with the stability result of Proposition 1. The proposed conductivity estimation algorithm proved to be robust both to measurement errors and to various source mislocations, while the estimations appear to be more stable at deep source locations. In contrast, the algorithm seems to be less robust with respect to the moment amplitude but the obtained estimations are again more stable at deep source locations.

Observe that the obtained results in Table 3.2 and Figures 3.2, 3.4, and 3.5 are quite accurate (within the scale of 10^{-3}) for a small and acceptable amount of introduced errors. For example, for an inverse source localization algorithm, an acceptable localization error would be within the scale of a few millimetres, while localizations of a few centimetres would be inappropriate for clinical and functional use. Assuming the realistic brain radius of 8 cm as in [90] a mislocation of 10% of the brain radius translates to 0.8 cm localization error in the human brain. Therefore, the estimations obtained with our algorithm and shown in Figures 3.4 and 3.5 beyond this (mislocation) value are less and less met in practice.

The bounds introduced in Figure 3.6, aim in particular at illustrating the robustness of our algorithm with respect to a fixed range of variation around the actual data, discarding estimations that are too far. In addition, the obtained results are in accordance with the discussion in Section 2.7, where it has been mentioned that if the sources are located far enough from S_0 in the sense that $\max(|\mathbf{C}_q|, |\mathbf{C}'_q|) \leq \rho < r_0$, the conductivity σ_1 depends on the boundary data g and on the source term $\mathcal{S}$. The results shown in Figures 3.2, 3.4, and 3.5 also illustrate the difference of stability with respect to the source distance from S_0. Computing the value of ρ and determining whether the computed values come in agreement with the numerical results would be interesting for a future investigation.

The results in Figure 3.9 indicate that the conductivity estimation algorithm is not very robust with respect to the moment amplitude and should be investigated further. Following the discussion of the last paragraph of Section 4.3.4, we could also perform the dual investigation and, for each fixed orientation of the moment, vary its amplitude.

In order to penalize high frequencies and to get more accurate estimations, one might introduce in the minimization criterion (3.8) appropriate multiplicative weights (decreasing with the spherical harmonic index k). Penalization of the high frequencies trough weighting can also be applied at equation (3.4). Also, concerning the computation of the coefficients from the pointwise values at electrodes, another possibility would be to solve the following minimization problem:

$$\min_{[g_{km}]} \|M[g_{km}] - [g_i]\|^2 + \lambda \sum_{k,m} k(k+1)|g_{km}|^2 \,,$$

where $\lambda > 0$ is a regularization coefficient. Note that one could also replace

the normalization (3.6) by:

$$\begin{cases} \tilde{g}_k = \sum\limits_{|m|\leq k} |g_{km}|^2 \,, \\ \tilde{\beta}_{0k} = \sum\limits_{|m|\leq k} \beta_{0km}\, \bar{g}_{km} \,, \end{cases}$$

where $\bar{g}_{km}$ is the complex conjugate number to g_{km}.

To improve both the EEG data expansion and the conductivity estimation, one might consider using another degree K for the spherical harmonic basis. Theoretically, the value of K should be chosen such that it satisfy the inequality $N_e \leq (K+1)^2$, in order to have an equal or higher number of know terms compared to unknowns. This implies that in our setting ($N_e = 64$), the degree for the spherical harmonic basis could be set to $K = 7$, which is the minimal value. However the appropriate value of K might be higher depending on the activity of a source activity and its frequency.

We observed in Section 3.3.3, Figure 3.4, that the mean estimated conductivity value was quite close to the actual σ_1 value used for the EEG data simulation. This suggest to use an iterative procedure that alternates between conductivity estimation and source localization steps.

More general models in terms of PDE could be interesting namely those provided by Helmholtz equation, see for example [12]. They furnish more precise models than Laplace-Poisson equation when the quasi-static assumption is no longer valid.

PART II

Conductivity estimation in a realistic geometry

CHAPTER 4

Importance of skull inhomogeneity

In the previous chapters we have studied the inverse conductivity estimation problem deriving analytical formulas for a spherical head geometry where the skull was modelled as a single and homogeneous layer. Derivation of analytical formulas while considering an inhomogeneous skull would assume that the skull is made of concentric spheres, which is too simplistic. Thus to analyse the importance of skull inhomogeneity we will consider realistic head models.

In this chapter, we question the validity of the human skull inhomogeneity for conductivity estimation in EEG, performing a simulation study that compares two realistic head models: the first modelling the skull as a single and homogeneous layer, the second modelling its inhomogeneity by accounting for two different types of skull tissues.

Simultaneous conductivity estimation and source localization is performed on the compared models using a number of single dipole simulated EEG data. Other aspects under consideration are the selection of the proper skull tissue and the influence of different skull templates on conductivity estimation.

Introduction to skull inhomogeneity

One of the major issues related to EEG is to localize where in the brain signals are generated. This is the so called inverse problem in electroencephalography (EEG) [72] and aims at finding the source distribution that best explains the electric potentials measured by a set of electrodes at the surface of the scalp. The quality of the inverse solution depends on the mathematical algorithm chosen [47], as well as the accuracy of the volume conductor, i.e. the head model, reflecting the geometry and the conductivity values of the different head tissues.

The human head consists of several tissues, some of the most commonly

found in head models being: the scalp, the skull, the cerebrospinal fluid (CSF), and the brain which is often segmented into gray and white matter. Among the head tissues, the skull is the one that influences most the accuracy of EEG source localization methods because of its low conductivity [100].

Although spherical head models can be used to solve the inverse source localization problem, when localization accuracy is the main priority, realistically shaped head models are used instead [27]. The realistically shaped head models, capture the head tissues in greater detail, as the tissues are often extracted from imaging modalities such as MRI and CT scans. Usually when such data are available, for the subject of interest, an individual head model can be constructed segmenting the different tissues for the available data. Conversely, when individual data are not available, a realistic approximation can be used, usually constructed by registering data of different individuals into the same space and then averaging them to produce an average realistic head model. Due to the imperfect anatomical correspondence among the individuals, the created head model might cause errors in the source localization as discussed in [99].

The human skull is a bony tissue consisting of compact (compacta) and spongy (spongiosa) bone layers, whose thickness vary across the skull. While compacta is present almost everywhere across the skull, spongiosa may not be always present. However, most often the skull is modelled as single bulk compartment, without taking into account the internal skull structure as it is not always visible in the available MRI data.

The conductivity value of the spongiosa compared to compacta may differ substantially, by a factor of 4.5 within an individual [3,28]. Depending on the relative thickness of the spongiosa, an approximate relationship between the bulk skull conductivity and the compacta and spongiosa conductivities can be formulated [28]. As the relative thickness of the spongiosa varies across the skull it has to be expected that the bulk skull conductivity also varies. Indeed, this is the case of measured conductivity values using skull samples of various proportions of spongiosa within the sample [95]. However, the skull is often modelled as a single bulk compartment with a single homogeneous conductivity value.

Solving the inverse problem of source reconstruction using uncertain head geometries [28, 65, 86] or conductivity values [2, 84] may lead to important localization errors.

As the skull tissue composition has strong inter-individual variability both in terms of tissue geometry and of individual tissue conductivity, conductivity estimation techniques are required [68] in order to determine the unknown skull tissue conductivity.

Conductivity estimation can be performed on data from an event-related stimulation paradigm, which can be explained by one dipole source [102]. Somatosensory Evoked Potentials (SEP) is one of the many event-related

stimulation paradigms [68] which has been suggested for conductivity estimation. SEP are obtained in response to a sensory stimulus, such as an electrical stimulation of the skin over the trajectory of the median nerve within an arm. The location of the response activity arises within the somatosensory cortex and while being quite focal can be explained by one dipole source.

A conductivity value for the skull can be estimated as the value for which the single dipole source provides the best goodness of fit to the EEG data. This conductivity value could then be used to analyse the actual data of interest whose activity is likely to lie outside the somatosensory cortex.

Furthermore, it is known that the EEG forward solution, i.e. given a source distribution what is the generated electrical potentials at a set of electrodes placed at the surface of the skull, is most affected by the conductivities of all tissues between the source and the sensors [44,65]. For conductivity estimation based on data from an event-related stimulation paradigm this means that the estimated skull conductivity might reflect only the local skull conductivity. The estimated conductivity value based on a different paradigm located in another brain region might differ substantially.

This raises the following research question: Is conductivity estimation based on data from an event-related stimulation paradigm meaningful without accounting for the internal skull structure, especially when the activity of interest may lie outside the area where the activity of the stimulation paradigm was located?

We perform a simulation study comparing two realistic head models constructed from individual MRI data, in order to determine the importance of the internal skull structure for conductivity estimation in EEG: a detailed model accounting for the compact and spongy bone layers and a bulk model where the skull is simplified to a single compartment. Using the detailed model as a reference, reference EEG data is generated for 20 single dipole sources placed at different brain areas. Conductivity estimation is performed in both models for all 20 single dipole sources using a simple exhaustive search approach, estimating the bulk skull conductivity in the bulk model and the compact bone conductivity in the detailed model, while the rest of the conductivity values are considered identical to the ones used in the reference data generation.

Materials and methods

Detailed head model generation

Acquired data

Magnetic resonance images (MRI) of three epileptic male subjects (30, 32 and 20 years-old) were acquired with a T1-weighted sequence. The voxel

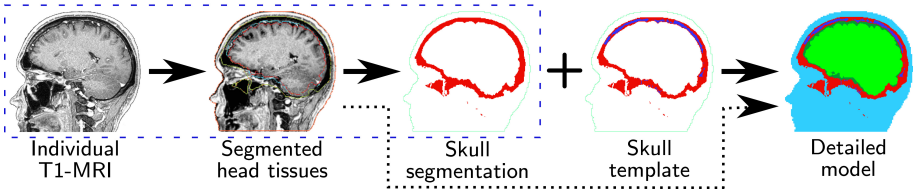

Figure 4.1: Detailed model generation work-flow: The individual's MRI is segmented distinguishing the scalp, skull, CSF and brain tissues. A spongiosa model is extracted from a template and included in the individual's skull segmentation, leading to a 5-layer realistic head model.

scan resolution was $1 \times 1 \times 1\,\text{mm}$. The data acquisition protocol was in accordance with the French rules for public health (article L 1121-1) and the Helsinki Declaration.

Segmentation and spongiosa model extraction

Our three detailed models (one for each patient) are based on the segmentation of the individual T1 MRI data using the automated procedure of BESA MRI 2.0 (BESA GmbH, Gräfelfing, Germany). We distinguished between the following tissue types: scalp, skull, CSF, and brain. Due to the low contrast and high noise of the available MRI the accurate segmentation of the internal skull structure (spongiosa compartment) was not possible. Instead, a template of the spongiosa compartment was extracted and aligned with the individual's skull segmentation. The spongiosa template was extracted from the labeled "Colin 27 Average Brain" [52].

Spongiosa model registration

In order to later include the spongiosa model to our individual's segmentation, we performed first an affine and then a non-linear registration of the skull template to the individual skull segmentation. Here, our main concern is the best possible alignment of the skull template, thus also the spongiosa compartment, with our individual skull segmentation. For the affine registration the FLIRT [55] tool implemented in the FSL toolbox was used. The non-linear registration was based on an extension [93] of the Diffeomorphics Deamons algorithm [104] implementation in MedInria 1.x [96] using a cost-function suitable for registration of labeled images. The nearest neighbour interpolation option was used to preserve meaningful labels in the transformed images.

Post-processing of the registered spongiosa model

The transformed spongiosa model was then post-processed using morphological operations.A morphological closing by 2 mm was applied to the spongiosa model to smoothen the distribution. Furthermore, the spongiosa model was masked with a by 1 mm eroded skull to guarantee the minimum thickness of the inner and outer compact bone layers. The morphological operations used, were implemented in MATLAB and Image Processing Toolbox Release 2012b (The MathWorks, Inc., Natick, Massachusetts, United States).

Volume conductor generation

All skull voxels of the individual segmentation that were marked in the transformed and post-processed spongiosa mask were relabeled as spongiosa. A 1 mm geometry-adapted hexahedral finite element mesh (FEM) [107] was then created in BESA MRI 2.0 (BESA GmbH, Gräfelfing, Germany) from the individual's segmentation with the included spongiosa model. The resulting 5-layer head model finally accounts for the following tissue types: scalp, skull's compacta and spongiosa, CSF, and brain. The same procedure was repeated for each patient using his MRI data to build a new detailed model. The detailed model generation work-flow is summarized in Figure 4.1.

Simulation setup

Reference data generation

Reference data was generated for 20 dipoles at 10 different locations spread over both brain hemispheres with radial and tangential orientations. The brain areas of our subjects were identified based on visual comparison with the Talairach Atlas. The source locations were manually selected to represent the following brain areas: frontal lobe, somatosensory cortex, auditory cortex, temporal lobe, and occipital cortex. Reference EEG data was simulated at 64 electrode locations for each source, in each detailed FEM model, with the sources not lying on the nodes of the FEM grid. The data simulation was performed in BESA Research 6.0 (BESA GmbH, Gräfelfing, Germany).

For the reference data generation the following commonly used isotropic conductivity values [28] were assigned to each element of the detailed model depending on the tissue: scalp 0.43 S/m, compacta 0.0064 S/m, spongiosa 0.0287 S/m, cerebral spinal fluid (CSF) 1.79 S/m, and brain 0.33 S/m. The reference data generation for a single dipole is illustrated in Figure 4.2.

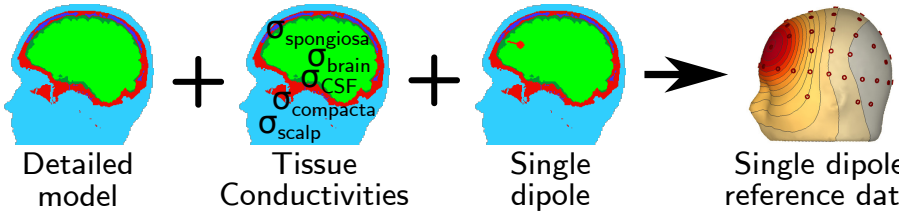

Figure 4.2: Reference data simulation for a single dipole: EEG measurements of a single time instant are generated placing a source in the reference volume conductor model of known tissue conductivities. The procedure was repeated for all 20 dipoles (10 locations with radial and tangential orientation).

Test models

Two test models are considered to perform conductivity estimation selecting 12 isotropic conductivity values to evaluate the tissue in question within each model, while the rest of the conductivity values are considered identical to the ones used in the reference data generation. We have taken care to use the same relative conductivity range from 42% to 250% of a reference tissue conductivity value for both models.

- The **detailed model** that specifically accounts for the internal skull structure (i.e. compact and spongy bone). For the detailed model the 12 evaluated isotropic compact bone conductivity values are evenly distributed in the range $[0.0026, 0.016]\,\mathrm{S/m}$ including the commonly used conductivity value $0.0064\,\mathrm{S/m}$ for the compact bone which was used in the reference data generation, as stated above. The value of $0.0064\,\mathrm{S/m}$ was also used as the reference for the compact bone conductivity range.

- A **bulk model** where the skull is simplified to a single compartment (without spongiosa). For the bulk model the 12 evaluated isotropic bulk skull conductivity values are evenly distributed in the range $[0.0042, 0.025]\,\mathrm{S/m}$ including the commonly used conductivity value $0.0042\,\mathrm{S/m}$ [28] for the skull. For this model the reference for the skull conductivity chosen as 100% was $0.01\,\mathrm{S/m}$ which was suggested in [28].

Conductivity estimation

Conductivity estimation and simultaneous source reconstruction is performed on the two test models for each patient and for all reference data, estimating the bulk skull conductivity in the bulk model and the compact bone conductivity in the detailed model.

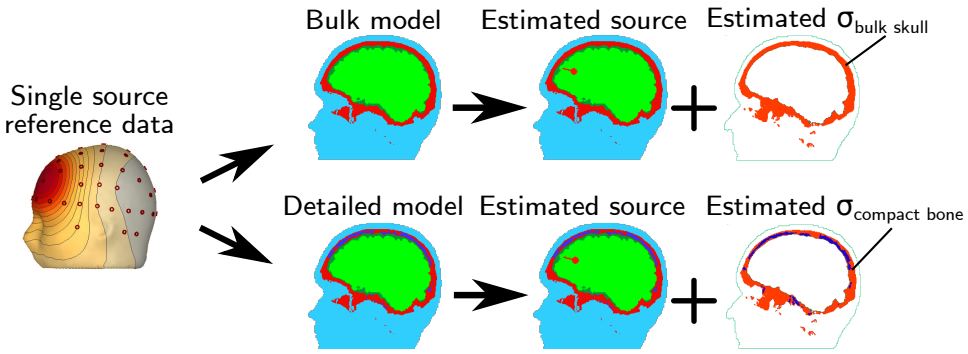

Figure 4.3: Conductivity estimation and source localization on both test models from single source reference data. The estimated conductivities are the bulk skull conductivity in the bulk model (the skull is modelled as a single compartment) and the compacta conductivity in the detailed model with spongiosa (the skull contains both compacta and spongiosa).

As we will see in this section, conductivity estimation is performed on each test model by maximising the goodness of fit between the reference paradigm data and the FEM forward computations with different homogeneous and isotropic conductivity values. For each conductivity value σ_i, $i = 1 \dots 12$ a lead field matrix $L(\sigma_i)$ was computed, capturing the head geometry and the tissues conductivities. A lead field matrix, computed by solving the EEG forward problem, represents the linear relationship between the amplitudes of dipolar sources within the brain and electrode measurements on the scalp. The dimension of a lead field matrix is $(n_{electrodes} \times 3 * n_{nodes})$ where $n_{electrodes}$ is the number of electrodes and $3 * n_{nodes}$ corresponds to the 3 canonical orientations at n_{nodes} fixed dipole locations.

For each precomputed lead field matrix $L(\sigma_i)$ a source estimation step is performed using a simple exhaustive search approach, where each node of an $2 \times 2 \times 2$ mm search grid is evaluated.

The estimated conductivity value, is the conductivity value σ_i used in the i^{th} precomputed lead field matrix (among the 12 precomputed lead field matrices) that gave the best goodness of fit to the reference data during the exhaustive search approach. Our goodness of fit measure is the ℓ^2 norm distance of the reference data from the projection norm of an evaluated node:

$$||EEG_{ref} - L_{node}(\sigma_i)M_{node}||_2 \tag{4.1}$$

where EEG_{ref} is a $(n_{electrodes} \times 1)$ column vector of the reference EEG measurements of a single paradigm generated on a reference model, $L_{node}(\sigma_i)$ is a $(n_{electrodes} \times 3)$ sub-matrix of the lead field matrix $L(\sigma_i)$ corresponding to the evaluated search grid node and M_{node} is a (3×1) column vector of the estimated source moment on the same search grid node. The source

moment is estimated as:

$$M_{node} = L^{\dagger}_{node}(\sigma_i) EEG_{ref} \tag{4.2}$$

where $L^{\dagger}_{node}(\sigma_i)$ is the pseudo-inverse of the sub-matrix $L_{node}(\sigma_i)$. The estimated conductivity corresponds to the index:

$$i = \underset{i}{\operatorname{argmax}} \left(\max_{node} \left(1 - \frac{||EEG_{ref} - L_{node}(\sigma_i) M_{node}||_2}{||EEG_{ref}||_2} \right) \right). \tag{4.3}$$

Observe that along with the estimated conductivity value, the source location is also obtained as the node maximizing the goodness of fit.

The conductivity estimation procedure thus follows the following algorithm:

1. Select a test model with conductivity values for all tissues except the tissue in question
2. Select a vector σ of N_c possible isotropic conductivities for the tissue in question
3. Compute the lead field matrix $L(\sigma_i)$, $i = 1, ..., N_c$ for each selected conductivity value σ_i for the tissue in question
4. For each conductivity value index $i = 1, ..., N_c$
   (a) For each $node = 1, 2, ..., N$ of the search grid compute: $p_i(node) = ||EEG_{ref} - L_{node}(\sigma_i) L^{\dagger}_{node}(\sigma_i) EEG_{ref}||_2$
   (b) Find the index $node^*$ minimizing $p_i(node)$
   (c) Compute the goal function value: $(1 - \frac{||EEG_{ref} - L_{node^*}(\sigma_i) M_{node^*}||_2}{||EEG_{ref}||_2})$
5. The optimal conductivity value is the one that corresponds to the maximum goal function value, while the optimal reconstructed source location is the $node^*$ for the optimal conductivity value.

Model evaluation

We evaluate the quality of the estimated conductivities and the accuracy of our source reconstruction on the test models (bulk or detailed).

Our main concern is to investigate the influence of the skull modelling on the quality of conductivity estimation.

To evaluate the quality of the conductivity estimation, a variability measure is defined that is able to compute a comparable quantity for both test models, despite the fact that the possible estimated conductivity values

belong to different ranges. For this purpose the coefficient of variation is computed as:

$$C_v = \frac{std}{\mu} \times 100\,, \tag{4.4}$$

where std is the standard deviation and μ the mean value of the estimated conductivities for a given model based on the 20 dipolar sources.

The localization errors are computed as the distance between the estimated sources in a test model and the original source locations used for the reference data generation.

Results

Influence of spongiosa modelling

The conductivity estimation results on the 20 manually selected sources are visualized in Fig. 4.4.

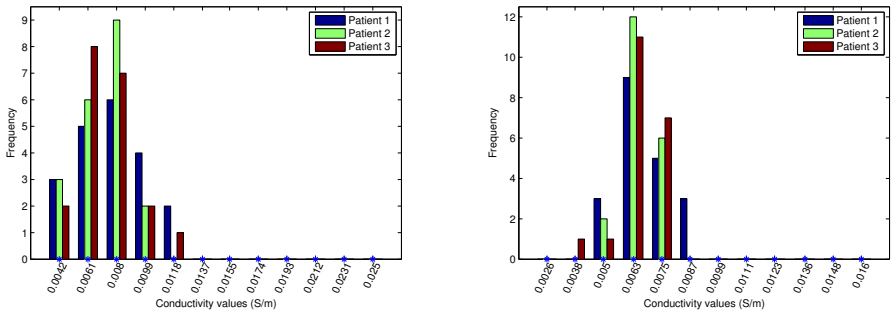

(a) Bulk model

(b) Detailed model

Figure 4.4: The frequency of the estimated conductivities for the 20 manually selected sources: The frequency of estimated conductivities for the three patients, using the simplified model (a) and the model containing the spongiosa (b). The compact bone conductivity value in the reference model was 0.0064 S/m.

The results of our estimated conductivities show that the range of estimated conductivities when estimating the conductivity of the bulk skull (bulk model) is $[0.0042, 0.0118]$ S/m for Patient 1 and Patient 3, and $[0.0042, 0.0099]$ S/m for Patient 2, whereas when estimating the compact bone conductivity accounting for the spongiosa (detailed model) the intervals are smaller: $[0.0050, 0.0087]$ S/m for Patient 1, $[0.0050, 0.0075]$ S/m for Patient 2, and $[0.0038, 0.0075]$ S/m for Patient 3.

The coefficient of variation (measuring the relative variability) of the estimated conductivities in the bulk model is 29% for Patient 1, 23% for

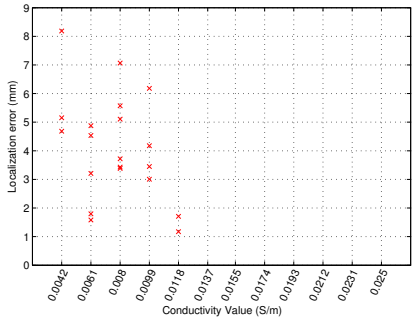

(a) Patient 1, bulk model

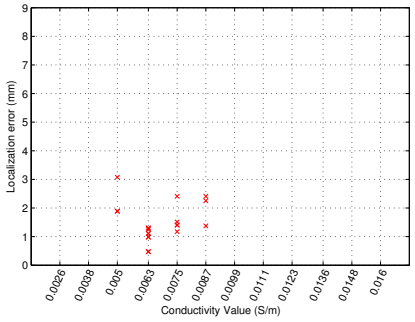

(b) Patient 1, detailed model

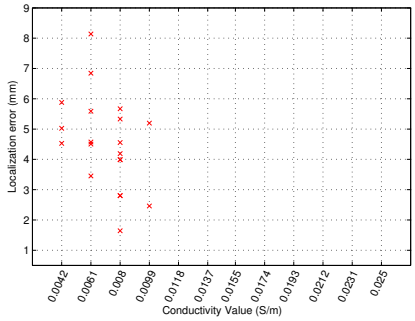

(c) Patient 2, bulk model

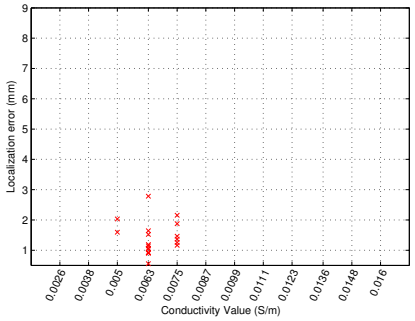

(d) Patient 2, detailed model

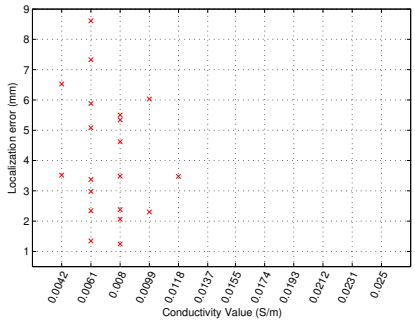

(e) Patient 3, bulk model

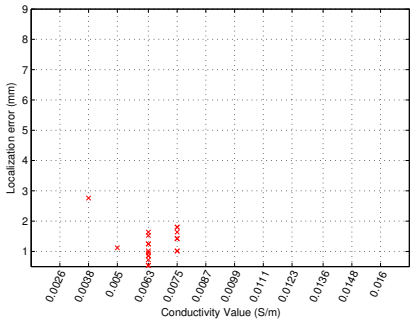

(f) Patient 3, detailed model

Figure 4.5: Localization errors for the 20 manually selected sources, across evenly spread conductivity values: results for three patients and their test models. The red x symbols indicate the localization error for the 20 manually selected dipoles.

Patient 2 and 25% for Patient 3, whereas in the detailed model the values are 17%, 11% and 14% respectively. The above implies that the relative variability of the estimated conductivities is 77%, 106% and 80% higher for each patient when estimating the conductivity of the bulk skull (bulk model) as compared to the model accounting for the spongiosa (detailed model).

The results of the simultaneous conductivity estimation and source localization, for all patients, are presented in Fig. 4.5. The results show that when using the bulk model to perform conductivity estimation and simultaneously recover the source locations, the obtained localization errors are higher (with errors reaching 9 mm for some sources) compared to the results obtained when using the detailed model where the localization errors are below 3 mm (except for one source for Patient 1 in Plot 4.5 (b).

Evaluation in the whole brain volume

Although the simulated data based on the 20 manually selected sources represent different brain areas, the number of the sources is not sufficient to explore the whole brain volume and assess the "global" performance of each test model. Therefore, new reference data are generated for a large number of probe – evaluation – sources with random orientations, that are evenly spread in the brain volume.

Two settings of probe sources are investigated: a) probe sources are placed on the nodes of the search grid used for the conductivity estimation procedure and b) probe sources are shifted such that they are placed between the nodes of the search grid. In the latter setting, there is no "inverse crime", since the locations used to generate the reference probe data differ from the ones used for conductivity estimation. The reference probe data are generated in each detailed model (used as reference) following an equivalent procedure as described in Subsection 4.2.2. Conductivity estimation and simultaneous source reconstruction is then performed for the new reference probe data on the test models.

Evaluation of the conductivity estimation

The conductivity estimation results on both probe source settings are presented in Fig. 4.6. The results show that the range of estimated conductivities is higher when the bulk model is used for conductivity estimation, compared to the results obtained using the detailed model.

The results in Figure 4.6(b) indicate the ideal scenario of conductivity estimation, where all the estimated conductivities are concentrated to the value 0.0063 S/m, i.e. the closest value to the conductivity used in the reference data simulation (0.0064 S/m).

Observe that the values of the frequency of the estimated conductivities in Figure 4.6(b) vary across the subjects. This is due to the size of the brain

volume of each patient and the number of sources that could be spread within it.

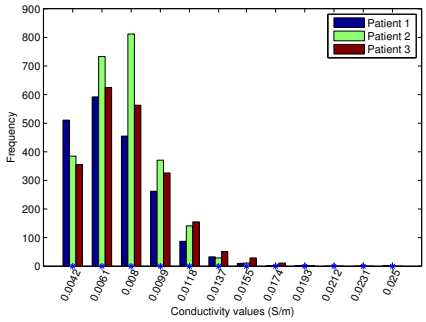

(a) Bulk model: sources on the nodes

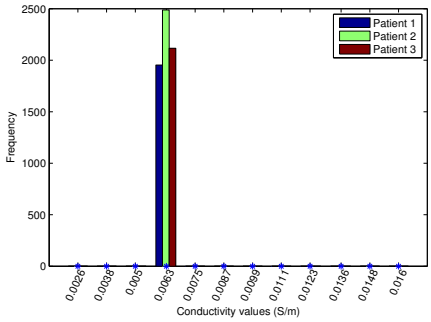

(b) Detailed model: sources on the nodes

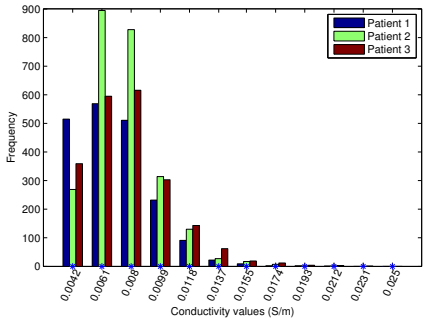

(c) Bulk model: sources between the nodes

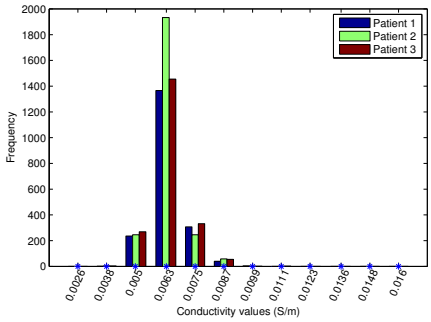

(d) Detailed model: sources between the nodes

Figure 4.6: The frequency of estimated conductivities for three patients, using a large number of probe sources spread in the brain volume. The frequency of estimated conductivities on the bulk (a) and on the detailed (b) model, in the ideal case where the probe sources had been on the nodes of the search grid for the reference probe data simulation. The frequency of estimated conductivities on the bulk (c) and on the detailed (d) model, when the probe sources had been between the nodes of the search grid for the reference probe data simulation. The compact bone conductivity value in the reference volume conductor was 0.0064 S/m.

Evaluation of the localization errors

To evaluate the localization error on the whole brain volume, the mean localisation error $\overline{d(\sigma_i)}$ for a conductivity value σ_i across the probe sources is computed as: the mean distance between the original probe locations (during the reference data simulation within the detailed model) and the

reconstructed sources (within a test model) during a source reconstruction step i.e. the reconstructed location $node^*$ for each probe source performing the exhaustive search approach for a lead field matrix $L(\sigma_i)$.

The localization errors of our test models are first evaluated over probe sources that are placed on the nodes of the search grid used for conductivity estimation. The obtained localization errors are illustrated in Fig. 4.7.

In this ideal situation, as both the simulated data (using the probe sources) and the search grid nodes used for conductivity estimation are on the same grid, the main difference between the probe data (simulated with the detailed model and the reference conductivities) and the conductivity estimation data fitting term (computed on a test model) comes from the differences in conductivity between the two models. Thus when the bulk model is used for conductivity estimation, its difference from the detailed model comes from the simplification of the skull tissues geometry. On the other hand, when the detailed model is used, its difference comes only from the conductivity value for the compact bone (0.0064 S/m during the data generation instead of the conductivity value investigated during the conductivity estimation).

As a consequence, the mean localization errors in the bulk model are in general much higher than the mean localization errors in the detailed model, with the minimum mean localization error in the bulk model (obtained for the conductivity value 0.008 S/m) being 5.5 mm, 4.3 mm, and 4.3 mm respectively for each patient, whereas in the detailed model (obtained for the conductivity value 0.0063 S/m) it is 0 mm for all patients. The latter confirms the expected superior performance of the detailed model in source localisation.

The localization errors of our models are then evaluated over the same number of probe sources, but shifted such that they are placed between the nodes of the search grid. The obtained results are illustrated in Fig. 4.8.

The mean localization errors for this probe setting are also higher in the bulk model compared to the detailed model, with the minimum mean localization error in the first (obtained for the conductivity value 0.008 S/m) being 6 mm, 5.2 mm and 4.9 mm respectively for each patient, whereas in the detailed model (obtained for the conductivity value 0.0063 S/m) being 1.7 mm for all patients. Compared to the results of Fig. 4.7 there is a general increase of the mean localization errors in all test models, but most noticeable is the increase in the detailed models for the minimum localisation error, increasing from 0 mm to 1.7 mm for all patients.

Note that as the search grid used for conductivity estimation has $2 \times 2 \times 2$ mm resolution, the minimum distance between a probe source location (laying in the middle of the search grid nodes) and the closest search grid node is approximately 1.7 mm, thus explaining the noticeable increase of the minimum mean localization error of the detailed models. The localization errors of the bulk models are also affected by the 1.7 mm distance between a probe

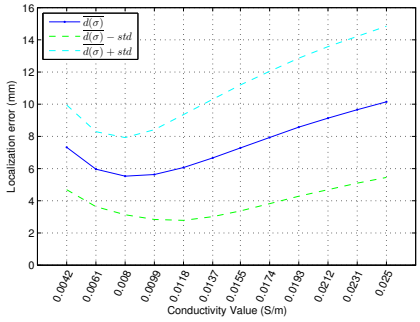

(a) Patient 1, bulk model

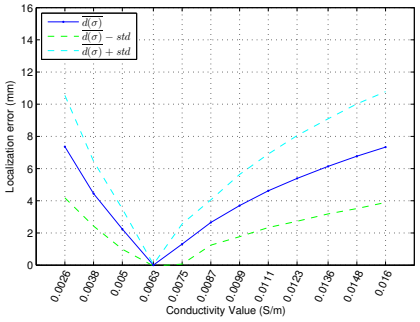

(b) Patient 1, detailed model

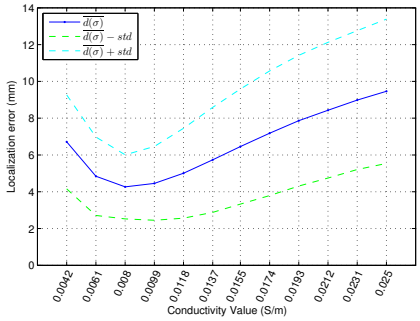

(c) Patient 2, bulk model

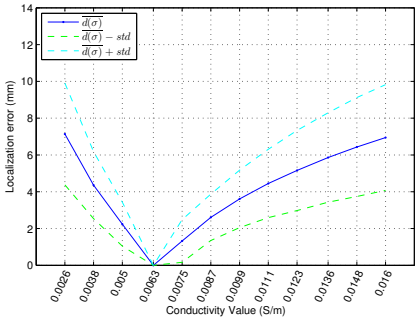

(d) Patient 2, detailed model

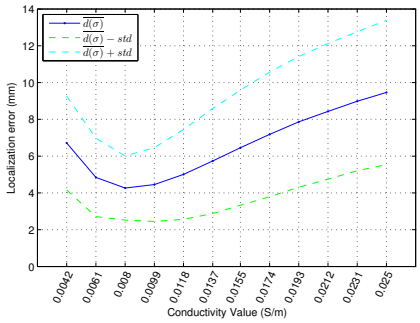

(e) Patient 3, bulk model

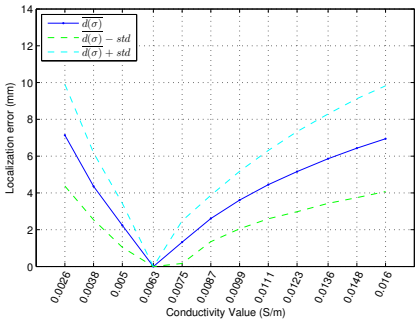

(f) Patient 3, detailed model

Figure 4.7: Mean localization errors for the probe sources placed on the search grid, across evenly spread conductivity values: results for three patients and their test models. The blue line indicates the mean localization errors for the evenly spread probe sources placed on the search grid. The dashed lines represent the standard deviation.

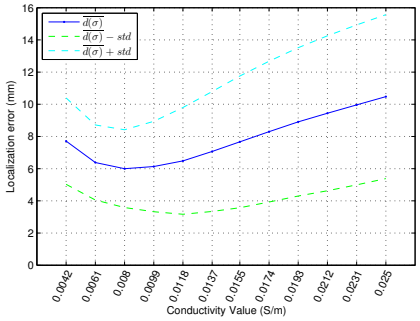

(a) Patient 1, bulk model

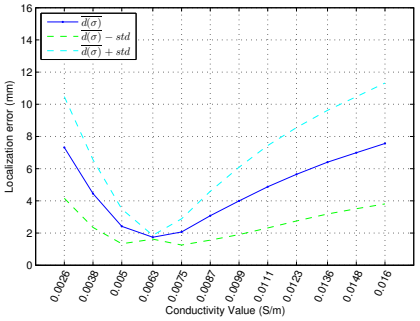

(b) Patient 1, detailed model

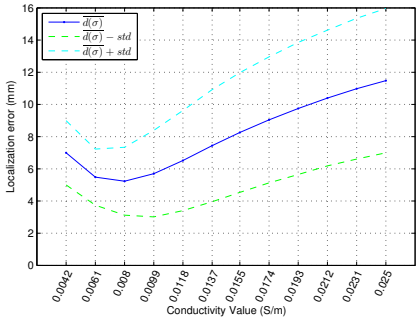

(c) Patient 2, bulk model

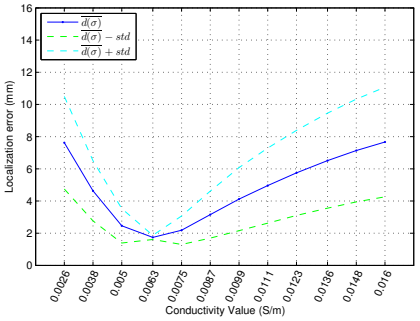

(d) Patient 2, detailed model

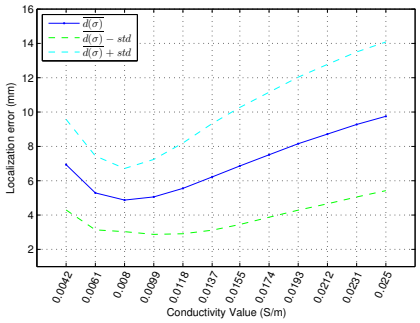

(e) Patient 3, bulk model

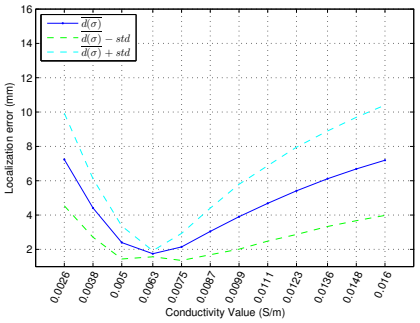

(f) Patient 3, detailed model

Figure 4.8: Mean localization errors for the probe sources placed off the search grid, across evenly spread conductivity values: results for three patients and their test models. The dashed lines represent the standard deviation.

source and the closest search grid node, but as there are many localisation errors with higher values than 1.7 mm (due to the model inaccuracies) the minimum mean localization error is not that much (visually) affected.

Observe that the mean localization results can also be viewed as the influence of wrongly estimated conductivity in source localization.

A head calibration scheme

Let us assume a plausible conductivity estimation scenario where one performs conductivity estimation on an event-related stimulation paradigm prior to collecting the actual data of interest, in order to calibrate the head model (volume conductor) and "improve" the later data analysis (source localization).

For example, consider that one would like to use SEP data in order to estimate the conductivity of an unknown tissue. Setting the estimated conductivity value for that tissue in his head model, one would like to analyse some EEG recordings from a different EEG experiment. Note that the location of the SEP arises within the somatosensory cortex whereas the activity of the EEG experiment may lie elsewhere. In such a scenario, the estimated conductivity of the tissue in question is optimised based on the activity (and the location) of the event-related stimulation paradigm and not on the activity of the actual data of interest.

Let us focus our attention on the inaccuracies one would get in the reconstructed sources following such a conductivity estimation scheme. We will investigate the following two questions: 1) when using an estimated conductivity value based on a single source to later perform source localization, what would be on average the obtained localization error? and 2) when randomly selecting a source for conductivity estimation, what would be on average the localisation error one should expect?

We will perform our investigation, using the estimated conductivities of the 20 manually selected sources (assuming that one has used one of those sources for the model calibration) and the localisation errors of the probe sources to assess on the performance of the test models. The performance of the test model will be evaluated on the values of the conductivities that were estimated during the model calibration i.e. the subset $J \subseteq \{1 \dots 12\}$ of estimated conductivity values using the 20 manually selected sources.

To answer the first question, one should consider the mean localisation error $\overline{d(\sigma_i)}$ for the subset $J \subseteq \{1 \dots 12\}$ of conductivity values. The variability of those mean localisation errors is also investigated, computing the difference of the maximum and minimum mean localisation errors for the same set of conductivity values $J \subseteq \{1 \dots 12\}$.

Finally, to answer the second question, we introduce the expected mean localization error metric computed as:

$$E[\,\overline{d}\,] = \frac{\sum_i w_i \overline{d(\sigma_i)}}{\sum_i w_i} \tag{4.5}$$

where $\overline{d(\sigma_i)}$ is the mean localization error across the probe sources for conductivity value σ_i while w_i is the number of times σ_i was estimated based on our 20 manually placed sources, i.e the frequency of estimated conductivities displayed in Figure 4.4(a).

The results of this investigation for both source configurations are summarised in Table 4.1.

Our investigation is first performed using probe sources placed on the nodes of the search grid used for conductivity estimation. The mean localization errors of the probe sources in this setting and the localization errors of the 20 manually placed sources (supposed to be used for the head calibration) are illustrated in Figure 4.9.

In the bulk model and for the same probe sources configuration, the difference between the maximum and the minimum mean localization error is 1.8 mm for Patient 1, 2.6 mm for Patient 2, and 2.4 mm for Patient 3.

The expected mean source localization error (5.98 mm, 4.89 mm, and 4.80 mm) for each patient respectively, is by 0.5 mm, 0.6 mm, and 0.5 mm larger than the optimal error in the same model.

Our investigation is then performed using probe sources shifted between the nodes of the search grid used for conductivity estimation. The mean localization errors of the probe sources in this setting and the localization errors of the 20 manually placed sources are illustrated in Figure 4.10.

In the bulk model for the shifted probe source configuration the difference between the maximum and the minimum mean localization error is 1.7 mm for Patient 1, 1.8 mm for Patient 2, and 2.0 mm for Patient 3.

The expected mean source localization error (6.43 mm, 5.62 mm, and 5.3 mm) for each patient is by 0.4 mm larger than the optimal error in the same model for all the patients.

Selection of the skull tissue conductivity

Estimating spongiosa conductivity

To further analyse the influence of the skull inhomogeneity in conductivity estimation, an additional investigation is performed estimating the conductivity of the spongy bone in the detailed model (instead of the conductivity of the compact bone). For this investigation we choose to evaluate 12 isotropic spongy bone conductivity values evenly distributed in the range $[0.012, 0.0717]$ S/m including the commonly used conductivity value

Table 4.1: Evaluation of the conductivity estimation and source reconstruction results for all three patients and all test models. Listed in rows are: (i) C_v, the coefficient of variation (in percent), (ii) the range of the mean localisation errors for the probe sources placed on the nodes of the search grid (in mm), (iii) the range of the mean localisation errors for the probe sources placed between the nodes of the search grid (in mm), (iv) the expected mean localisation error for the probe sources for placed on the nodes of the search grid (in mm), and (v) the expected mean localisation error for the probe sources placed between the nodes of the search grid. The range of the mean localisation errors was computed for $i \in J$, where $J \subseteq \{1 \dots 12\}$ is the set of estimated conductivity values using the 20 manually selected sources. The notations P_{on} and P_{off} distinguish if the probe sources where placed on or between (off) the search grid nodes (used for conductivity estimation).

	Patient 1		Patient 2		Patient 3	
Metric	Bulk	Detailed	Bulk	Detailed	Bulk	Detailed
C_v	29	17	23	11	25	14
$\overline{d_i}(P_{on})$	[5.53, 7.32]	[0, 2.65]	[4.29, 6.92]	[0, 2.34]	[4.27, 6.71]	[0, 4.36]
$\overline{d_i}(P_{off})$	[6, 7.71]	[1.74, 3.07]	[5.23, 6.99]	[1.74, 2.46]	[4.87, 6.94]	[1.75, 4.41]
$E[\,\overline{d}(P_{on})]$	5.98	1.06	4.89	0.67	4.80	0.79
$E[\,\overline{d}(P_{off})]$	6.43	2.12	5.62	1.95	5.30	2.05

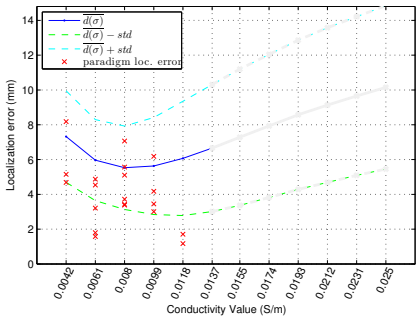

(a) Patient 1, bulk model

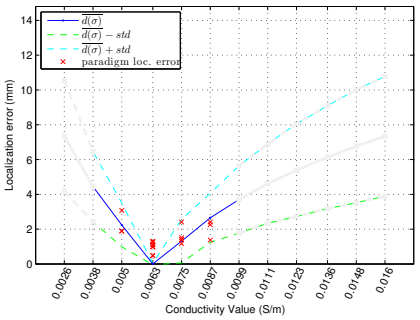

(b) Patient 1, detailed model

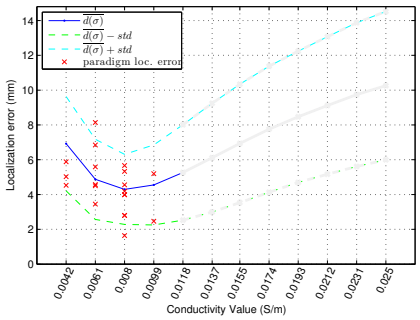

(c) Patient 2, bulk model

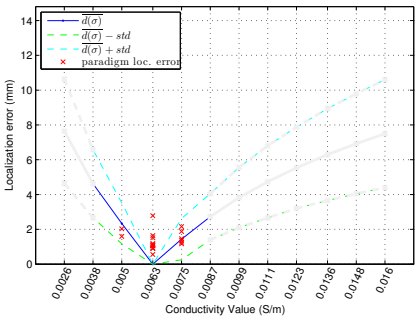

(d) Patient 2, detailed model

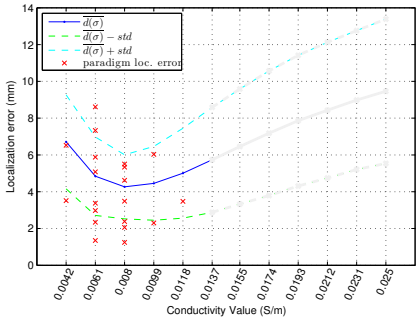

(e) Patient 3, bulk model

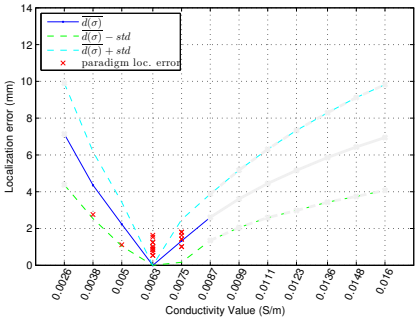

(f) Patient 3, detailed model

Figure 4.9: Localization errors for the 20 manually selected sources and the probe sources placed on the search grid, across evenly spread conductivity values: results for three patients and their test models. The red x symbols indicate the localization error for the 20 manually selected sources. The blue line indicates the mean localization errors for the evenly spread probe sources placed on the search grid. The dashed lines represent the standard deviation.

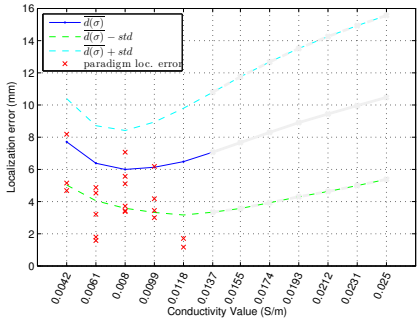

(a) Patient 1, bulk model

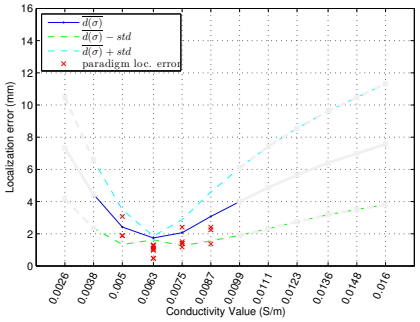

(b) Patient 1, detailed model

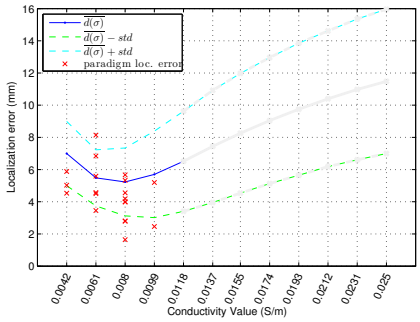

(c) Patient 2, bulk model

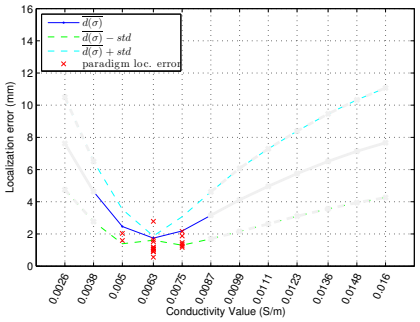

(d) Patient 2, detailed model

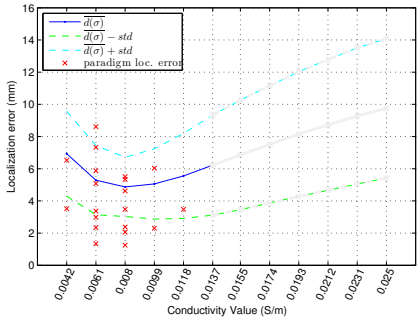

(e) Patient 3, bulk model

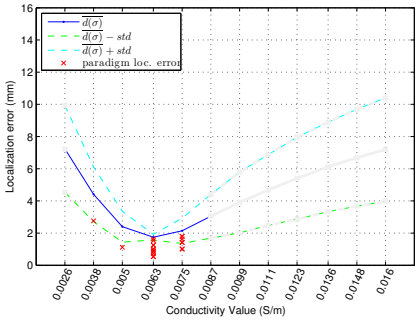

(f) Patient 3, detailed model

Figure 4.10: Localization errors for the 20 manually selected sources and the probe sources placed off the search grid, across evenly spread conductivity values: results for three patients and their test models. The red x symbols indicate the localization error for the 20 manually selected sources. The blue line indicates the mean localization errors for the evenly spread probe sources placed off the search grid. The dashed lines represent the standard deviation.

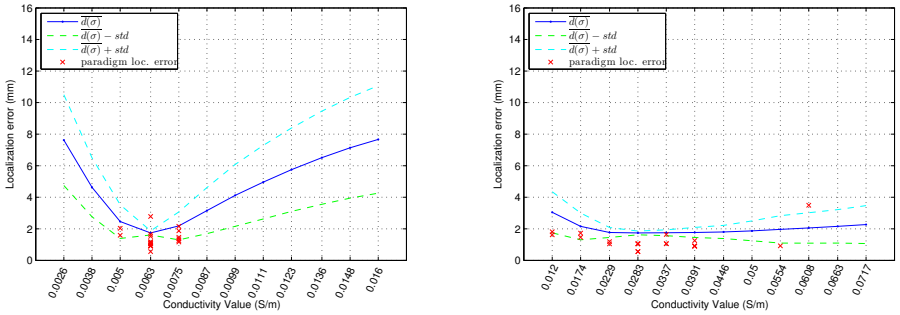

(a) Compact bone

(b) Spongy bone

Figure 4.11: Localization errors across evenly spread conductivity values, estimating (a) the compact bone and (b) spongy bone conductivity on the detailed model of Patient 2. The red x symbols indicate the localization error for the 20 manually selected sources. The blue line indicates the mean localization errors for the evenly spread probe sources placed off the search grid. The dashed lines represent the mean localization errors for the evenly spread probe sources plus (or minus) the standard deviation. For the reference data generation the compact bone conductivity was set to 0.0064 S/m and for the spongy bone conductivity to 0.0287 S/m.

0.0287 S/m for the spongy bone which was used in the reference data generation described in Section 4.2.2.

Conductivity estimation and simultaneous source localization is performed using the method described in Section 4.2.2 for the 20 manually placed sources (see Section 4.2.2) and also the probe sources that are shifted between the nodes of the search grid (see Section 4.3.2).

The conductivity estimation results for the spongiosa are compared to the results obtained for the compacta and presented in Figure 4.11. The results show that estimating the spongy bone conductivity under this range of conductivities when the compact bone is known, does not influence significantly the source localization. Indeed the obtained localization errors are quite low over the different conductivity values when estimating the spongy bone conductivity. In contrast, when conductivity estimation was performed on the compact bone the obtained localization errors increase more rapidly over the different conductivity values. This justifies our choice in our investigations, performing conductivity estimation on the compact bone instead of the spongy bone.

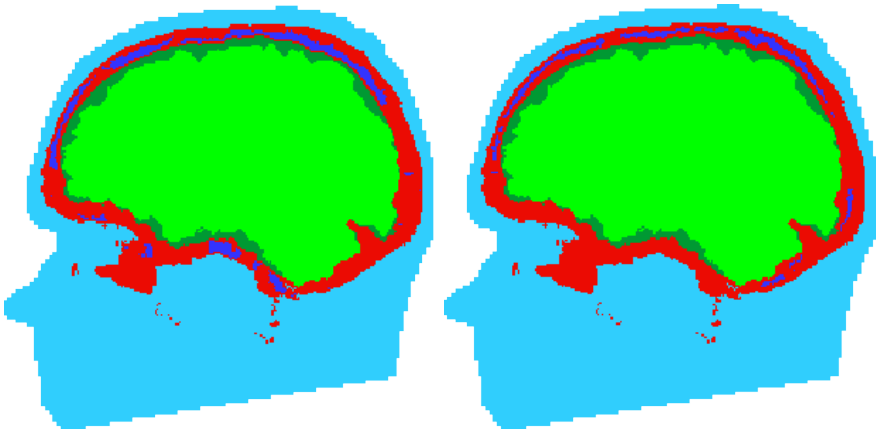

(a) Colin27: 14.84% of spongy bone (b) BLNI2012: 8.57% of spongy bone

Figure 4.12: Comparison of two detailed models for Patient 2 with different spongy bone distributions included in the skull: (a) the "Colin 27 Average Brain" template and (b) the reference model in [65].

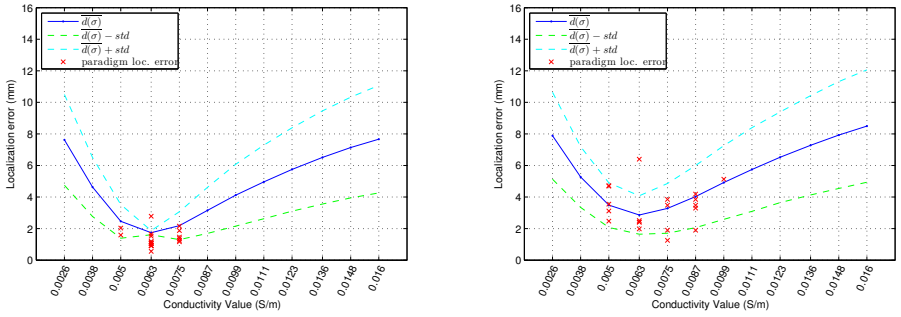

(a) Colin27 (b) BLNI2012

Figure 4.13: Localization errors across evenly spread conductivity values, using two detailed models for Patient 2 with different spongy bone distributions included in the skull: results using (a) the Colin27 detailed model and (b) the BLNI2012 detailed model. The blue line indicates the mean localization errors for the evenly spread probe sources placed off the search grid. The dashed lines represent the standard deviation. For the reference data generation the compact bone conductivity was set to 0.0064 S/m.

Influence of the spongiosa distribution in compacta conductivity estimation

To determine the influence of the spongiosa distribution in conductivity estimation, a new detailed model was constructed for Patient 2 using a different spongy bone template. Note that we are back to compacta conductivity estimation. The distribution of the spongy bone included in the new detailed model was extracted from the reference model in [65] following an equivalent procedure as described in Section 4.2.1. Let as refer to this detailed model as "BLNI2012". Recall that the distribution of the spongy bone in the detailed model of Patient 2 was based on the "Colin 27 Average Brain" [52] template, already presented in Section 4.2.1. We will refer to this model as "Colin27". In the Colin27 detailed model, the amount of spongiosa present in the skull was 14.84% of the overall skull tissue, whereas in the BLNI2012 detailed model the amount of spongiosa was 8.57%. The amount of spongiosa present within the skull, was estimated according to the volume assigned to the spongiosa tissues relative to the total skull volume (spongiosa and compacta) in each generated FEM model. Note that including the two different spongy bone distributions to the segmentation of the same patient, allow us both to investigate the influence of the spongiosa distribution in the same space (skull size and geometry) and also use the same source locations for the data generation in both models.

Conductivity estimation and simultaneous source localization is performed using the method described in Section 4.2.2 for the 20 manually placed sources (see Section 4.2.2) and also the probe sources that are shifted between the nodes of the search grid (see Section 4.3.2) on the BLNI2012 detailed model.

A side by side comparison of the two models is illustrated in Figure 4.12. The conductivity estimation results and the obtained localization errors are presented in Figure 4.13, comparing them with the previously obtained results on the Colin27 detailed model.

The coefficient of variation (measuring the relative variability) of the estimated conductivities in the Colin27 detailed model was 11 % whereas in the BLNI2012 detailed model the coefficient is 22 %. Comparing the above coefficients of variation with the one obtained for the bulk model in the same patient (see Section 4.3.1), the above values implies that the relative variability of the estimated conductivities is 105 % and 7 % higher when estimating the conductivity of the bulk skull (bulk model) as compared to the models accounting for the spongiosa (the Colin27 and the BLNI2012 detailed model respectively).

Observe that the above increase in the relative variability is quite different when using the two detailed models (the Colin27 and the BLNI2012 relative to the bulk models). The difference between the Colin27 and the BLNI2012 detailed model was the distribution of the spongy bone included

in the same skull segmentation, which reduced from 14.84% to 8.57%. This indicate that when the amount of spongy bone present in the skull is low, the detailed model is not very different from the bulk model and thus the importance of spongiosa within the skull is reduced.

Discussion

In this part, we performed simultaneous conductivity estimation and source reconstruction on detailed and simplified realistic head models of three patients to investigate the influence of spongiosa in skull modelling for conductivity estimation. Our main goal was to quantify the amount of variability in the estimated conductivities when the spongiosa was included or not within the skull layer. The resulting source localisation errors were also computed. Our conductivity estimation scheme was performed using a set of predefined conductivity values for the tissue in question, fitting forward model computations (on the investigated models) to simulated EEG measurements (on detailed head models considered as reference models). We simulated EEG measurements considering single dipole sources placed manually in different brain areas, and we also used a large number of probe sources evenly spread in the brain to cover a large number of possible brain locations. Simultaneous conductivity estimation and source localisation was performed over all simulated data.

Our results show that when estimating the bulk skull conductivity using the manually placed sources the relative variance of the estimated values was for the three patients larger than when taking the spongiosa into account. An even higher variability of the estimated conductivities was observed, when the conductivity estimation was performed using the probe sources. This confirms our initial expectation with regard to the influence of the local variation of the bulk skull conductivity due to the spongiosa distribution.

For the bulk models and the conductivity values estimated from some of the 20 manually placed sources the mean localization error was at least 1.8 mm larger than the optimal error (i.e. the minimum mean localization error). This means that, when selecting a single paradigm (an event-related stimulation paradigm explained by a single dipole source) for conductivity estimation it cannot be guaranteed that the localization error using the resulting estimated conductivity will be optimal.

In the bulk models the majority of the localization errors for the 20 manually placed sources are smaller than the mean localization error of the probe sources for the same conductivity value. This indicates that although estimating the bulk skull conductivity from a chosen source paradigm leads to decreased localization error for that paradigm, using the same conductivity value to explain the sources of the actual data of interest, may on average lead to bigger localization errors.

When randomly choosing a paradigm and estimating the bulk skull conductivity an additional localization error of at least 0.5 mm has to be expected.

The presented issue could be mitigated by performing the conductivity estimation not only for one but for multiple paradigms representing different brain areas. The additional experiments may, however, require too much time and effort for this to be a viable solution.

We mention the recent work [1] presenting an approach for estimating the conductivity based on multiple near-dipolar scalp EEG maps automatically extracted from continuous EEG data. Conductivity estimation in this approach is based not only on a single source location, and in consequence, the estimated values might yield estimated values which are closer to the optimal value.

As an alternative solution, electrical impedance tomography (EIT) [98] can be used, where current is injected through a pair of EEG electrodes while the unknown conductivities can be estimated maximizing a goodness of fit with the data at the other electrodes [79]. There, pairs of electrodes may be used to increase the performance of conductivity estimation. Moreover, the location of the source of the electrical activity and its waveform i.e the injected electrical current at the pair of electrodes, is well known. Therefore, the uncertainty of the source term in the conductivity estimation scheme is eliminated, which could increase the accuracy of the estimated conductivities. This is hardly the case in EEG (or even in SEP measurements), where the exact location of the activity is not perfectly known and may lead to inaccuracies in the estimated conductivities due to wrongly estimated source locations.

In our investigations, a decrease of the localisation errors in the detailed models is observed compared to the bulk models, indicating that including the spongiosa in skull modelling improves the source localisation accuracy. This comes in agreement with the work in [28] where simulations were performed on detailed and simplified skull models to investigate the influence on the errors in the forward calculations and the reconstructed dipole locations.

According to the work of [3, 95] where the conductivity of several skull samples was measured invasively, the conductivity of the human skull is not homogeneous and depends on the local skull structures (presence of compacta only or both compacta and spongiosa).

In our investigations (see Section 4.4.1), estimating the spongy bone conductivity when the compact bone is known, did not influence significantly the conductivity estimation results. This may indicate that lower conductivity values influence more the localization errors compared to misspecified higher conductivity values. Therefore in the present work, we have chosen to estimate the compact bone conductivity instead.

In our study we have chosen to simulate single dipole EEG data and use a simple exhaustive search approach to localize them. Due to the simplicity

of the localization method, which evaluates only the nodes of a search grid to localize the sources, the reported sources location are restricted to lay on the nodes of the evaluation grid. This can introduce localization errors that depend on the resolution of the evaluation grid (see the discussion at the end of Section 4.3.2) and can affect the estimated conductivities. The above issue could be resolved considering several advanced source localisation techniques existing both for dipolar or distributed sources [72].

Finally, our experiments have also shown that the reference model generation workflow allows to model compartments (skull spongiosa) even when they are not visible in the original MRI data. An additional investigation on real EEG measurements would however be required to determine whether a bulk skull model or including spongiosa from a skull template to the individual's skull segmentation would improve the conductivity estimation results. In such an investigation one could follow a procedure similar to [15, 110] in order to construct an accurate head model from MRI data (where the skull spongiosa is visible), and combine EEG and MEG measurements to estimate the compacta conductivity. Then using the created model as reference, could evaluate the performance of the other models with the bulk skull and the included "artificial" spongiosa.

Conclusion

Our results show that without accounting for the internal skull structure the conductivity estimation is not in all cases optimal. The estimated conductivity depends on the paradigm which data is used during the estimation process.

We also recommend, if possible, to use a model that correctly represents the internal structure of the skull to reduce the variability in the estimated conductivities.

CHAPTER 5

General discussion and conclusion

The human head is an inhomogeneous medium, anatomically complicated, composed of several tissues of various conductivities. While the conductivity values of some head tissues may be considered as known, the conductivity value of the skull shows great inter-subject and intra-subject variability. Therefore an average conductivity value across a population can not be used to describe the skull conductivity of each individual (see discussion in Section 1.1).

In addition, EEG signals are affected by the conductivities of the head tissues and particularly by the conductivity of the skull because of its low value, which also affects the source localization accuracy in EEG. Therefore, conductivity estimation techniques are required to minimize the uncertainty of the unknown skull conductivity value (or values) and thus improve the accuracy of source localization techniques, as established in [68]. The ultimate goal of conductivity estimation to be achieved, is to avoid the invasive measurements that are currently in use (see for example [63]), which can cause implications to the individual.

The aim of conductivity estimation techniques is to determine the unknown conductivity value within a domain from non invasive measurements acquired at some distance of its boundary. To solve the inverse conductivity estimation problem in EEG, and in addition to the EEG measurements, we assumed the geometry of the head (including the internal tissues) and the source parameters to be known.

While the geometry of the head tissues can be extracted (with sufficient accuracy) from imaging modalities, the location of the sources is rarely known in clinical or experimental applications. Exceptions are specific experiments or well studied cases in EEG where the response of the brain to a stimulus generates an electrical activity which is expected to arise within a certain area of the brain. Such an example are the Somatosensory Evoked Potentials (SEP) which are obtained in response to a sensory stimulus. The location of the response activity arises within the somatosensory cortex and

it is quite focal in that region of the brain. Still, SEP/SEF data source localization show significant inter-individual variability in terms of estimated source locations and orientations.

Concerning the sources and in order to solve the inverse conductivity estimation problem, one has either to have a priori knowledge about the source distribution or to solve both the source localization and conductivity estimation problems. The two problems depend on each others solution for accurate results.

A priori knowledge about the sources can be obtained for example using SEP data, as the location of the response activity is "known" and the activity is quite focal, thus can be explained by a single dipole. An alternative solution is to use simultaneously with EEG other modalities to locate the sources, such as MEG that is shown to be nearly not affected by the conductivity of the skull [15, 110] or even intracranial recordings as in [63].

Conductivity estimation on a homogeneous skull

We solved in Part I the conductivity estimation problem for the skull in a 3-layered spherical head geometry, where the skull is modelled as a single and homogeneous layer. The problem is solved from the available EEG partial boundary data, expanded on the spherical harmonics basis, and transmitted over the spherical interfaces by transfer functions, while the full knowledge of the sources is given (through a number of coefficients of its spherical harmonics expansion).

Linear algebra computations then allow us to find polynomials that possess a root which should coincide with the unknown skull conductivity, thus solving the estimation problem. This proves that a solution to the skull conductivity estimation problem exists, when the sources are known, and also that the solution is unique and "stable".

We provided a reconstruction algorithm for the skull conductivity, which solves the problem with low computational cost. It uses a non-linear least squares minimization scheme applied to the computed spherical harmonics coefficients of the solution in the three layers. Our numerical study shows that the algorithm is able to accurately estimate the skull conductivity, with good robustness properties with respect to various levels of noise and source configurations.

In reality, neither approximating the head tissues by spherical layers is realistic, nor the location of the sources is perfectly known. To solve the problem of unrealistic head geometry, realistically shaped head models have been proposed to model the non spherical geometry of the head tissues in greater detail. Using realistic head models, the source localization accuracy was improved with respect to the spherical head models, but still, in most applications the skull was modelled as a single bulk and homogeneous layer

using an average (reported) conductivity value that might be far from the true conductivity of a given individual.

Unlike the conductivity estimation case in our spherical head model, where the unknown conductivity value was recovered solving polynomial equations, in realistic models, one can estimate the unknown conductivity value as the value that provides the best goodness of fit between the given EEG data and a number of forward simulations considering different conductivity settings (varying the unknown tissue conductivity). If the sources are not known (which is usually the case), additional forward simulations have to be considered (for each conductivity setting) evaluating various source locations in order to find the best goodness of fit to the given data, solving simultaneously both problems [68].

Observe that estimating a conductivity value as the value that best explains the given EEG data via the given head model and the source parameters, the estimated value does not necessary have to match the biological conductivity of the unknown tissue. This may happen because the head models are approximations of the individuals head, with modelling inaccuracies in terms of tissue geometry and conductivity. Performing conductivity estimation one also compensates for inaccuracies in the head model (assuming that the source parameters are correct), which might yield to significant improvement to the source localization accuracy. Thus, performing conductivity estimation can be viewed as an additional advantage over solving the source localization problem alone.

Conductivity estimation on an inhomogeneous skull

Several studies based on invasive measurements and sensitivity analysis of the skull conductivity show that the skull is indeed inhomogeneous, with the local skull conductivity depending on the internal skull structure and its local composition [3, 28, 95]. In Part II, we question the validity of the human skull inhomogeneity for conductivity estimation in EEG, performing a simulation study that compares two head models in realistic geometry: the first modelling the skull as a single and homogeneous layer, the second modelling its inhomogeneity by accounting for two different types of skull tissues (compacta and spongiosa).

Our simultaneous conductivity estimation and source localization scheme was performed using a set of predefined conductivity values for the tissue in question, fitting forward model computations (on the investigated models) to simulated EEG measurements (on detailed head models considered as reference models). Simultaneous conductivity estimation and source localization was performed over simulated data from single dipoles.

Our study shows that without accounting for the internal skull structure the conductivity estimation is not in all cases optimal. The estimated

conductivity depends on the sources captured by the EEG data used during the estimation process. When using a wrong conductivity value for the bulk skull, the mean localization error computed over spread sources within the whole head volume increased, while this increase is significantly lower in the model accounting for the internal skull structure. Those results are in agreement with previous studies showing that the internal structure of the skull should be considered in the head modelling [28, 73]. Therefore, we recommend, if possible, to use a model that correctly represents the internal structure of the skull to reduce the variability in the estimated conductivities.

Selection of skull tissue and conductivities

For the examined conductivity values in our study, our investigation suggest that when accounting for the skull compact and spongiosa, conductivity estimation should be performed on compacta, as spongiosa has less influence on the conductivity estimation procedure. When spongiosa can not be segmented from the available data, a spongiosa template can be included within the bulk skull instead, but to conclude whether including a skull template improves or not the source localization in practice, further investigations are needed. In [73] an artificial spongiosa layer was included within the skull by iteratively eroding the compact layer, to improve the source localization accuracy of the bulk skull model. The investigation was based only on a single subject, which makes it difficult to conclude for the whole population.

Performing simultaneous conductivity estimation and source localization in our study a number of forward simulations had to be considered with different conductivity settings (varying the unknown conductivity value). For each distinct conductivity setting, a new lead field matrix solution has to be computed making the problem computationally demanding.

In an effort to determine the right conductivity range for conductivity estimation, one may consider solving the conductivity estimation problem first in a spherical geometry (where the solution can be obtained with low computational cost) or find ways to improve the computational time of the forward problem in the realistic geometry.

In [69], a method is proposed which allows to approximate the lead field matrix for a set of conductivity configurations, using only the exact solution for a small set of basis points from the conductivity space. This approach has the computational advantage that allows one to investigate a wide range of conductivity values with greater precision without making the problem impractical (in terms of computational time).

Determining the conductivity points that influence most the conductivity estimation procedure could also be of great importance, rather than selecting evenly spread conductivity points within a plausible range, as in

our investigations.

Source localization, techniques and restrictions

As the source mislocation affects the estimated conductivities, the more accurate the source estimation is the better the conductivity estimation will perform. The choice of source model and source localization technique to analyse the given EEG data is of crucial importance as the given EEG data might capture focal or not activity, activity generated by one or more active brain areas, different amounts of noise present in the data. In our study in the realistic head geometry, a simple exhaustive search approach was used assuming that only one dipolar source is active at a single time instant. This assumption can already constrain a lot the use of our technique depending on the expected nature of the sources in the given EEG data.

Several more advanced source localization techniques are proposed in the literature, such as MUSIC [74] which can detect multiple dipolar sources, techniques that try to separate the source [76] or that rely on distributed sources. Among the techniques that rely on distributed sources are: minimum norm [94], mixed norm [45], LORETA [81, 82], and EPIFOCUS [71] which can be used to locate focal activity (as the one generated in SEP and epileptic EEG recordings), see discussion in [72] for more techniques. Finally, in [80] an extension to a data-based method has been developed that learns a dictionary from a set of measurements aquired over multiple repetitions (trials). The method has been developed to better handle the trial to trial variability (variations in latency and phase of signals) than simply averaging them and is designed to handle multidimensional data, such as MEG and EEG. Using such techniques with our conductivity estimation scheme is expected to improve its use with more general and experimental EEG recordings.

While in our study the whole brain was discretized forming a grid of source locations that was used as the source space, the sources are in general expected to arise within the gray matter and not within the white matter of the brain. Using SEP or similar data where the sources are expected to arise within a specific cortex lobe, this a priori information can be incorporated into the conductivity estimation scheme restricting further the source space. To restrict the source space and allow sources to be active only within the somatosensory cortex, segmentation of this area should be performed, which can be done using brain anatomical atlases. An anatomical brain atlas, is a division of the brain into structures and can be registered to the individual's MRI data to segment the structure of interest (in our case the volume of the somatosensory cortex) as illustrated in Fig 5.1.

Restricting the source parameters such as the amplitude, may also improve the conductivity estimation procedure.

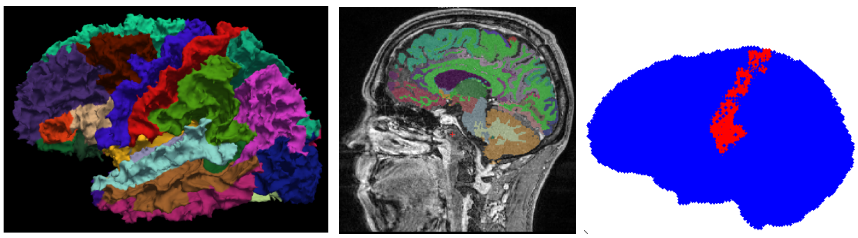

Figure 5.1: Source space restriction using an anatomical atlas. [Left] A brain anatomical atlas. [Middle] The registered atlas superimposed on a slice of the individuals MRI data. [Right] The resulting restricted source space (in red color).

Multimodal data

With continuous technological advances in computer power and the improvements in imaging modalities, more and more information can be combined to solve the inverse source localization problem in EEG.

Already, the geometry of the head tissues can be extracted by segmenting non-invasive imaging modalities and their combinations (see Section 1.5). Due to the improvements in the resolution of the MRI sequences, segmentation of the various head tissues is becoming more and more reliable. New MRI sequences that better image the skull [106] are going to improve the skull segmentation, which is currently challenging from MRI data, leading to head models with improved accuracy.

In the recent years, an increasing number of approaches have emerged that aim at improving the source localization by combining simultaneous multimodal measurements, see for example [14] where MEG and EEG measurements are combined to solve the problem.

APPENDIX A

Mathematical notes and tools

Mathematical notes

Operators

In the three-dimensional Cartesian coordinate system we have the following operators:

The **gradient** of a scalar function f, is a vector defined as:

$$\operatorname{grad} f = \nabla f = \frac{\partial f}{\partial x}\mathbf{i} + \frac{\partial f}{\partial y}\mathbf{j} + \frac{\partial f}{\partial z}\mathbf{k}\,.$$

Shows how fast f changes in the three directions.

The **divergence** of a vector field $\mathbf{F}$ is a scalar defined as:

$$\operatorname{div}\mathbf{F} = \nabla \cdot \mathbf{F} = \frac{\partial F_x}{\partial x} + \frac{\partial F_y}{\partial y} + \frac{\partial F_z}{\partial z}\,.$$

The divergence at a point represents the degree to which a small volume around the point is a source or a sink for the vector flow.

The **Curl** of a vector field $\mathbf{F}$, is a vector defined as:

$$\operatorname{rot}\mathbf{F} = \nabla \times \mathbf{F} = \left(\frac{\partial F_z}{\partial y} - \frac{\partial F_y}{\partial z}\right)\mathbf{i} + \left(\frac{\partial F_x}{\partial z} - \frac{\partial F_z}{\partial x}\right)\mathbf{j} + \left(\frac{\partial F_y}{\partial x} - \frac{\partial F_x}{\partial y}\right)\mathbf{k}\,.$$

The Laplacian of a real valued function is a real valued quantity defined as:

$$\Delta f = \nabla^2 f = \nabla \cdot \nabla f = \frac{\partial^2 f}{\partial x^2} + \frac{\partial^2 f}{\partial y^2} + \frac{\partial^2 f}{\partial z^2} = 0\,.$$

The Laplace operator can be interpreted as the extent to which a point represents a source or sink.

Spherical coordinates

In a spherical domain the problem is usually considered in spherical coordinates, an orthogonal three-dimensional coordinate system expressed by the radius r, the inclination θ and the azimuth ϕ. The Cartesian coordinates $\mathbf{r} = [x, y, z]$ can be retrieved from the spherical coordinates (radius r, inclination θ, azimuth ϕ), where $r \in [0, \infty)$, $\theta \in [0, \pi]$, $\phi \in [0, 2\pi)$, by:

$$\begin{cases} x = r\,\sin\theta\,\cos\phi\,, \\ y = r\,\sin\theta\,\sin\phi\,, \\ z = r\,\cos\theta\,. \end{cases}$$

Laplace equation

Laplace's equation is a second-order partial differential equation often written as:

$$\nabla^2\varphi = 0 \qquad \text{or} \qquad \Delta\varphi = 0\,, \tag{A.1}$$

where $\nabla^2 = \Delta$ is the Laplace operator and φ is a **scalar function**.

The solutions of Laplace's equation are called **harmonic functions** (source Wiki, [51]).

In three dimensions, the problem is to find twice-differentiable real-valued functions f, of real variables x, y, and z, such that the following equation is satisfied in terms of:

Cartesian coordinates:

$$\Delta f = \frac{\partial^2 f}{\partial_x^2} + \frac{\partial^2 f}{\partial_y^2} + \frac{\partial^2 f}{\partial_y^2} = 0\,.$$

Spherical coordinates:

$$\Delta f = \frac{1}{\rho^2}\frac{\partial}{\partial\rho}\left(\rho^2\frac{\partial f}{\partial\rho}\right) + \frac{1}{\rho^2\sin\theta}\frac{\partial}{\partial\theta}\left(\sin\theta\frac{\partial f}{\partial\theta}\right) + \frac{1}{\rho^2\sin^2\theta}\frac{\partial^2 f}{\partial\varphi^2} = 0\,.$$

Harmonic functions

In a region Ω a function is called harmonic **if** it satisfies the Laplace equation **at every point** in the region. If the region is the exterior of a certain closed surface S, then it must in addition vanish like $1/l$ for $l \to \infty$.

Poisson equation:

If the right-hand side is specified as a given function, $h(x, y, z)$, i.e., if the whole equation is written as

$$\Delta f = h\,, \tag{A.2}$$

then it is called "Poisson's equation".

Spherical harmonic coefficients

As we have seen in Section 2.4, the function of the potential $u_i(r, \theta, \varphi)$ that is harmonic on a boundary S_i, can be expanded on spherical harmonic basis of degree $K > 0$. The spherical harmonic coefficients g_{km} and β_{0km} of the expanded potensial $u_0(r_0, \theta, \varphi)$ and $g(r_2, \theta, \varphi)$ can then be computed as:

$$g_{km} = \iint_{S_2} g(r_2, \theta, \varphi) r_2^k Y_{km}(\theta, \varphi) sin\theta d\theta d\varphi \,, \tag{A.3}$$

$$\beta_{0km} = \iint_{S_0} u_s(r_0, \theta, \varphi) r_0^{-(k+1)} Y_{km}(\theta, \varphi) sin\theta d\theta d\varphi \,. \tag{A.4}$$

See [33, Ch. II, Eq. (7.74)].

Boundary value problems

When a physical problem is considered in a bounded domain of space, for example within a spherical geometry, then we are led to boundary value problems [83].

Two of the most important **boundary conditions** are of the following types:

1. Boundary conditions of the first kind (Dirichlet conditions).
2. Boundary conditions of the second kind (Neumann conditions).

The formulation of the Dirichlet and Neumann boundary conditions for the **Laplace** equations follows.

Dirichlet boundary conditions

Find the solution of the equation $\Delta u = 0$ in some domain of space (or plane) which takes **given values on the boundary**.

For example find the distribution of the electric potential inside a domain if the potential on its boundary is given.

$$\begin{cases} \Delta u = 0 & \text{in the domain } \Omega \,, \\ u = \varphi & \text{on the boundary } \partial\Omega \,, \end{cases}$$

where φ is a given function.

Neumann boundary conditions

Find the solution of the given equation in some domain of space (or plane) assuming that the **outwards normal derivative** $\partial_n u$ (which is proportional to the mass flux) **is given on** $\partial\Omega$.

$$\begin{cases} \Delta u = 0 & \text{in the domain } \Omega \,, \\ \partial_n u = \varphi & \text{on the boundary } \partial\Omega \,. \end{cases}$$

The Neumann problem has a meaning **only in the case** where the **total flux** through the boundary $\partial\Omega$ is **equal to zero** ($\int_{\partial\Omega} \partial_n u ds = 0$).

Neumann boundary conditions and Poisson equation

The Dirichlet and Neumann boundary conditions are formulated similarly for the **Poisson** equation $\Delta u = f$.

For the Neumann boundary value problem:

$$\begin{cases} \Delta u = f & \text{in the domain } \Omega\,, \\ \partial_n u = \varphi & \text{on the boundary } \partial\Omega\,, \end{cases}$$

to have a solution it is necessary and sufficient that

$$\int_\Omega f dx = \int_{\partial\Omega} \varphi ds\,.$$

Another peculiarity of the Neumann boundary problem for the Poisson equation is that the solution is **not unique**.

One way of solving such problems is by finding a set of solutions of the homogeneous partial differential equation in question that satisfies certain boundary conditions. Based on the linear superposition of those solution one is able to construct the general solution.

Bibliography

[1] Z. A. Acar, C. E. Acar, and S. Makeig. Simultaneous head tissue conductivity and EEG source location estimation. *NeuroImage*, 124:168–180, 2016.

[2] Z. A. Acar and S. Makeig. Effects of Forward Model Errors on EEG Source Localization. *Brain Topography*, 26(3):378–396, Jan. 2013.

[3] M. Akhtari, H. C. Bryant, A. N. Mamelak, E. R. Flynn, L. Heller, J. J. Shih, M. Mandelkem, A. Matlachov, D. M. Ranken, E. D. Best, M. A. DiMauro, R. R. Lee, and W. W. Sutherling. Conductivities of Three-Layer Live Human Skull. *Brain Topography*, 14(3):151–167, Mar. 2002.

[4] G. Alessandrini. Singular solutions of elliptic equations and the determination of conductivity by boundary measurements. *J. Differential Equations*, 84:252–272, 1990.

[5] G. Alessandrini. Stable determination of conductivity by boundary measurements. *Appl. Anal.*, 27:153–172, 1998.

[6] G. Alessandrini. Generic uniqueness and size estimates in the inverse conductivity problem with one measurement. *Le Matematiche*, 54(3):5–14, Nov. 1999.

[7] G. Alessandrini, L. Rondi, E. Rosset, and S. Vessella. The stability for the Cauchy problem for elliptic equations. *Inverse Problems*, 25, 2009.

[8] G. Alessandrini and S. Vessella. Lipschitz stability for the inverse conductivity problem. *Advances in Applied Mathematics*, 35:207–241, 2005.

[9] H. Ammari and H. Kang. *Polarization and Moment Tensors, With Applications to Inverse Problems and Effective Medium Theory*. Springer, 2007.

[10] J. P. Ary, S. A. Klein, and D. H. Fender. Location of Sources of Evoked Scalp Potentials: Corrections for Skull and Scalp Thicknesses. *IEEE Transactions on Biomedical Engineering*, BME-28(6):447–452, June 1981.

[11] B. Atfeh, L. Baratchart, J. Leblond, and J. R. Partington. Bounded extremal and Cauchy-Laplace problems on the sphere and shell. *J. Fourier Analysis and Applications*, 16(2):177–203, 2010.

[12] C. Athanasiadis, A. Ramm, and I. Stratis. Inverse acoustic scattering by a layered obstacle. *Inverse Problems, Tomography, and Image Processing. Ramm A. ed., Plenum Press, New York*, pages 1–8, 1998.

[13] S. Axler, P. Bourdon, and W. Ramey. *Harmonic Function Theory*. Springer-Verlag, 2001.

[14] Ü. Aydin, S. Rampp, A. Wollbrink, H. Kugel, J.-H. Cho, T. R. Knösche, C. Grova, J. Wellmer, and C. H. Wolters. Zoomed MRI Guided by Combined EEG/MEG Source Analysis: A Multimodal Approach for Optimizing Presurgical Epilepsy Work-up and its Application in a Multi-focal Epilepsy Patient Case Study. *Brain Topography*, pages 1–17, May 2017.

[15] Ü. Aydin, J. Vorwerk, P. Küpper, M. Heers, H. Kugel, A. Galka, L. Hamid, J. Wellmer, C. Kellinghaus, S. Rampp, and C. H. Wolters. Combining EEG and MEG for the Reconstruction of Epileptic Activity Using a Calibrated Realistic Volume Conductor Model. *PLoS ONE*, 9(3):e93154, Mar. 2014.

[16] S. Baillet, J. C. Mosher, and R. M. Leahy. Electromagnetic brain mapping. *IEEE Signal Processing Magazine*, 18(6):14–30, Nov. 2001.

[17] L. Baratchart, A. Ben Abda, F. Ben Hassen, and J. Leblond. Recovery of pointwise sources or small inclusions in 2D domains and rational approximation. *Inverse problems*, 21:51–74, 2005.

[18] S. B. Baumann, D. R. Wozny, S. K. Kelly, and F. M. Meno. The electrical conductivity of human cerebrospinal fluid at body temperature. *IEEE Transactions on Biomedical Engineering*, 44(3):220–223, Mar. 1997.

[19] D. Brunet, M. M. Murray, and C. M. Michel. Spatiotemporal Analysis of Multichannel EEG: CARTOOL. *Intell. Neuroscience*, 2011:2:1–2:15, Jan. 2011.

[20] H. Buchner, G. Knoll, M. Fuchs, A. Rienäcker, R. Beckmann, M. Wagner, J. Silny, and J. Pesch. Inverse localization of electric dipole current

sources in finite element models of the human head. *Electroencephalography and Clinical Neurophysiology*, 102(4):267–278, Apr. 1997.

[21] G. Chavent and K. Kunisch. The Output Least Squares Identifiability of the Diffusion Coefficient from an H1–Observation in a 2–D Elliptic Equation. *ESAIM: Control, Optimisation and Calculus of Variations*, 8:423–440, Jan. 2002.

[22] G. Chen and J. Zhou. *Boundary Element Methods with Applications to Nonlinear Problems*, volume 7. Springer Science & Business Media, 2010.

[23] M. Clerc, J. Leblond, J.-P. Marmorat, and T. Papadopoulo. Source localization using rational approximation on plane sections. *Inverse Problems*, 28(5):055018, 2012.

[24] M. Clerc, J. Leblond, J.-P. Marmorat, and C. Papageorgakis. Uniqueness result for an inverse conductivity recovery problem with application to EEG. *Rendiconti dell'Istituto di Matematica dell'Università di Trieste. An International Journal of Mathematics*, 48, 2016.

[25] A. Crouzeix, B. Yvert, O. Bertrand, and J. Pernier. An evaluation of dipole reconstruction accuracy with spherical and realistic head models in MEG. *Clinical Neurophysiology*, 110(12):2176–2188, Dec. 1999.

[26] B. N. Cuffin. EEG localization accuracy improvements using realistically shaped head models. *IEEE Transactions on Biomedical Engineering*, 43(3):299–303, Mar. 1996.

[27] B. N. Cuffin. EEG localization accuracy improvements using realistically shaped head models. *IEEE Transactions on Biomedical Engineering*, 43(3):299–303, Mar. 1996.

[28] M. Dannhauer, B. Lanfer, C. H. Wolters, and T. R. Knösche. Modeling of the human skull in EEG source analysis. *Human Brain Mapping*, 32(9):1383–1399, Sept. 2011.

[29] F. Darvas, J. J. Ermer, J. C. Mosher, and R. M. Leahy. Generic head models for atlas-based EEG source analysis. *Human Brain Mapping*, 27(2):129–143, Feb. 2006.

[30] G. Dassios. Electric and magnetic activity of the brain in spherical and ellipsoidal geometry. *Mathematical Modeling in Biomedical Imaging I*, pages 133–202, 2009.

[31] G. Dassios and A. S. Fokas. Electro-magneto-encephalography for a three-shell model: Dipoles and beyond for the spherical geometry. *Inverse Problems*, 25(3):035001, 2009.

[32] G. Dassios and A. S. Fokas. The definite non-uniqueness results for deterministic EEG and MEG data. *Inverse Problems*, 29(6):065012, 2013.

[33] R. Dautray and J.-L. Lions. *Mathematical Analysis and Numerical Methods for Science and Technology: Volume 1 Physical Origins and Classical Methods*. Springer-Verlag Berlin Heidelberg, 1 edition, 1990.

[34] J. C. de Munck, B. W. van Dijk, and H. Spekreijse. Mathematical dipoles are adequate to describe realistic generators of human brain activity. *IEEE Transactions on Biomedical Engineering*, 35(11):960–966, Nov. 1988.

[35] A. Delorme, J. Palmer, J. Onton, R. Oostenveld, and S. Makeig. Independent EEG Sources Are Dipolar. *PLOS ONE*, 7(2):e30135, Feb. 2012.

[36] A. El Badia and T. Ha-Duong. An inverse source problem in potential analysis. *Inverse Problems*, 16:651–663, 2000.

[37] O. Faiz, S. Blackburn, and D. B. Moffat. *Anatomy at a Glance*. At a glance series. Wiley-Blackwell, Chichester, West Sussex, UK Hoboken, NJ, 3. ed edition, 2011. OCLC: 649701824.

[38] O. Faugeras, F. Clément, R. Deriche, R. Keriven, T. Papadopoulo, J. Roberts, T. Viéville, F. Devernay, J. Gomes, and G. Hermosillo. The inverse EEG and MEG problems: The adjoint state approach I: The continuous case. 1999.

[39] A. S. Fokas and Y. Kurylev. Electro-magneto-encephalography for the three-shell model: Minimal L2-norm in spherical geometry. *Inverse Problems*, 28(3):035010, 2012.

[40] V. Fonov, A. C. Evans, K. Botteron, C. R. Almli, R. C. McKinstry, and D. L. Collins. Unbiased average age-appropriate atlases for pediatric studies. *NeuroImage*, 54(1):313–327, Jan. 2011.

[41] C. Gabriel, S. Gabriel, and E. Corthout. The dielectric properties of biological tissues: I. Literature survey. *Physics in Medicine & Biology*, 41(11):2231, 1996.

[42] S. Gabriel, R. W. Lau, and C. Gabriel. The dielectric properties of biological tissues: II. Measurements in the frequency range 10 Hz to 20 GHz. *Physics in Medicine & Biology*, 41(11):2251, 1996.

[43] R. Ganesan and S. Radhakrishnan. Segmentation of computed tomography brain images using genetic algorithm. *International Journal of Soft Computing*, 4(4):157–161, 2009.

[44] N. G. Gençer and C. E. Acar. Sensitivity of EEG and MEG measurements to tissue conductivity. *Physics in Medicine and Biology*, 49(5):701, Mar. 2004.

[45] A. Gramfort, M. Kowalski, and M. Hämäläinen. Mixed-norm estimates for the M/EEG inverse problem using accelerated gradient methods. *Physics in Medicine & Biology*, 57(7):1937, 2012.

[46] A. Gramfort, T. Papadopoulo, E. Olivi, M. Clerc, and others. OpenMEEG: Opensource software for quasistatic bioelectromagnetics. *Biomed. Eng. Online*, 9(1):45, 2010.

[47] R. Grech, T. Cassar, J. Muscat, K. P. Camilleri, S. G. Fabri, M. Zervakis, P. Xanthopoulos, V. Sakkalis, and B. Vanrumste. Review on solving the inverse problem in EEG source analysis. *Journal of NeuroEngineering and Rehabilitation*, 5(1):25, Nov. 2008.

[48] M. Hämäläinen, R. Hari, J. Ilmoniemi, J. Knuutila, and O. V. Lounasmaa. Magnetoencephalography theory, instrumentation, and applications to noninvasive studies of the working human brain. *Revies of Modern Physics*, 65:413–497, 1993.

[49] M. Hämäläinen and J. Sarvas. Realistic conductivity geometry model of the human head for interpretation of neuromagnetic data. *IEEE Trans. Biomedical Engineering*, 2(36):165–171, 1989.

[50] J. Haueisen, D. S. Tuch, C. Ramon, P. H. Schimpf, V. J. Wedeen, J. S. George, and J. W. Belliveau. The Influence of Brain Tissue Anisotropy on Human EEG and MEG. *NeuroImage*, 15(1):159–166, Jan. 2002.

[51] B. Hofmann-Wellenhof and H. Moritz. *Physical Geodesy*. Springer Science & Business Media, Oct. 2006.

[52] C. J. Holmes, R. Hoge, L. Collins, R. Woods, A. W. Toga, and A. C. Evans. Enhancement of MR Images Using Registration for Signal Averaging. *Journal of Computer Assisted Tomography*, 22(2), 1998.

[53] V. Isakov. On uniqueness of recovery of a discontinuous conductivity coefficient. *Comm. Pure Appl. Math.*, 41:865–877, 1988.

[54] V. Isakov. *Inverse Problems for Partial Differential Equations*. Springer-Verlag, 1998.

[55] M. Jenkinson, P. Bannister, M. Brady, and S. Smith. Improved optimization for the robust and accurate linear registration and motion correction of brain images. *NeuroImage*, 17(2):825–841, Oct. 2002.

[56] K. Jerbi, J. C. Mosher, S. Baillet, and R. M. Leahy. On MEG forward modelling using multipolar expansions. *Physics in Medicine & Biology*, 47(4):523, 2002.

[57] D. Kandaswamy, T. Blu, and D. Van De Ville. Analytic sensing for multi-layer spherical models with application to EEG source imaging. *Inverse Problems and Imaging*, 7(4):1251–1270, 2013.

[58] H. Kang and J. K. Seo. Layer potential technique for the inverse conductivity problem. *Inverse Problems*, 12:267–278, 1996.

[59] H. Kang and J. K. Seo. A note on uniqueness and stability for the inverse conductivity problem with one measurement. *J. Korean Math. Soc.*, 38:781–792, 2001.

[60] C. Kenig, J. Sjöstrand, and G. Uhlmann. The Calderón Problem with Partial Data. *Ann. of Math.*, 165(2):567–591, 2007.

[61] A. Kirsch. *An Introduction to the Mathematical Theory of Inverse Problems*. Springer, 1996.

[62] P. H. Laarne, M. L. Tenhunen-Eskelinen, J. K. Hyttinen, and H. J. Eskola. Effect of EEG Electrode Density on Dipole Localization Accuracy Using Two Realistically Shaped Skull Resistivity Models. *Brain Topography*, 12(4):249–254, June 2000.

[63] Y. Lai, W. van Drongelen, L. Ding, K. E. Hecox, V. L. Towle, D. M. Frim, and B. He. Estimation of in vivo human brain-to-skull conductivity ratio from simultaneous extra- and intra-cranial electrical potential recordings. *Clinical Neurophysiology*, 116(2):456–465, Feb. 2005.

[64] M. Lalancette, M. Quraan, and D. Cheyne. Evaluation of multiple-sphere head models for MEG source localization. *Physics in Medicine & Biology*, 56(17), 2011.

[65] B. Lanfer, M. Scherg, M. Dannhauer, T. R. Knösche, M. Burger, and C. H. Wolters. Influences of skull segmentation inaccuracies on EEG source analysis. *NeuroImage*, 62(1):418–431, Aug. 2012.

[66] J. Leblond. Identifiability properties for inverse problems in EEG data processing and medical engineering, with observability and optimization issues. *Acta Applicandae Mathematicae*, 135(1):175–190, 2015.

[67] J. Leblond, C. Paduret, S. Rigat, and M. Zghal. Source localization in ellipsoids by the best meromorphic approximation in planar sections. *Inverse Problems*, 24(3):035017, 2008.

[68] S. Lew, C. H. Wolters, A. Anwander, S. Makeig, and R. S. MacLeod. Improved EEG source analysis using low-resolution conductivity estimation in a four-compartment finite element head model. *Human Brain Mapping*, 30(9):2862–2878, Sept. 2009.

[69] K. Maksymenko, T. Papadopoulo, and M. Clerc. A fast EEG forward problem approximation method and its application to tissue conductivity estimation. International Conference on Basic and Clinical Multimodal Imaging, 2017.

[70] T. Medani, D. Lautru, D. Schwartz, Z. Ren, and G. Sou. FEM Method for the EEG Forward Problem and Improvement Based on Modification of the Saint Venant's Method. *Progress In Electromagnetics Research*, 153:11–22, 2015.

[71] R. G. d. P. Menendez, S. G. Andino, G. Lantz, C. M. Michel, and T. Landis. Noninvasive Localization of Electromagnetic Epileptic Activity. I. Method Descriptions and Simulations. *Brain Topography*, 14(2):131–137, Dec. 2001.

[72] C. M. Michel, M. M. Murray, G. Lantz, S. Gonzalez, L. Spinelli, and R. Grave de Peralta. EEG source imaging. *Clinical Neurophysiology*, 115(10):2195–2222, Oct. 2004.

[73] V. Montes-Restrepo, P. van Mierlo, G. Strobbe, S. Staelens, S. Vandenberghe, and H. Hallez. Influence of Skull Modeling Approaches on EEG Source Localization. *Brain Topography*, 27(1):95–111, Jan. 2014.

[74] J. C. Mosher, S. Baillet, and R. M. Leahy. Eeg Source Localization and Imaging Using Multiple Signal Classification Approaches. *Journal of Clinical Neurophysiology*, 16(3):225–238, May 1999.

[75] J. C. Mosher and R. M. Leahy. Recursive MUSIC: A framework for EEG and MEG source localization. *IEEE Transactions on Biomedical Engineering*, 45(11):1342–1354, Nov. 1998.

[76] J. C. Mosher, P. S. Lewis, and R. M. Leahy. Multiple dipole modeling and localization from spatio-temporal MEG data. *IEEE Transactions on Biomedical Engineering*, 39(6):541–557, June 1992.

[77] J.-C. Nédélec. *Acoustic and Electromagnetic Equations: Integral Representations for Harmonic Problems*, volume 144. Springer Science & Business Media, 2001.

[78] P. L. Nunez and R. Srinivasan. *Electric Fields of the Brain: The Neurophysics of EEG*. Oxford University Press, Jan. 2006.

[79] T. F. Oostendorp, J. Delbeke, and D. F. Stegeman. The conductivity of the human skull: Results of in vivo and in vitro measurements. *IEEE Transactions on Biomedical Engineering*, 47(11):1487–1492, Nov. 2000.

[80] C. Papageorgakis, S. Hitziger, and T. Papadopoulo. Dictionary Learning for Multidimensional Data. In *Proceedings of GRETSI 2017*, Juan-les-Pins, France, Sept. 2017.

[81] R. D. Pascual-Marqui, M. Esslen, K. Kochi, D. Lehmann, and others. Functional imaging with low-resolution brain electromagnetic tomography (LORETA): A review. *Methods and findings in experimental and clinical pharmacology*, 24(Suppl C):91–95, 2002.

[82] R. D. Pascual-Marqui, D. Lehmann, T. Koenig, K. Kochi, M. C. G. Merlo, D. Hell, and M. Koukkou. Low resolution brain electromagnetic tomography (LORETA) functional imaging in acute, neuroleptic-naive, first-episode, productive schizophrenia. *Psychiatry Research: Neuroimaging*, 90(3):169–179, June 1999.

[83] V. P. Pikulin and S. I. Pohozaev. *Equations in Mathematical Physics: A Practical Course*. Springer Science & Business Media, Jan. 2012.

[84] R. Pohlmeier, H. Buchner, G. Knoll, A. RienÄcker, R. Beckmann, and J. Pesch. The influence of skull-conductivity misspecification on inverse source localization in realistically shaped finite element head models. *Brain Topography*, 9(3):157–162, Mar. 1997.

[85] R. Potthast and I. Stratis. The Singular Sources Method for an Inverse Transmission Problem. *Computing*, 75(2-3):237–255, Aug. 2005.

[86] C. Ramon, P. H. Schimpf, and J. Haueisen. Influence of head models on EEG simulations and inverse source localizations. *BioMedical Engineering OnLine*, 5(1):10, Feb. 2006.

[87] J. K. Rice, C. Rorden, J. S. Little, and L. C. Parra. Subject position affects EEG magnitudes. *NeuroImage*, 64:476–484, Jan. 2013.

[88] D. Rivest-Hénault, N. Dowson, P. B. Greer, J. Fripp, and J. A. Dowling. Robust inverse-consistent affine CT–MR registration in MRI-assisted and MRI-alone prostate radiation therapy. *Medical Image Analysis*, 23(1):56–69, July 2015.

[89] C. Rorden, L. Bonilha, J. Fridriksson, B. Bender, and H.-O. Karnath. Age-specific CT and MRI templates for spatial normalization. *Neuroimage*, 61(4):957–965, July 2012.

[90] S. Rush and D. A. Driscoll. Current Distribution in the Brain From Surface Electrodes. *Anesthesia & Analgesia*, 47(6):717, November/December 1968.

[91] C. E. Sanchez, J. E. Richards, and C. R. Almli. Age-Specific MRI Templates for Pediatric Neuroimaging. *Developmental Neuropsychology*, 37(5):379–399, July 2012.

[92] L. Spinelli, S. G. Andino, G. Lantz, M. Seeck, and C. M. Michel. Electromagnetic Inverse Solutions in Anatomically Constrained Spherical Head Models. *Brain Topography*, 13(2):115–125, Dec. 2000.

[93] C. Stark. ROI-Demons. `http://darwin.bio.uci.edu/~cestark/roial/roial.html`.

[94] M. Stenroos and O. Hauk. Minimum-norm cortical source estimation in layered head models is robust against skull conductivity error. *Neuroimage*, 81:265–272, Nov. 2013.

[95] C. Tang, F. You, G. Cheng, D. Gao, F. Fu, G. Yang, and X. Dong. Correlation between structure and resistivity variations of the live human skull. *IEEE Transactions on Biomedical Engineering*, 55(9):2286–2292, 2008.

[96] N. Toussaint, J.-C. Souplet, and P. Fillard. MedINRIA: Medical Image Navigation and Research Tool by INRIA. In *Proc. of MICCAI'07 Workshop on Interaction in Medical Image Analysis and Visualization*, Brisbane, Australia, Australia, 2007.

[97] G. Uhlmann. Electrical impedance tomography and Calderón's problem. *Inverse Problems*, 25(12):123011, 2009.

[98] G. Uhlmann. Electrical impedance tomography and Calderón's problem. *Inverse Problems*, 25(12):123011, 2009.

[99] P. A. Valdés-Hernández, N. von Ellenrieder, A. Ojeda-Gonzalez, S. Kochen, Y. Alemán-Gómez, C. Muravchik, and P. A. Valdés-Sosa. Approximate average head models for EEG source imaging. *Journal of Neuroscience Methods*, 185(1):125–132, Dec. 2009.

[100] S. Vallaghé and M. Clerc. A global sensitivity analysis of three- and four-layer EEG conductivity models. *IEEE Transactions on Biomedical Engineering*, 56(4):988–995, Apr. 2009.

[101] S. Vallaghe and M. Clerc. A Global Sensitivity Analysis of Three- and Four-Layer EEG Conductivity Models. *IEEE Transactions on Biomedical Engineering*, 56(4):988–995, Apr. 2009.

[102] S. Vallaghé, M. Clerc, and J.-M. Badier. In vivo conductivity estimation using somatosensory evoked potentials and cortical constraint on the source. In *4th IEEE International Symposium on Biomedical Imaging: From Nano to Macro, 2007. ISBI 2007*, pages 1036–1039, Apr. 2007.

[103] R. Van Uitert, C. Johnson, and L. Zhukov. Influence of head tissue conductivity in forward and inverse magnetoencephalographic Simulations using realistic head models. *IEEE Transactions on Biomedical Engineering*, 51(12):2129–2137, Dec. 2004.

[104] T. Vercauteren, X. Pennec, A. Perchant, and N. Ayache. Diffeomorphic demons: Efficient non-parametric image registration. *NeuroImage*, 45(1, Supplement 1):S61–S72, Mar. 2009.

[105] J. Vorwerk, J.-H. Cho, S. Rampp, H. Hamer, T. R. Knösche, and C. H. Wolters. A guideline for head volume conductor modeling in EEG and MEG. *NeuroImage*, 100(Supplement C):590–607, Oct. 2014.

[106] F. Wiesinger, L. I. Sacolick, A. Menini, S. S. Kaushik, S. Ahn, P. Veit-Haibach, G. Delso, and D. D. Shanbhag. Zero TEMR bone imaging in the head. *Magnetic Resonance in Medicine*, 75(1):107–114, Jan. 2016.

[107] C. Wolters, A. Anwander, G. Berti, and U. Hartmann. Geometry-Adapted Hexahedral Meshes Improve Accuracy of Finite-Element-Method-Based EEG Source Analysis. *IEEE Transactions on Biomedical Engineering*, 54(8):1446–1453, Aug. 2007.

[108] C. H. Wolters, A. Anwander, X. Tricoche, D. Weinstein, M. A. Koch, and R. S. MacLeod. Influence of tissue conductivity anisotropy on EEG/MEG field and return current computation in a realistic head model: A simulation and visualization study using high-resolution finite element modeling. *NeuroImage*, 30(3):813–826, Apr. 2006.

[109] C. H. Wolters, L. Grasedyck, and W. Hackbusch. Efficient computation of lead field bases and influence matrix for the FEM-based EEG and MEG inverse problem. *Inverse Problems*, 20(4):1099, Aug. 2004.

[110] C. H. Wolters, S. Lew, R. S. MacLeod, and M. Hämäläinen. Combined EEG/MEG source analysis using calibrated finite element head models. *Biomedizinische Technik/Biomedical Engineering. Rostock, Germany: Walter de Gruyter*, 55(Suppl 1):64–68, 2010.

[111] Z. Zhang, P. Liu, D. Zhou, and L. Ding. An improved 10-tissue human head model with real anatomical structure and hexahedral discretization feature in magnetic induction measurement simulation. *Computer Assisted Surgery*, 21(sup1):148–153, Dec. 2016.